

Measuring the Time Dependence
of $B_s^o - \overline{B}_s^o$ Oscillations

by


Manuella Greta Vinciter
B.Sc., McGill University, 1990.


A thesis submitted in partial fulfillment
of the requirements for the degree of
Master of Science


in the Department of Physics and Astronomy.

We accept this thesis as conforming
to the required standard.


Dr. R. K. Keeler, Supervisor (Department of Physics and Astronomy)


Dr. A. Astbury, Departmental Member (Department of Physics and Astronomy)


Dr. G. Beer, Departmental Member (Department of Physics and Astronomy)


Dr. D. Pitman, Departmental Member (Department of Physics and Astronomy)


Dr. H. Kwok, Outside Member (Department of Electrical Engineering)


Dr. S. Page, External Examiner (Department of Physics, University of Manitoba)

© Manuella Greta Vinciter, 1992
University of Victoria.

*All rights reserved. Thesis may not be reproduced in whole or in part,
by photocopy or other means, without the permission of the author.*

ACCEPTED
FACULTY OF GRADUATE STUDIES

DEAN
4 FEB 93

QA 865
V5


20130101 00:00:00
20130101 00:00:00
20130101 00:00:00
20130101 00:00:00


Supervisor: Dr. R. K. Keeler


Abstract


A Monte Carlo study was made of the possibility of measuring the frequency of oscillation of $B_s^0 - \bar{B}_s^0$ mixing given existing detector technology. A measurement of this oscillation frequency is important since it leads to the determination of one of the elements of the Cabibbo-Kobayashi-Maskawa quark mixing matrix, $|V_{ts}|$. The present values of the C-K-M matrix elements suggest that the oscillation frequency lies in the range $\frac{\Delta M}{\Gamma} \sim 2$ to 265 although the current best estimates give $\frac{\Delta M}{\Gamma} \sim 15$. The OPAL silicon microvertex detector at CERN is used as an example of present day detector technology. The energy lost by an ionizing particle in a silicon wafer is studied in detail. The phenomenon of B_s^0 oscillations was simulated by computer using a simple model. These simulated events were analyzed by three different methods in an attempt to quantify the number of events needed in order to achieve a given precision for the measurement of the B_s^0 oscillation frequency. With 200 B_s^0 mesons detected, a measurement of $\frac{\Delta M}{\Gamma}$ up to 10 can be made with good precision.

Examiners:


Dr. R. K. Keeler, Supervisor (Department of Physics and Astronomy)


Dr. A. Astbury, Departmental Member (Department of Physics and Astronomy)


Dr. G. Beer, Departmental Member (Department of Physics and Astronomy)


Dr. D. Patman, Departmental Member (Department of Physics and Astronomy)


Dr. H. Kwok, Outside Member (Department of Electrical Engineering)


Dr. S. Page, External Examiner (Department of Physics, University of Manitoba)

Table of Contents

Abstract	ii
Table of Contents	iii
List of Tables	iv
List of Figures	vii
Acknowledgement	xvii
Dedication	xviii
1 Introduction	1
2 B Meson Flavor Oscillations	15
3 The OPAL Detector	38
4 Silicon Vertex Detector Analysis and Results	49
5 B_s^0 Oscillation Simulations and Analyses	64
6 B Meson Oscillation Simulation Results	89
7 Summary of Results	131
Bibliography	136
Appendix A: Landau Energy Loss Theory	140
Appendix B: Simulation Results	144

List of Tables

1.1	<i>Properties of the B_s^0 meson. The lifetime and the mass values are obtained from reference [1]. Virtually nothing has been experimentally confirmed about the B_s^0.</i>	1
1.2	<i>Table of vector and axial-vector coupling constants assuming $\sin^2 \theta_w \approx 0.22$.</i>	8
1.3	<i>B mesons and their quark content. Antiparticles are formed by the interchange of quark and antiquark e.g. $B^- = (b\bar{u})$.</i>	10
1.4	<i>D mesons and their quark content. Antiparticles are formed as explained in table 1.3.</i>	10
2.1	<i>Estimated branching ratios of the different processes from reference [17]. \bar{X}_b is an antibaryon which contains a \bar{b} quark.</i>	26
2.2	<i>The number of dilepton events produced. Muons can be reconstructed with an efficiency of $\epsilon \approx 0.75$ and electrons with an efficiency of $\epsilon \approx 0.55$ [24]. Assuming that electrons and muons are created from B mesons in equal quantities, then $\epsilon_1 \epsilon_2 \approx \frac{1}{2}(0.75)(0.55) + \frac{1}{4}(0.75)(0.75) + \frac{1}{4}(0.55)(0.55) = 0.42$.</i>	27
2.3	<i>Some branching ratios of D_s^+ and ϕ mesons.</i>	28
2.4	<i>The number of dileptons produced with a D_s tagged on one side.</i>	30

2.5	<i>Decays of the B meson for the primary kaon method. X is any particle including another kaon.</i>	34
4.1	<i>Table of most probable values of the convoluted Landau distribution found by the iteration scheme. The errors given in this table represent the smallest step size used when trying to find the MPV.</i>	56
4.2	<i>Table of output parameters of the convoluted Landau distributions fitted to the experimental energy loss histograms.</i>	56
4.3	<i>Table of σ_{noise} values from the fits of the energy loss distributions. .</i>	57
4.4	<i>Table of σ_{noise} values from the truncated Gaussian fit of the peak. .</i>	58
4.5	<i>Table of mean values of the noise sum per cluster distributions. . . .</i>	59
6.1	<i>Table of runs performed with the fitting program.</i>	96
6.2	<i>Table of fitting method runs which have 90 percent of events within $\pm 3\sigma$. This table compares the mean, the error on the mean found by the fitting procedure, and the σ of the Gaussian fit with the mean and and the SD of the entire reconstructed ω/τ distribution.</i>	105
6.3	<i>Table of runs performed with the folding program.</i>	108
6.4	<i>Table of runs performed with the FFT program.</i>	118
6.5	<i>Table of comparison of the parameters used by Moser and the parameters used in this thesis for the FFT method.</i>	129
B.1	<i>Table of runs performed with the fitting program.</i>	144

B.2	<i>Results of runs performed with the fitting program. The first three columns show the run number, the number of events per data set, and the ω/τ used when generating the data. The next four columns show the output ω/τ and the sigma from the Gaussian fit of the reconstructed ω/τ distribution along with the associated errors. The next column shows the percent of events which were within $\pm 3\sigma$ of mean of the Gaussian-like distribution in the reconstructed ω/τ distribution. The last two columns show the mean and the standard deviation of the whole reconstructed ω/τ distribution.</i>	147
B.3	<i>Table of runs performed with the folding program.</i>	148
B.4	<i>Results of runs performed with the folding program. The first three columns show the run number, the number of events per data set, and the ω/τ used when generating the data. The next four columns show the output ω/τ and the sigma from the Gaussian fit of the folding frequency distribution along with the associated errors. The next column shows the percent of events which were within $\pm 3\sigma$ of mean of the Gaussian-like distribution in the folding frequency distribution. The last two columns show the mean and the standard deviation of the whole folding frequency distribution.</i>	150
B.5	<i>Table of runs performed with the FFT program.</i>	151
B.6	<i>Results of runs performed with the FFT program. The first three columns show the run number, the number of events per data set, and the ω/τ used when generating the data. The last two columns show the mean and the standard deviation of the whole FFT peak frequency distribution.</i>	154

List of Figures

1.1	The Feynman diagram for the reaction $e^+e^- \rightarrow Z^0 \rightarrow$ (quarks and leptons). In this diagram, $f\text{-}\bar{f}$ represents a quark-antiquark pair or a lepton-antilepton pair.	3
1.2	The variation of the e^+e^- cross section as a function of center of mass energy from reference [2].	4
1.3	The coupling of a boson with two fermions. The vertex factor of this electroweak interaction is $-\frac{ig_W}{2\sqrt{2}}\gamma^\mu(1 - \gamma^5)V_{cs}$ where g_W is the weak coupling constant.	10
1.4	The spectator model view of the decay of a B meson to a D meson and a lepton-neutrino pair where q represents any light quark.	11
1.5	Feynman diagram with the largest contribution to the rate of $B_s^0 \rightarrow D_s^- X$	13
2.1	The time evolution of a B_s^0 (equation (2.12)) for $\omega = \frac{1}{2}(\frac{\Delta M}{\Gamma}) = 1$ and 3. A lifetime of 1.37 ps is assumed.	19
2.2	Box diagrams for $B_s^0 - \bar{B}_s^0$ flavor oscillation including the dominant C-K-M vertex elements. In the left box diagram, a W^+ moves counter-clockwise and a W^- moves clockwise and vice versa for the right box diagram.	20

2.3	Diagrams showing the dilepton tagging of B_s^0 flavor oscillation. B mesons are produced in pairs at the interaction region; hence, in a) no flavor oscillation occurs and so the leptons have opposite signs. In b) flavor oscillation occurs hence the leptons have the same sign. . .	24
2.4	Diagrams of the processes which yield B_s^0 mesons. In this diagram, $q = u$ or d	25
2.5	The spectator decay of a b antibaryon, \bar{X}_b , where \bar{Q} represents two light quarks.	27
2.6	Figure showing the relative abundance of leptons as a function of p_T coming from various sources [25]. Note that for $p_T > 1.2$ GeV/c, the majority of leptons come from $b \rightarrow l$	29
2.7	Diagram of an example of a D_s^+ produced by the decay of a B_d^0	31
2.8	Diagrams of the production of leading kaons with (a) the \bar{B}_s^0 , (b) the B^- , (c) the \bar{B}_d^0 , and (d) the oscillation $B_s^0 - \bar{B}_s^0$. Diagram c) cannot have a leading charged kaon.	33
3.1	Diagram of the OPAL detector at the CERN laboratory in Switzerland from reference [29].	39
3.2	Diagram of the orientation of the ladders on the barrels of the OPAL silicon microvertex detector. The distance from the center of the beam pipe to the 1.1 mm Be beam pipe is 5.35 cm. The distance from the center of the beam pipe to the inner barrel and to the outer barrel are 6.08 cm and 7.52 cm respectively.	42
3.3	A diagram of a silicon wafer taken from reference [31].	43

3.4	<i>The layout of the test beam run which tested the performance of the silicon microvertex detector at the PS accelerator at CERN. The two outer detectors are FOXFET detectors equipped with 5 MX3 chips each while the inner FOXFET detector has 5 MX5 chips. A 5 GeV/c π beam was incident on these detectors. The separation distance between detector 1 and 2 is 2.54 ± 0.01 cm and the distance between detector 2 and 3 is 2.50 ± 0.01 cm.</i>	45
3.5	<i>Plot of a Landau distribution for 5 GeV/c pions in 300 μm of silicon. $\phi(\lambda)$ is the Landau integral shown in equation (A.7).</i>	47
4.1	<i>Distribution of the lowest χ^2 of the tracks. This figure is referred to as a pseudo χ^2 because σ_i was ignored in the fit.</i>	51
4.2	<i>Distribution of cluster pulse height sums. It should be noted that detector 2 was read out via an MX5 chip which has a larger gain than the MX3 chips used to readout detectors 1 and 3.</i>	52
4.3	<i>The distribution of cluster pulse height sums fitted to a Landau distribution convoluted with a Gaussian distribution.</i>	55
4.4	<i>Detector by detector comparison of the σ_T from the least square fits.</i>	56
4.5	<i>Distribution of the noise sum per cluster calculated at the pedestal level.</i>	58
4.6	<i>Schematic cross section of part of the OPAL detector. $L_1 = 60.8$ mm, $L_2 = 14.4$ mm, $\sigma_1 = \sigma_2 = 4.1$ μm.</i>	62

5.1 *Probability distribution of observing a non-oscillating B^0 for $\frac{\omega}{\tau} = 2.19 \text{ ps}^{-1}$ and $\tau = 1.37 \text{ ps}$ with: a) no mistagging, no smearing, and no flat background; b) 10 percent mistagging, no smearing, and no flat background; c) 10 percent mistagging, 10 percent smearing, and no flat background; and d) 10 percent mistagging, 10 percent smearing, and 10 percent flat background. The area under these curves is 1. Note the change in scale in the y-axis of these curves.* 73

5.2 *A high statistics run for the fitting method where the fitting function is superposed on the 10000 generated data for the input parameters: $\frac{\omega}{\tau} = 2.19 \text{ ps}^{-1}$, $\sigma = 0.13$ $\tau = 1.37 \text{ ps}$, mistagging = 0.10, background = 0.10, and 0.1 ps bin size. The output parameters of the fit were: $\omega/\tau = (2.19 \pm 0.01) \text{ ps}^{-1}$, mistagging = 0.10 ± 0.01 , and background = 0.10 ± 0.01* 76

5.3 *Results of high statistics fits with the fitting method which were repeated for 10 sets of 10000 events. The 10000 events for each fit were generated with the input parameters: $\frac{\omega}{\tau} = 2.19 \text{ ps}^{-1}$, $\sigma = 0.13$ $\tau = 1.37 \text{ ps}$, mistagging = 0.10, background = 0.10, and 0.2 ps bin size. The mean and standard deviation (SD) values for the output parameters of the fit were: mean = 2.19 ps^{-1} and SD = 0.01 ps^{-1} for the output ω/τ distribution, mean = 0.10 and SD = 0.01 for the output mistagging distribution, and mean = 0.1 and SD = 0.01 for the output background distribution.* 77

5.4 *a) Distribution binned with bin size $x_{bin} \approx 0.2 \text{ ps}$ for $\frac{\omega}{\tau} = 2.19 \text{ ps}^{-1}$, $\sigma = 0.13$ $\tau = 1.37 \text{ ps}$, 10 percent mistagging, and 10 percent background. b) The distribution in a) is divided into intervals of $x_{int} \approx 1.4 \text{ ps}$. c) The resulting distribution after folding.* 79

5.5 Results of high statistics runs with the folding method on a $\cos^2(\frac{\omega}{\tau}t)$ distribution which were repeated for 25 sets of 10000 events. The input ω/τ was 2.19 ps^{-1} with a 0.03 ps bin size. The mean of the output frequency distribution which has a bin size of 0.05 ps^{-1} is 2.20 ps^{-1} with a standard deviation of 0.02 ps^{-1} 82

5.6 Results of high statistics runs with the folding method which were repeated for 100 sets of 10000 events. The 10000 events for each folding were generated with the input parameters: $\frac{\omega}{\tau} = 2.19 \text{ ps}^{-1}$, $\sigma = 0.13 \text{ ps}$, $\tau = 1.37 \text{ ps}$, mistagging = 0.10, background = 0.10, and 0.03 ps bin size. The mean and standard deviation values for the output frequency distribution which has a 0.05 ps^{-1} bin size are 2.34 ps^{-1} and 0.09 ps^{-1} respectively. 83

5.7 a) Amplitude distribution from an FFT applied to 50000 events binned into 0.2 ps bins for $\frac{\omega}{\tau} = 2.19 \text{ ps}^{-1}$, $\sigma = 0.13 \text{ ps}$, $\tau = 1.37 \text{ ps}$, 10 percent mistagging, 10 percent background, and frequency bin size of 0.12 ps^{-1} . The arrow shows the peak frequency at 2.28 ps^{-1} . b) Amplitude distribution from an FFT applied to 50000 events with the exponential term subtracted and binned into 0.2 ps bins for $\frac{\omega}{\tau} = 2.19 \text{ ps}^{-1}$, $\sigma = 0.13 \text{ ps}$, $\tau = 1.37 \text{ ps}$, 10 percent mistagging, 10 percent background, and frequency bin size of 0.12 ps^{-1} . The arrow shows the peak frequency at 2.28 ps^{-1} 87

- 5.8 a) Amplitude distribution from an FFT applied to 50000 events binned into 0.16 ps bins for $\frac{\omega}{\tau} = 2.19 \text{ ps}^{-1}$, $\sigma = 0.13 \text{ ps}$, $\tau = 1.37 \text{ ps}$, 10 percent mistagging, 10 percent background, and frequency bin size of 0.6 ps^{-1} . The arrow shows the peak frequency at 2.32 ps^{-1} . b) Amplitude distribution from an FFT applied to 50000 events with the exponential term subtracted and binned into 0.16 ps bins for $\frac{\omega}{\tau} = 2.19 \text{ ps}^{-1}$, $\sigma = 0.13 \text{ ps}$, $\tau = 1.37 \text{ ps}$, 10 percent mistagging, 10 percent background, and frequency bin size of 0.6 ps^{-1} . The arrow shows the peak frequency at 2.32 ps^{-1} 88
- 6.1 a) A typical output frequency distribution for the fitting Monte Carlo with input $\frac{\omega}{\tau} = 0.73 \text{ ps}^{-1}$ and where 100 sets of 25 sample events were used. b) A low frequency (input $\frac{\omega}{\tau} = 0.73 \text{ ps}^{-1}$) and high number of events (100 sets of 200 sample events) distribution. c) A high frequency (input $\frac{\omega}{\tau} = 5.11 \text{ ps}^{-1}$) and low number of events (100 sets of 25 sample events) distribution. The dashed lines indicate the value of the input ω/τ 91
- 6.2 The fitted ω/τ distribution from the fitting method performed on 100 sets of 200 sample events generated with the parent parameters: $\omega/\tau = 3.65 \text{ ps}^{-1}$, 0.2 ps bin size, 10 percent mistagging and 10 percent background. The mean of this distribution is 3.67 ps^{-1} with an SD of 0.29 ps^{-1} 92

6.3 The fitted ω/τ distribution from the fitting method performed on 100 sets of 200 sample events generated with the parent parameters: $\omega/\tau = 3.65 \text{ ps}^{-1}$, 0.2 ps bin size, 10 percent mistagging and 10 percent background. The fit was performed with the mistagging and background fixed at zero. The mean of this distribution is 3.66 ps^{-1} with an SD of 0.05 ps^{-1} 93

6.4 a) An output frequency distribution for the fitting program with input $\frac{\omega}{\tau} = 0.73 \text{ ps}^{-1}$ and 100 sets of 100 sample events were used. b) The same distribution after the first iteration of the Gaussian fit. c) The same distribution after the second iteration of the Gaussian fit. The fit results with the χ^2 per degree of freedom of the fits are shown in the boxes. 95

6.5 Fitting method plot of the absolute percentage difference of the mean of the output ω/τ distribution from the input ω/τ versus N for an input $\omega/\tau = 2.19 \text{ ps}^{-1}$. The plot converges to zero at large N 97

6.6 Fitting method plot of SD/\sqrt{N} versus N of the output ω/τ distribution for an input $\omega/\tau = 2.19 \text{ ps}^{-1}$. The plot converges to zero for large N and is an increasing function at small N 99

6.7 Fitting method plot of the absolute percentage difference of the mean of the output ω/τ distribution from the input ω/τ averaged over the four runs versus N . Data at $N = 25, 50, 100,$ and 200 have been slightly offset for clarity. Note that there is a change in scale for the y-axis of the upper plot. The three data points at $N = 200$ have error bars which are too small to be displayed. Note that the y-axis starts at -2 percent. 100

6.8	Fitting method plot of SD/\sqrt{N} of the output ω/τ distribution averaged over the four runs versus N	102
6.9	Fitting method plot of the percentage of entries within the $\pm 3\sigma$ region of the output ω/τ distribution versus N for an input $\omega/\tau = 2.19 \text{ ps}^{-1}$. Note that the y-axis starts at 40 percent.	103
6.10	a) A typical output frequency distribution for the folding method with input $\frac{\omega}{\tau} = 5.11 \text{ ps}^{-1}$ and 100 sets of 200 sample events were used. b) A low frequency (input $\frac{\omega}{\tau} = 2.19 \text{ ps}^{-1}$) and high number of events (100 sets of 200 sample events) distribution. c) A high frequency (input $\frac{\omega}{\tau} = 5.11 \text{ ps}^{-1}$) and low number of events (100 sets of 25 sample events) distribution. The dashed lines indicate the value of the input ω/τ	107
6.11	Folding method plot of the absolute percentage difference of the mean from the input ω/τ versus N for an input $\omega/\tau = 2.19 \text{ ps}^{-1}$. Note that the y-axis starts at 10 percent. The plot converges to about 12 percent at $N = 200$	109
6.12	Folding method plot of SD/\sqrt{N} of the folding frequency distribution versus N for an input $\omega/\tau = 2.19 \text{ ps}^{-1}$	111
6.13	Folding method plot of the absolute percentage difference of the mean of the output frequency distribution from the input ω/τ averaged over the three runs versus N . Data at $N = 25, 50, 100,$ and 200 have been slightly offset for clarity. Note that there is a change in scale for the y-axis of the upper plot.	112
6.14	Folding method plot of SD/\sqrt{N} averaged over the three runs versus N	114

6.15 *Folding method plot of the percentage of entries within the $\pm 3\sigma$ region versus N for an input $\omega/\tau = 2.19 \text{ ps}^{-1}$. Note that the y-axis starts at 20 percent.* 115

6.16 a) *An output frequency distribution for the FFT method with input $\frac{\omega}{\tau} = 3.65 \text{ ps}^{-1}$ and 100 sets of 200 sample events were used. b) Another output frequency distribution with input $\frac{\omega}{\tau} = 3.65 \text{ ps}^{-1}$ and 100 sets of 25 sample events were used. The dashed lines indicate the value of the input $\frac{\omega}{\tau}$* 117

6.17 *FFT method plot of the absolute percentage difference of the mean of the peak frequency distributions from the input ω/τ versus N for an input $\omega/\tau = 2.19 \text{ ps}^{-1}$. Since the peak frequencies were measured at the upper edge of a frequency bin, the mean values used in this plot were shifted by half a frequency bin width (0.3 ps^{-1}) from the values in Appendix B to give the value of the peak frequency at the center of the bin. The plot converges to zero percent at $N = 200$. . .* 119

6.18 a) *Amplitude distribution from an FFT applied to 200 events binned into 0.16 ps bins for $\frac{\omega}{\tau} = 2.19 \text{ ps}^{-1}$, $\sigma = 0.13 \text{ ps}$, $\tau = 1.37 \text{ ps}$, 10 percent mistagging, 10 percent background, and frequency bin size of 0.6 ps^{-1} . The arrow shows the peak frequency at 2.25 ps^{-1} . (Divide the peak value by two to get the frequency.) b) Amplitude distribution from an FFT applied to the same 200 events with the exponential term subtracted and binned into 0.16 ps bins for $\frac{\omega}{\tau} = 2.19 \text{ ps}^{-1}$, $\sigma = 0.13 \text{ ps}$, $\tau = 1.37 \text{ ps}$, 10 percent mistagging, 10 percent background, and frequency bin size of 0.6 ps^{-1} . The peak at 2.25 ps^{-1} has disappeared.* 121

6.19	<i>FFT method plot of the absolute percentage difference of the mean of the peak frequency distributions with the exponential term subtracted from the input ω/τ versus N for an input $\omega/\tau = 2.19 \text{ ps}^{-1}$. The plot converges to zero percent at $N = 200$. The mean values in these plots were also shifted by half a bin as described in figure 6.17.</i>	122
6.20	<i>FFT method plot of SD/\sqrt{N} of the peak frequency distribution versus N for an input $\omega/\tau = 2.19 \text{ ps}^{-1}$.</i>	123
6.21	<i>FFT method plot of SD/\sqrt{N} of the peak frequency distribution with the exponential term subtracted versus N for an input $\omega/\tau = 2.19 \text{ ps}^{-1}$.</i>	125
6.22	<i>FFT method plot of the absolute percentage difference of the mean of the output frequency distribution from the input ω/τ averaged over the four runs versus N. Data at $N = 25, 50, 100,$ and 200 have been slightly offset for clarity. Note that there is a change in scale for the y-axis of the upper plot. Note that the y-axis starts at -10 percent. The mean values in these plots were also shifted by half a bin as described in figure 6.17.</i>	126
6.23	<i>FFT method plot of SD/\sqrt{N} averaged over the four runs versus N. Data at $N = 25, 50, 100,$ and 200 have been slightly offset for clarity.</i>	127
7.1	<i>The number of events needed to satisfy the 90 percent Gaussian criterion for varying $\frac{\Delta M}{\Gamma}$ based on the results from the fitting method.</i>	134
A.1	<i>Plot of a Landau distribution for 5 GeV/c pions in 300 μm of silicon. $\phi(\lambda)$ is the Landau integral shown in equation (A.7).</i>	143

Acknowledgments

Many thanks go to Richard Keeler for guiding me in my work and for showing me the basics of particle physics. My work with the silicon microvertex detector could not have been accomplished without the help of Christian Moisan and Chris Oram. I am grateful to them. Learning to use the Apollo computers and the PAW package was made easy with the careful instructions of Myron Rosvick. I thank him. I would like to acknowledge the help that I received from my fellow UVic OPALites. Finally, I would like to thank my office mates Sean Bohun and Mark Welsh for their mathematical genius, helpful hints and suggestions, and their moral support.

Dedication

To Hans Kamper and Norman Lewis who make physics look easy and fun and to Danny who was my faithful canine companion throughout the grind of undergraduate physics.

Chapter 1

Introduction

1.1 Introduction

This thesis explores the possibility of measuring the frequency of oscillation of $B_s^0 - \bar{B}_s^0$ mixing given existing detector technology. The B_s^0 meson is a particle consisting of an anti-b quark and an s quark. Table 1.1 shows the properties of the B_s^0 , which has the ability to oscillate within its lifetime between the particle and antiparticle state via a second order weak transition. The oscillation frequency of B_s^0 mixing has not yet been measured. The mean lifetime of the B_s^0 meson is not measured explicitly. However the lifetime, averaged over all possible B mesons, is measured to be about 1.37 ps. Theory suggests that the variation in the values of the individual

B_s^0 MESON		
$I(J^P)$	$\frac{1}{2}(0^-)$	(theory)
Lifetime	$\sim (0.97 - 1.61)$ ps	(experiment)
Mass	$\sim (5.36 - 5.41)$ GeV/c ²	(experiment)

Table 1.1: *Properties of the B_s^0 meson. The lifetime and the mass values are obtained from reference [1]. Virtually nothing has been experimentally confirmed about the B_s^0 .*

lifetimes of the different types of B mesons from the measured average lifetime will be about 10 percent. Present experiments show a variation of about 25 percent. It is expected that the lifetime of the B_s^0 will be known to a much better precision by the time a measurement of B_s^0 oscillation frequency can be made. A measurement of the oscillation frequency is important since, in conjunction with other measurements, it leads to the determination of $|V_{ts}|$, an element of the Cabibbo-Kobayashi-Maskawa quark mixing matrix. The detectors at LEP, the Large Electron (e^-) Positron (e^+) collider at the CERN laboratory in Switzerland, should soon detect enough B_s^0 events to allow a measurement of this oscillation effect.

In this thesis, the phenomenon of B_s^0 oscillations is simulated with a simple model by generating a signal and a background with statistics and resolutions which are typical of the LEP collider and LEP detectors. These simulated events are analyzed in an attempt to quantify the number of events necessary to achieve a given precision for measuring the B_s^0 oscillation frequency.

The LEP collider makes it possible to measure the B_s^0 oscillation effect. It operates at an energy equal to the mass of the Z^0 (the carrier of the neutral component of the weak force) to produce the reaction $e^+e^- \rightarrow Z^0 \rightarrow$ (quarks or leptons) (see figure 1.1 for the Feynman diagram for this reaction). Figure 1.2 [2] shows that a collider operating at the Z^0 mass has a large enhancement in cross section. The LEP accelerator operates currently at a maximum luminosity of about $1.0 \times 10^{31} \text{ cm}^{-2}\text{s}^{-1}$ (with a designed luminosity of $1.6 \times 10^{31} \text{ cm}^{-2}\text{s}^{-1}$ and a designed Z^0 rate of 0.5 Hz for multihadron events) resulting in a Z^0 rate of about 0.3 Hz for multihadron events. The B_s^0 mesons produced in the chain $e^+e^- \rightarrow Z^0 \rightarrow b\bar{b} \rightarrow B_s^0 X$ (where X is any particle) can be created in sufficient quantities to measure the oscillation effect.

OPAL is one of the four detectors in use at LEP. The OPAL detector is a solenoidal magnetic spectrometer surrounded by energy absorbing detectors opti-

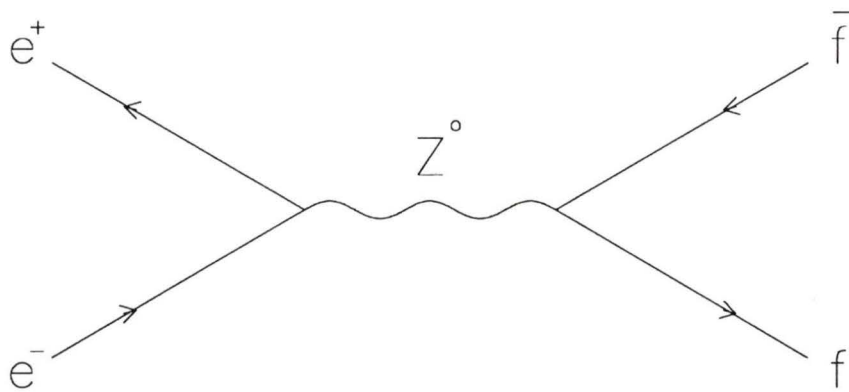


Figure 1.1: The Feynman diagram for the reaction $e^+e^- \rightarrow Z^0 \rightarrow (quarks \text{ and leptons})$. In this diagram, $f\text{-}\bar{f}$ represents a quark-antiquark pair or a lepton-antilepton pair.

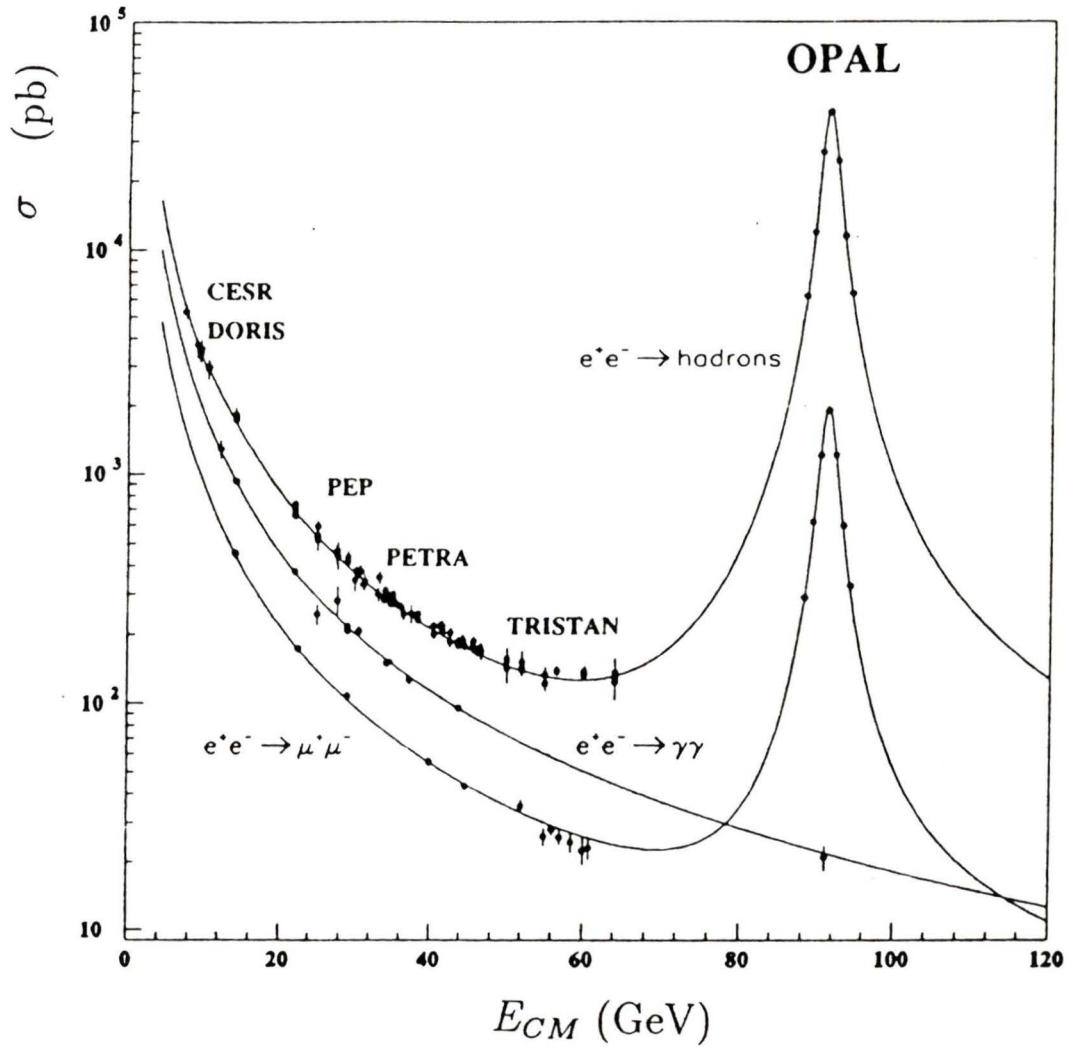


Figure 1.2: The variation of the e^+e^- cross section as a function of center of mass energy from reference [2].

mized to measure the energy of photons (γ), electrons, and positrons. The exterior layer of the detector is a muon detector which measures the momentum and position of muons which penetrate the energy absorbing layers. Two layers of silicon strip microvertex detectors were recently installed at the center of the detector around the beam pipe. These detectors have an intrinsic position resolution for charged particles of about $4 \mu\text{m}$. Due to this excellent spatial resolution, these detectors can reconstruct the flight path of the decay products of the B_s^0 which then leads to the determination of the decay length of the B_s^0 . A typical value for this decay length for a B_s^0 produced at LEP energies is 2.2 mm. The spatial resolution of this detector affects the ability to measure the B_s^0 decay length. The author worked on tests of this detector which confirmed that the measured energy loss of ionizing particles in the detector agrees with the expected Landau theory of energy loss. The results of this work will also be given in this thesis.

1.2 The Standard Model

The reaction $e^+e^- \rightarrow Z^0$ proceeds via the electroweak interaction. The electroweak force acts on all elementary spin $\frac{1}{2}$ particles, called fermions (f), via the exchange of vector gauge bosons (γ , W^\pm , and Z^0). The twelve elementary fermions fit into three families

$$\begin{pmatrix} u \\ d \\ e \\ \nu_e \end{pmatrix} \begin{pmatrix} c \\ s \\ \mu \\ \nu_\mu \end{pmatrix} \begin{pmatrix} t \\ b \\ \tau \\ \nu_\tau \end{pmatrix} \quad (1.1)$$

where u , c , and t are quarks with an electrical charge of $\frac{2}{3}e$; d , s , and b are quarks with an electrical charge of $-\frac{1}{3}e$; e , μ , and τ are charged leptons; and ν_e , ν_μ , and ν_τ are neutral leptons called neutrinos. The neutrinos are assumed to be massless. All particles have an antiparticle counterpart and the six different types of quarks are

called flavors.

The work of Glashow, Weinberg, and Salam [3, 4, 5] led to the Standard Model, in which the weak coupling of intermediate vector bosons to leptons and quarks was related to the coupling of the photon, thereby unifying the weak and electromagnetic forces. As a consequence, a good prediction of the masses of the intermediate vector bosons followed: $M_W = 82 \pm 2 \text{ GeV}/c^2$ and $M_Z = 92 \pm 2 \text{ GeV}/c^2$ [6]. The discovery of the W^\pm and Z^0 in 1983 [7, 8, 9] confirmed the theory. Currently, the most precise values for the masses are measured as $M_W = 80.6 \pm 0.4 \text{ GeV}/c^2$ and $M_Z = 91.161 \pm 0.031 \text{ GeV}/c^2$ [10]. These gauge bosons, like the photon, have a spin of 1. The weak coupling constant, g_w is related to the electromagnetic coupling constant, g_e by the equation $g_e = g_w \sin \theta_w$ where θ_w is the Weinberg weak mixing angle.

The Standard Model is a gauge theory which explains the interactions of the elementary particles via three of the four forces of nature; the electromagnetic interaction and the weak interaction, which have been joined to form the electroweak interaction, and the strong interaction. The Standard Model has eighteen parameters which must be measured by experiment: 3 coupling constants, 6 quark masses, 3 lepton masses, 3 quark mixing angles plus a phase, a weak mixing angle (θ_w), and the mass of the Higgs particle.

Leptons do not feel the strong force which acts only on quarks that carry one of three charge values called “color”. The strong force is mediated by the exchange of colored gluons. The strong force binds quarks to produce colorless particles called hadrons. A quark can combine with an antiquark ($q_1 \bar{q}_2$) to produce integral spin particles called mesons which obey Bose-Einstein statistics. Three quarks can combine ($q_1 q_2 q_3$) to form half-integral spin particles called baryons which obey Fermi-Dirac statistics. The strong force can be described phenomenologically by a potential of the form $-\frac{4\alpha_s}{3r} + kr$ where k is a constant and α_s is the strong coupling constant.

The first term dominates at small r ($r \ll 1$ fm) and arises from the exchange of one gluon. The second term is a confining term which dominates at large r . It has the consequence that any attempt to liberate a single quark from a hadron results in the production of a color-charge neutral $q\bar{q}$ pair from the vacuum. Since mesons are color neutral, the nuclear force can be regarded as the residual effect of the strong force. At LEP, these color neutral mesons appear in the detector as jets of particles produced via a process called fragmentation of primordial quarks.

All leptons couple identically to the W^\pm in the weak interaction and all charged leptons couple identically to the γ in the electromagnetic interaction. However, the coupling of quarks and leptons to the Z^0 depends on the charge, Q^f , and value of the weak isotopic spin, I_3^f , of the quark or lepton. These couplings terms are [11]

$$C_V = I_3^f - 2Q^f \sin^2 \theta_W \quad (1.2)$$

and

$$C_A = I_3^f \quad (1.3)$$

where C_V and C_A are the vector and axial-vector coupling constants of the fermions, f , to the Z^0 . These values for $\sin^2 \theta_w \approx 0.22$ are given in table 1.2 [11]. The partial width of the Z^0 to a given fermion/antifermion pair ($Z^0 \rightarrow f\bar{f}$ where f can be a quark or a lepton) can be written in terms of the width to neutrinos [11]

$$\Gamma(Z^0 \rightarrow f\bar{f}) = \Gamma(Z^0 \rightarrow \nu\bar{\nu}) 2 (C_V^2 + C_A^2)_f N_c. \quad (1.4)$$

where N_c , a color factor, is 1 for e , μ , and τ and 3 for u , d , c , s , and b . Due to the strong force, all six quark flavors can exist in one of three color charges and hence each possible color state of the quarks must be treated as an independent quark state. The total width of the Z^0 is $\Gamma_Z = 2.6$ GeV where $\Gamma(Z^0 \rightarrow \nu\bar{\nu}) \approx 160$ MeV, $\Gamma(Z^0 \rightarrow l\bar{l}) \approx 80$ MeV, $\Gamma(Z^0 \rightarrow u\bar{u}, c\bar{c}, \text{ or } t\bar{t}) \approx 275$ MeV, and $\Gamma(Z^0 \rightarrow d\bar{d}, s\bar{s}, \text{ or } b\bar{b}) \approx$

Fermions	$2C_V$	$2C_A$	$C_V^2 + C_A^2$
ν_e, ν_μ, ν_τ	1	1	0.5
e, μ, τ	$-1 + 4\sin^2\theta_w$	-1	0.25
u, c, t	$1 - \frac{8}{3}\sin^2\theta_w$	1	0.29
d, s, b	$-1 + \frac{4}{3}\sin^2\theta_w$	-1	0.37

Table 1.2: Table of vector and axial-vector coupling constants assuming $\sin^2\theta_w \approx 0.22$.

355 MeV. These values predict branching ratios to individual charged leptons of approximately 3 percent. The total fraction of Z^0 decays to hadrons is 70 percent. The ratio of widths is $\Gamma_{l\bar{l}} : \Gamma_{\nu\bar{\nu}} : \Gamma_{u\bar{u},c\bar{c},t\bar{t}} : \Gamma_{d\bar{d},s\bar{s},b\bar{b}} = 1 : 2 : 3.5 : 4.5$. Hence, the branching ratio is higher for the d, s, b quarks than for the u, c, t quarks. It must be emphasized that free quarks are not observed. Quarks are only observed in hadrons.

1.3 The Decays of B mesons

Flavor is not conserved by the charged weak interaction (*i.e.* the exchange of W^\pm). The mass eigenstates of the quarks are used to form hadrons. However, the weak interaction sees a mixture of the mass eigenstates and this mixing is conventionally represented by the Cabibbo-Kobayashi-Maskawa (C-K-M) matrix, V

$$\begin{pmatrix} d' \\ s' \\ b' \end{pmatrix} = V \begin{pmatrix} d \\ s \\ b \end{pmatrix} = \begin{pmatrix} V_{ud} & V_{us} & V_{ub} \\ V_{cd} & V_{cs} & V_{cb} \\ V_{td} & V_{ts} & V_{tb} \end{pmatrix} \begin{pmatrix} d \\ s \\ b \end{pmatrix} \quad (1.5)$$

where primed quarks are the weak eigenstates and the unprimed quarks are the mass eigenstates. By convention, the quarks with a charge of $\frac{2}{3}$ (u, c, and t quarks) do not mix while the quarks with a charge of $-\frac{1}{3}$ (d, s, and b quarks) do mix. Limits have been placed on the magnitudes of these matrix elements by experiment and by

unitarity [12]

$$|V_{ij}| = \begin{pmatrix} 0.9747 - 0.9759 & 0.218 - 0.224 & 0.001 - 0.007 \\ 0.218 - 0.224 & 0.9734 - 0.9752 & 0.030 - 0.058 \\ 0.003 - 0.019 & 0.029 - 0.058 & 0.9983 - 0.9996 \end{pmatrix} \quad (1.6)$$

The C-K-M matrix can be parameterized as [12]

$$V = \begin{pmatrix} c_{12}c_{13} & s_{12}c_{13} & s_{13}e^{-i\delta_{13}} \\ -s_{12}c_{23} - c_{12}s_{23}s_{13}e^{i\delta_{13}} & c_{12}c_{23} - s_{12}s_{23}s_{13}e^{i\delta_{13}} & s_{23}c_{13} \\ s_{12}s_{23} - c_{12}c_{23}s_{13}e^{i\delta_{13}} & -c_{12}s_{23} - s_{12}c_{23}s_{13}e^{i\delta_{13}} & c_{23}c_{13} \end{pmatrix} \quad (1.7)$$

where $c_{ij} = \cos \theta_{ij}$, $s_{ij} = \sin \theta_{ij}$, and $i, j = 1, 2$, or 3 . δ_{13} is a phase angle and θ_{ij} represents the mixing angle between the quark generations. In the limit $\theta_{23} = \theta_{13} = 0$, then $|V_{ub}|$, $|V_{cb}|$, $|V_{ts}|$, and $|V_{td}|$ go to zero and so only the d and the s quarks mix in a manner given by the quantity known as the Cabibbo angle $\theta_c = \theta_{12} \approx 13.1^\circ$. The signs of the elements of the C-K-M matrix in equation (1.6) are determined by the phase angle. This phase provides a possible explanation for the phenomenon of charge-parity violation in the weak interaction. The C-K-M matrix elements give the relative strength of the electroweak interaction between interacting fermions and the exchange bosons (see figure 1.3). The two C-K-M matrix elements which are relevant to B_s^0 mesons are $|V_{ts}|$ and $|V_{tb}|$. It is hoped that a measurement of B_s^0 oscillations combined with the existing measurement of B_d^0 oscillations will lead to the determination of $|V_{ts}|$.

A \bar{b} quark can combine with either a u , d , s , or c to produce a B meson. A b and a \bar{b} can also join to form an Υ . The naming scheme for B mesons is given in table 1.3. The B^+ and the B^0 mesons have a measured mass of about $5.279 \text{ GeV}/c^2$. The predominant weak decays of the B mesons are to the D mesons (the naming scheme of the D mesons is given in table 1.4). The decay of a B meson to a D meson can be understood by the use of the spectator model. This model is based on the fact that the mass of the b quark is large compared to that of the other

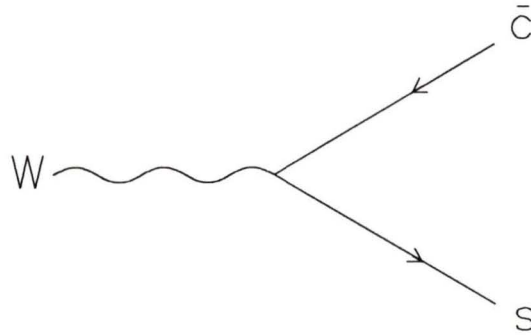


Figure 1.3: The coupling of a boson with two fermions. The vertex factor of this electroweak interaction is $-\frac{ig_W}{2\sqrt{2}}\gamma^\mu(1-\gamma^5)V_{cs}$ where g_W is the weak coupling constant.

MESON	QUARKS
B^+	$\bar{b}u$
B_d^0	$\bar{b}d$
B_s^0	$\bar{b}s$
B_c^+	$\bar{b}c$

Table 1.3: B mesons and their quark content. Antiparticles are formed by the interchange of quark and antiquark e.g. $B^- = (b\bar{u})$.

MESON	QUARKS
D^0	$c\bar{u}$
D^+	$c\bar{d}$
D_s^+	$c\bar{s}$

Table 1.4: D mesons and their quark content. Antiparticles are formed as explained in table 1.3.

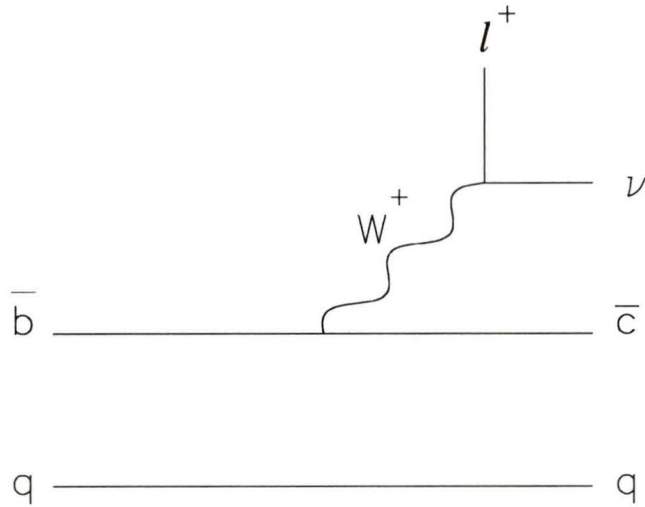


Figure 1.4: *The spectator model view of the decay of a B meson to a D meson and a lepton-neutrino pair where q represents any light quark.*

quark which forms the B meson. The heavy b quark carries most of the momentum while the lighter quark is treated as a spectator that does not participate in the decay. Because the b quark and the light spectator quark are bound close together and the strong force gets weaker at smaller distances, the b quark decays as if it were a free particle. Hence, the decay of the B meson is determined by the decay of the b quark (see figure 1.4 for the Feynman diagram of the spectator decay of a B meson). This decay occurs by the flavor-changing charged current provided by the W^\pm . The coupling of the b quark to other quarks is given by the elements of the C-K-M matrix. The values of the elements $|V_{ub}|$ and $|V_{cb}|$ give the rates for a b quark to decay to a u or a c quark respectively. In equation (1.6), it can be seen that $|V_{cb}|$ is greater than $|V_{ub}|$ and so a b quark mainly decays to a c quark. Similarly, the spectator model can also be applied to the decays of D mesons where the companion quark to the charm quark is light compared with the c . The values for the C-K-M

elements $|V_{cd}|$ and $|V_{cs}|$ give the rates for a c quark to decay to a d or an s quark. Since $|V_{cs}| \approx 1$, the dominant decay is a c quark is to an s quark. Experiments show that the spectator model does not appear to work as well for the c quark mesons as for the b quark mesons.

1.4 The Production of B mesons in e^+e^- Collisions

There are several ways of producing $b\bar{b}$ pairs. LEP produces $b\bar{b}$ pairs by operating on the Z^0 resonance. Other machines such as CESR (at Cornell) and DORIS (in Hamburg) are e^+e^- machines which operate at the $\Upsilon(4s)$ resonance. Pairs of $b\bar{b}$ quarks can also be created from the vacuum by running at energies above the $b\bar{b}$ production threshold. The relative probability of $b\bar{b}$ production from the vacuum compared to other quark pairs is given by the relative square of the quark charges $\left(\frac{e_b}{e_q}\right)^2$ where e_b is the charge of the b quark and e_q is the charge of the other quark. There are many reasons why it may be preferable to work at the Z^0 resonance as opposed to the $\Upsilon(4s)$ resonance. The observed cross section at the $\Upsilon(4s)$ is about 1 nb on a continuum cross section of 2.5 nb while the absolute $b\bar{b}$ production cross section at the Z^0 resonance is about 6 nb. Also, decay products from $\Upsilon(4s)$ have very small velocities ($\beta \approx 0.06$) [13] whereas the decay products from Z^0 at LEP have a large boost, $\beta \approx 0.98$. Hence, lifetime measurements of B mesons from $\Upsilon(4s)$ are very difficult since the B mesons decay close to the production vertex. The meson of interest in this thesis is the B_s^0 . The B_s^0 mesons are too heavy to be created as a decay product of the $\Upsilon(4s)$ and hence only machines operating well above the $\Upsilon(4s)$ resonance (e.g. LEP at the Z^0 resonance) can produce these particles copiously. The $\Upsilon(5s)$ state with a mass of 10.86 GeV/c² can decay to produce B_s^0 mesons. However, its cross section is only about 0.3 nb on a continuum cross section of 2.5 nb.

The branching ratio for $Z^0 \rightarrow b\bar{b}$ is about 15 percent. Hence from about one

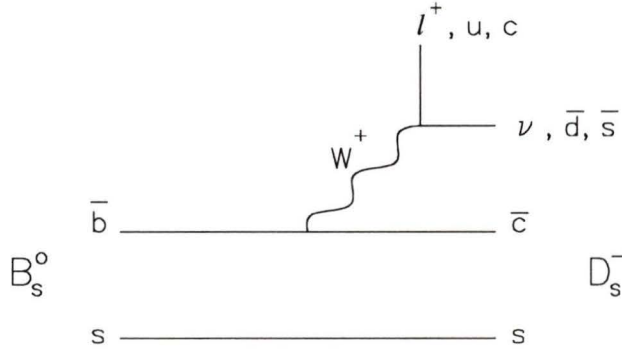


Figure 1.5: Feynman diagram with the largest contribution to the rate of $B_s^0 \rightarrow D_s^- X$.

million Z^0 's per year in the OPAL detector, about $1.5 \times 10^5 \bar{b}\bar{b}$ pairs should be created. The probability of $b \rightarrow B_s^0$ is about 10% and the B_s^0 decays to a D_s^- (a meson with a charmed quark) almost 100% of the time. Therefore, from the reaction $e^+e^- \rightarrow Z^0 \rightarrow \bar{b}\bar{b} \rightarrow B_s^0 X \rightarrow D_s^- X'$ approximately $1.5 \times 10^4 D_s^-$ mesons should emerge as the decay products of the B_s^0 . Figure 1.5 is the Feynman diagram which makes the largest contribution to the $B_s^0 \rightarrow D_s^- X$ decay rate. The B meson decay products (mainly D mesons, leptons and pions) will be emitted in a narrow cone around the direction of the parent B meson.

1.5 Outline of Thesis

In chapter 2, the theory of $B_s^0 - \bar{B}_s^0$ oscillations will be presented. Two methods of finding the particle/antiparticle nature of the B_s^0 at the time of its creation (the

dilepton tagging method and the primary kaon method) will be explored. The measurement of the time of flight of B_s^0 mesons will also be discussed.

The OPAL silicon microvertex detector, which is used as an example of a typical vertex detector at LEP, will be described in chapter 3 along with the energy loss theory appropriate for such a detector. The noise associated with the detector, and how it affects the measurement of the energy lost by ionizing particles in the detector, will also be explained in this chapter.

The energy loss theory developed in chapter 3 will be used in chapter 4 to explain the work which the author performed in confirming that the measured energy loss in the detector agrees with the expected Landau theory.

In chapter 5, programs written by the author will be explained. These programs simulate B_s^0 flavor oscillations. Use is then made of one of three different methods (the fitting method, the folding method, and the Fast Fourier method) to recover the frequency of oscillation of the generated events.

The results of these three methods of analysis applied to generated events representing the anticipated low numbers of B_s^0 mesons will be given in tabular and graphical form in chapter 6 and conclusions will be drawn based on these results.

Finally, the work performed in this thesis will be summarized in chapter 7.

Chapter 2

B Meson Flavor Oscillations

2.1 The Theory of B Meson Mixing

The B^0 and \bar{B}^0 are not eigenstates of the weak interaction since $CP|B^0\rangle \neq \pm|B^0\rangle$ (where C is the charge conjugation operator and P is the parity operator). However, they both can decay weakly to some common states (e.g. $\pi^+\pi^-$ where $CP|\pi^+\pi^-\rangle = |\pi^+\pi^-\rangle$). Because of this, the B_s^0 mesons can oscillate between their particle and antiparticle states in a phenomenon known as mixing. Flavor oscillations have been observed in the $K^0 - \bar{K}^0$ system in 1956 [14] and in the $B_d^0 - \bar{B}_d^0$ system in 1987 [15].

An arbitrary b-flavored state $a|B^0\rangle + b|\bar{B}^0\rangle$ obeys the time-dependent Schrödinger equation [16]

$$i\frac{d}{dt}\begin{pmatrix} a \\ b \end{pmatrix} = \mathcal{H}\begin{pmatrix} a \\ b \end{pmatrix} \quad (2.1)$$

where

$$\mathcal{H} = \mathbf{M} - i\frac{\mathbf{\Gamma}}{2} = \begin{pmatrix} M_{11} - i\frac{\Gamma_{11}}{2} & M_{12} - i\frac{\Gamma_{12}}{2} \\ M_{21} - i\frac{\Gamma_{21}}{2} & M_{22} - i\frac{\Gamma_{22}}{2} \end{pmatrix} \quad (2.2)$$

with $M_{11} = M_{22} = M$ and $\Gamma_{11} = \Gamma_{22} = \Gamma$ due to CPT invariance (they are a particle-antiparticle pair). \mathbf{M} and $\mathbf{\Gamma}$ are Hermitian matrices, hence $M_{21} = M_{12}^*$ and $\Gamma_{21} = \Gamma_{12}^*$, and the off-diagonal terms are not equal to zero if there exist $B \rightarrow \bar{B}$ transitions via virtual or real intermediate states.

The eigenvalues of \mathcal{H} are

$$M_1 - \frac{i}{2}\Gamma_1 \text{ and } M_2 - \frac{i}{2}\Gamma_2 \quad (2.3)$$

where

$$M_{1,2} \equiv M \pm \text{Re}\sqrt{(M_{12}^* - i\frac{\Gamma_{12}^*}{2})(M_{12} - i\frac{\Gamma_{12}}{2})}$$

and

$$\Gamma_{1,2} \equiv \Gamma \mp 2\text{Im}\sqrt{(M_{12}^* - i\frac{\Gamma_{12}^*}{2})(M_{12} - i\frac{\Gamma_{12}}{2})}.$$

The eigenstates of \mathcal{H} are

$$|B_1\rangle = p|B^0\rangle + q|\bar{B}^0\rangle \text{ and } |B_2\rangle = p|B^0\rangle - q|\bar{B}^0\rangle$$

where

$$\frac{q}{p} = \sqrt{\frac{M_{12}^* - i\frac{\Gamma_{12}^*}{2}}{M_{12} - i\frac{\Gamma_{12}}{2}}}$$

and $p^2 + q^2 = 1$. From quark theory, the P (parity) operator transforms the pseudoscalar particle B^0 from a $|B^0\rangle$ state to a $-|B^0\rangle$ state and vice versa while the C (charge conjugation) operator transforms the $|B^0\rangle$ state to a $|\bar{B}^0\rangle$ state and vice versa. Hence, CP eigenstates can be built such that $CP|B_1\rangle = -|B_1\rangle$ and $CP|B_2\rangle = |B_2\rangle$. These CP eigenstates are

$$\begin{aligned} |B_1(t)\rangle &= \frac{1}{\sqrt{2}}[|B^0(t)\rangle + |\bar{B}^0(t)\rangle] \\ |B_2(t)\rangle &= \frac{1}{\sqrt{2}}[|B^0(t)\rangle - |\bar{B}^0(t)\rangle]. \end{aligned} \quad (2.4)$$

implying $|q/p| = 1$.

From equation (2.1) and from the eigenvalues and eigenstates in equations (2.3) and (2.4), the states $|B_1(t)\rangle$ and $|B_2(t)\rangle$ satisfy

$$i\frac{d}{dt}|B_i(t)\rangle = (M_i - i\frac{\Gamma_i}{2})|B_i(t)\rangle \quad (2.5)$$

where the subscript $i = 1$ and 2 . The solution to this equation is

$$|B_i(t)\rangle = Ae^{-iM_i t} e^{-\Gamma_i \frac{t}{2}} \quad (2.6)$$

where A^1 is a constant. But from equation (2.4)

$$|B^0(t)\rangle = \frac{1}{\sqrt{2}}[|B_1(t)\rangle + |B_2(t)\rangle]$$

and

$$|\bar{B}^0(t)\rangle = \frac{1}{\sqrt{2}}[|B_1(t)\rangle - |B_2(t)\rangle].$$

Hence, if a pure B^0 state exists at $t = 0$ then, in equation (2.6), $A = \frac{1}{\sqrt{2}}$ and

$$|B^0(t)\rangle = \frac{1}{2}[e^{-iM_1 t} e^{-\Gamma_1 \frac{t}{2}} + e^{-iM_2 t} e^{-\Gamma_2 \frac{t}{2}}]$$

$$|\bar{B}^0(t)\rangle = \frac{1}{2}[e^{-iM_1 t} e^{-\Gamma_1 \frac{t}{2}} - e^{-iM_2 t} e^{-\Gamma_2 \frac{t}{2}}].$$

The intensity distribution of the B^0 and \bar{B}^0 are

$$I(B^0(t)) = \langle B^0 | B^0 \rangle = \frac{1}{4}(e^{-\Gamma_1 t} + e^{-\Gamma_2 t} + 2e^{-\bar{\Gamma} t} \cos(\Delta M t)) \quad (2.7)$$

$$I(\bar{B}^0(t)) = \langle \bar{B}^0 | \bar{B}^0 \rangle = \frac{1}{4}(e^{-\Gamma_1 t} + e^{-\Gamma_2 t} - 2e^{-\bar{\Gamma} t} \cos(\Delta M t)) \quad (2.8)$$

where $\Delta M = M_2 - M_1$ and $\bar{\Gamma} = \frac{\Gamma_1 + \Gamma_2}{2}$. These equations are the intensity distributions for observing a B^0 state (in the case of $I(B^0(t))$) or a \bar{B}^0 (for the case of $I(\bar{B}^0(t))$) if a pure B^0 state is assumed at $t = 0$. Integrating $I(B^0(t))$ and $I(\bar{B}^0(t))$ over all time results in the total probability of observing a B^0 or a \bar{B}^0 state if a pure B^0 state at $t = 0$ is assumed

$$P(B^0) = \frac{1}{4} \left[\frac{1}{\Gamma_1} + \frac{1}{\Gamma_2} + \frac{2\bar{\Gamma}}{\bar{\Gamma}^2 + (\Delta M)^2} \right] \quad (2.9)$$

¹ A has units of $[\text{energy}]^{\frac{1}{2}}$.

$$P(\overline{B}^0) = \frac{1}{4} \left[\frac{1}{\Gamma_1} + \frac{1}{\Gamma_2} - \frac{2\overline{\Gamma}}{\Gamma^2 + (\Delta M)^2} \right]. \quad (2.10)$$

The mixing probability, χ , is given by [17]

$$\chi = \frac{P(\overline{B}^0)}{P(B^0) + P(\overline{B}^0)} = \frac{(\frac{\Delta M}{\Gamma})^2 + (\frac{\Delta \Gamma}{2\overline{\Gamma}})^2}{2[(\frac{\Delta M}{\Gamma})^2 + 1]} \quad (2.11)$$

where $\Delta \Gamma = \Gamma_2 - \Gamma_1$ and χ varies from 0 to 0.5 since $0 \leq (\frac{\Delta \Gamma}{2\overline{\Gamma}})^2 \leq 1$ and $0 \leq (\frac{\Delta M}{\Gamma})^2 \leq \infty$.

If the approximation $\Gamma_1 \approx \Gamma_2 = \Gamma$ is made which is probably valid for B-decays which have large available phase space and using $\Gamma = \frac{1}{\tau}$, then the time evolution of a B^0 or a \overline{B}^0 state becomes

$$I(B^0(t)) = e^{-\Gamma t} \cos^2 \left(\frac{\Delta M t}{2} \right) = e^{-\frac{t}{\tau}} \cos^2 \left(\frac{1}{2} \frac{\Delta M}{\Gamma} \frac{t}{\tau} \right) \quad (2.12)$$

$$I(\overline{B}^0(t)) = e^{-\Gamma t} \sin^2 \left(\frac{\Delta M t}{2} \right) = e^{-\frac{t}{\tau}} \sin^2 \left(\frac{1}{2} \frac{\Delta M}{\Gamma} \frac{t}{\tau} \right) \quad (2.13)$$

with the probabilities

$$P(B^0) = \frac{1}{2} \left[\frac{2\Gamma^2 + (\Delta M)^2}{\Gamma(\Gamma^2 + (\Delta M)^2)} \right] \quad (2.14)$$

$$P(\overline{B}^0) = \frac{1}{2} \left[\frac{(\Delta M)^2}{\Gamma(\Gamma^2 + (\Delta M)^2)} \right] \quad (2.15)$$

with

$$\chi = \frac{(\frac{\Delta M}{\Gamma})^2}{2[(\frac{\Delta M}{\Gamma})^2 + 1]}. \quad (2.16)$$

Figure 2.1 shows equation (2.12) for two values of $\omega = \frac{1}{2}(\frac{\Delta M}{\Gamma})$ assuming $\tau = 1.37$ ps. The normalized probability distributions ($\frac{dP}{dt}$) of observing a B^0 or a \overline{B}^0 as a function of time are given by $\frac{I(B^0(t))}{P(B^0)}$ and $\frac{I(\overline{B}^0(t))}{P(\overline{B}^0)}$ respectively.

The ARGUS [15] and CLEO [18] collaborations have observed $B_d^0 - \overline{B}_d^0$ oscillations and measured $r = \frac{(\Delta M/\Gamma)^2}{(\Delta M/\Gamma)^2 + 2} = 0.21 \pm 0.08$ and $0.19 \pm 0.06 \pm 0.06$ respectively.

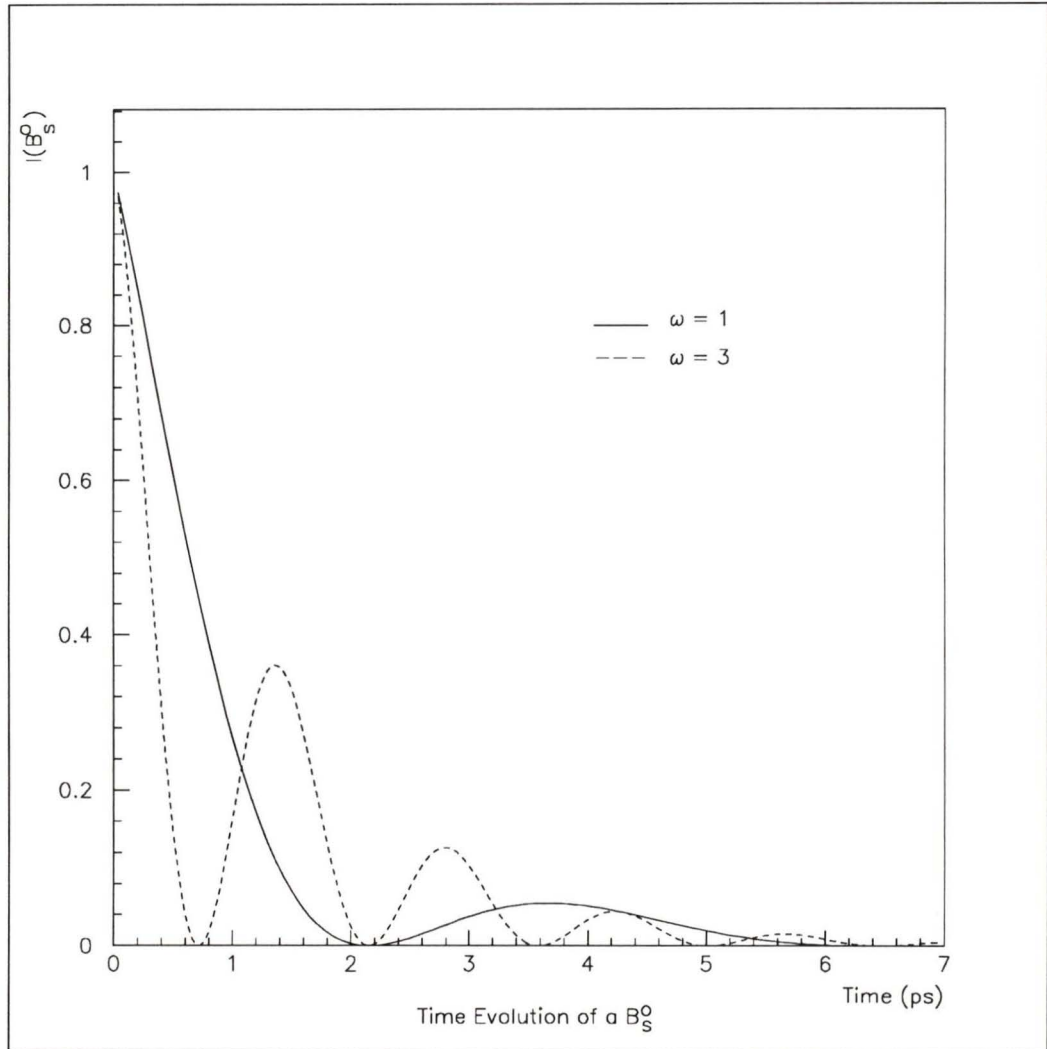


Figure 2.1: The time evolution of a B_s^0 (equation (2.12)) for $\omega = \frac{1}{2}(\frac{\Delta M}{\Gamma}) = 1$ and 3. A lifetime of 1.37 ps is assumed.

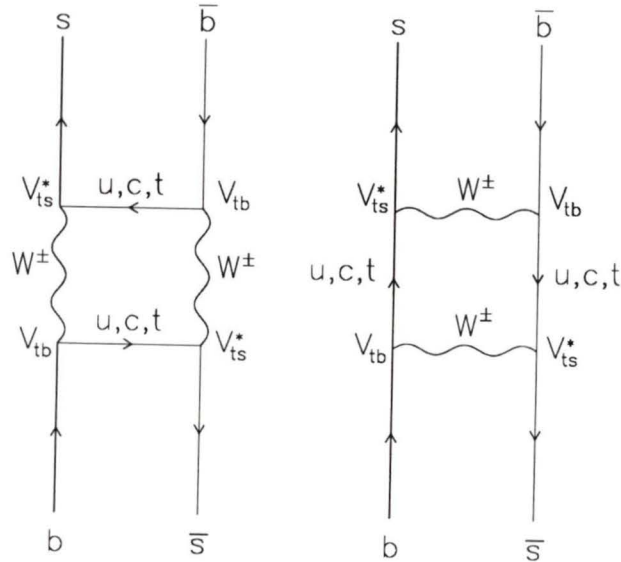


Figure 2.2: Box diagrams for $B_s^0 - \bar{B}_s^0$ flavor oscillation including the dominant C-K-M vertex elements. In the left box diagram, a W^+ moves counter-clockwise and a W^- moves clockwise and vice versa for the right box diagram.

These results give an average value [19] for $\left(\frac{\Delta M}{\Gamma}\right)_{B_d^0}$ of

$$\left(\frac{\Delta M}{\Gamma}\right)_{B_d^0} = 0.71 \pm 0.13. \quad (2.17)$$

Of interest to this thesis is the mixing of $B_s^0 - \bar{B}_s^0$ mesons which is induced by second order weak interactions shown in the diagrams in figure 2.2. These box diagrams can be evaluated to give the value for $(\Delta M)_{B_s^0}$. All six diagrams must be taken into account when evaluating this process. However, the box diagrams with the virtual t quark dominate the expression since the coupling of the b quark and the t quark to the W^+ is given by the V_{tb} element in the C-K-M matrix (see equation 1.6) which is along the diagonal and hence nearly equal to one. Any other b quark C-K-M element is off the diagonal and hence smaller. The following expression results

for $\left(\frac{\Delta M}{\Gamma}\right)_{B_s^o}$ [17]

$$\left(\frac{\Delta M}{\Gamma}\right)_{B_s^o} = \frac{G_F^2 M_t^2}{6\pi} \tau_{B_s^o} B_{B_s^o} f_{B_s^o}^2 M_{B_s^o} [|V_{tb} V_{ts}^*|^2 \frac{A(\xi)}{\xi} \eta_{QCD} + Q] \quad (2.18)$$

where

- G_F , the Fermi coupling constant, is $1.16639 \times 10^{-5} \text{ GeV}^{-2}$,
- M_t , the mass of the t quark, is greater than $91 \text{ GeV}/c^2$ [20] (from experiment),
- $\tau_{B_s^o}$ is the lifetime of the B_s^o as given in table 1.1,
- $f_{B_s^o}$ is the B_s^o decay constant which characterizes the overlap of the \bar{b} and s quarks in the B_s^o , and
- $B_{B_s^o}$, the bag factor, is a QCD correction which encompasses deviations from assumptions made about quark pair production when evaluating the diagram. $f_{B_s^o}$ and $B_{B_s^o}$ are the main source of uncertainty in this problem. A current best estimate gives $B_{B_s^o} f_{B_s^o}^2 \approx (140 \text{ MeV})^2$ [17].
- V_{tb} and V_{ts}^* are elements in the C-K-M matrix (see equation 1.6),
- $A\left(\left(\frac{M_t^2}{M_W^2}\right)^2\right)$, a kinematic correction, is a slow function of the t quark mass. For $85 < M_t < 200 \text{ GeV}/c^2$, the function is approximately equal to 0.65 [17].
- η_{QCD} contains the lowest order QCD corrections and is about 0.83 for the top mass range of $40 < M_t < 200 \text{ GeV}/c^2$ [17].
- Q represents the C-K-M elements for u quark and c quark exchange in figure 2.2.

The quantity often quoted in the literature is $x_s = \left(\frac{\Delta M}{\Gamma}\right)_{B_s^o}$ and from equation (2.12) it is clear that $\frac{1}{2\pi} \left(\frac{\Delta M}{\Gamma}\right)_{B_s^o}$ gives the number of oscillations per lifetime.

Equation (2.18) also holds for B_d^o mixing with the C-K-M matrix elements changed appropriately for box diagrams involving B_d^o ($\bar{b}d$) mixing. This can be used to provide a rough estimate of $(\frac{\Delta M}{\Gamma})_{B_s^o}$ since many factors cancel approximately

$$\left(\frac{\Delta M}{\Gamma}\right)_{B_s^o} \approx \left(\frac{\Delta M}{\Gamma}\right)_{B_d^o} \left| \frac{V_{ts}}{V_{td}} \right|^2 (1 + SU(3)_{breaking}). \quad (2.19)$$

The term $SU(3)_{breaking}$ arises from the fact that the bag factor, B , and the decay constant, f , are not necessarily the same for B_s^o and B_d^o (it is a small correction on the order of 0.0 ± 0.2 [17]). From the present knowledge of the C-K-M matrix given in equation (1.6), $|V_{td}| = 0.003 - 0.019$ and $|V_{ts}| = 0.029 - 0.058$. The measured value from the CLEO and the ARGUS collaborations for $(\frac{\Delta M}{\Gamma})_{B_d^o}$ is given in equation (2.17). Then, according to the Standard Model,

$$\left(\frac{\Delta M}{\Gamma}\right)_{B_s^o} \sim 2 - 265 \quad \text{or } \chi \sim 0.4 - 0.5. \quad (2.20)$$

However, within the patterns of decay between the generations of quarks and leptons, it appears that $|V_{ts}|/|V_{td}| \sim 1/\lambda$ where $\lambda = \sin \theta_c = 0.22$ (the sine of the Cabibbo angle). Hence, a sensible estimate of $(\frac{\Delta M}{\Gamma})_{B_s^o}$ is given by $(\frac{\Delta M}{\Gamma})_{B_s^o} \sim 15$.

The ability for a detector to measure $(\frac{\Delta M}{\Gamma})_{B_s^o}$ will depend on how many samples of B_s^o oscillation can be collected per period. A signal must be sampled at least twice per period in order to measure its frequency of oscillation. A resolution of $\Delta_t = 0.1$ ps for the reconstructed time of flight is equivalent to sampling with that period. Hence, for a B_s^o oscillation with a frequency of $\frac{1}{2} \frac{\Delta M}{\Gamma} \frac{1}{\tau}$, then the maximum frequency that the detector can measure is $(\frac{\omega}{\tau})_{max} = \frac{\pi}{2\Delta_t} \approx 16$ (or $(\frac{\Delta M}{\Gamma})_{max} \approx 43$).

2.2 B Meson Tagging

For an e^+e^- collider operating at the Z^o resonance, the decay $e^+e^- \rightarrow Z^o \rightarrow B_s^o X$ (where X is any particle) will result in a B_s^o meson with a momentum of

approximately $p_B = 30 \text{ GeV}/c$ which travels about 2.2 mm before decaying into a jet of hadrons. These decay products will be emitted in a narrow cone around the direction of the B_s^0 . Since the maximum transverse momentum of a decay product of the B_s^0 is approximately $M_B/2$ or 2.5 GeV/c (where M_B is the mass of the B_s^0), the maximum angle between the jet axis and the track of a decay product is $\approx \frac{M_B}{p_B} \approx 10^\circ$.

Two important requirements must be met when attempting to measure flavor oscillations of B_s^0 mesons: 1) the particle-antiparticle nature of the B_s^0 meson at the B meson production and decay vertices must be determined and 2) B_s^0 mesons must be identified unambiguously. The following sections describe two methods of determining these factors.

2.2.1 Dilepton Tagging Method

The semileptonic decays of the B_s^0 into electrons and muons yield one method of determining the nature of B_s^0 and \bar{B}_s^0 mesons at the B meson production and decay vertices [17]. The sign of the lepton provides the particle-antiparticle nature of the parent B_s^0 at its decay vertex while the sign of the lepton from the other B meson formed at the same time as the B_s^0 provides the particle-antiparticle nature of the B_s^0 at its production vertex (see figure 2.3). This method can be used in the following production processes which specifically yield B_s^0 mesons: $e^+e^- \rightarrow B^+\bar{B}_s^0 + X$, $e^+e^- \rightarrow B_d^0\bar{B}_s^0 + X$, and $e^+e^- \rightarrow B_s^0\bar{B}_s^0 + X$ (see figure 2.4). In order to use this method, the sign of the lepton pairs coming from $B^+\bar{B}_s^0$, $B_d^0\bar{B}_s^0$, and $B_s^0\bar{B}_s^0$ must be determined. These meson pairs are created by pulling quark-antiquark pairs from the vacuum and associating them with the $b\bar{b}$ coming from $e^+e^- \rightarrow b\bar{b}$. The probability of quark-antiquark pair production for the various types of quarks is given by the ratios [22] $P(u\bar{u}) : P(d\bar{d}) : P(s\bar{s}) : P(c\bar{c}) \simeq 1 : 1 : \frac{1}{3} : 10^{-11}$ (determined from experiment). These probabilities indicate that the processes $e^+e^- \rightarrow B^+\bar{B}_s^0 +$

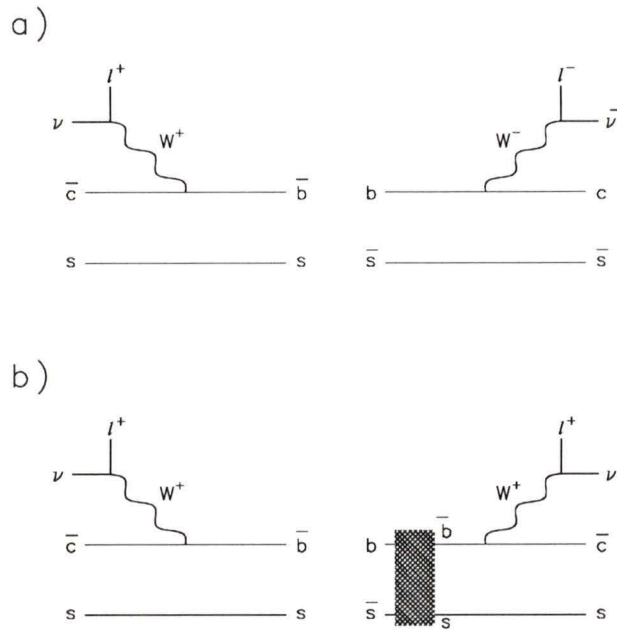


Figure 2.3: Diagrams showing the dilepton tagging of B_s^0 flavor oscillation. B mesons are produced in pairs at the interaction region; hence, in a) no flavor oscillation occurs and so the leptons have opposite signs. In b) flavor oscillation occurs hence the leptons have the same sign.

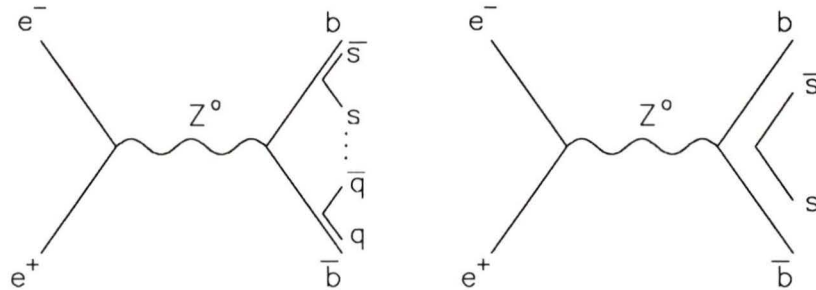


Figure 2.4: Diagrams of the processes which yield B_s^0 mesons. In this diagram, $q = u$ or d .

X and $e^+e^- \rightarrow B_d^0 \bar{B}_s^0$ should occur with equal probability. From figure 2.3, it can be seen that for decays with no oscillation the dileptons will have unlike-sign electrical charges. However, if flavor oscillation occurs, then the dileptons will have like-sign electrical charges. Theory and experiment provide an estimate for the branching ratio of $b\bar{b}$ from the Z^0 . Using this value and the probability for quark-antiquark production, the branching ratios of the processes given in figure 2.4 can be estimated. Using these branching ratios given in table 2.1 from reference [17], the number of dilepton events for each desired reaction can be calculated. Since few B_s^0 mesons have been identified, these branching ratios are theoretical estimates and are likely to be accurate to 10 to 20 percent.

Decays	Branching ratios
$Z^0 \rightarrow B^+ \bar{B}_s^0 + X$	0.04
$Z^0 \rightarrow B_d^0 \bar{B}_s^0 + X$	0.04
$Z^0 \rightarrow B_s^0 \bar{B}_s^0 + X$	0.01
$Z^0 \rightarrow \bar{X}_b \bar{B}_s^0 + X$	0.01

Table 2.1: Estimated branching ratios of the different processes from reference [17]. \bar{X}_b is an antibaryon which contains a \bar{b} quark.

The number of dilepton events detected in an experiment is given by

$$N_{B_q \bar{B}_s^0} = N_{Z^0} \times Br(Z^0 \rightarrow B_q \bar{B}_s^0) \times Br(B_q \rightarrow l^+ + X) \times Br(\bar{B}_s^0 \rightarrow l^- + X) \times \epsilon_1 \epsilon_2 \quad (2.21)$$

where $q = u, d, \text{ or } s$ and $Br(B_q \rightarrow l^+ + X) = 0.21$ represents the sum of the semileptonic branching ratios for B mesons whose charge has not been identified [23]. N_{Z^0} is the number of Z^0 produced and $\epsilon_1 \epsilon_2$ are the efficiencies for detecting the two leptons (either muons or electrons).

In addition to the dilepton events given by (2.21), the sample will include a contribution from $e^+ e^- \rightarrow \bar{X}_b \bar{B}_s^0 + X$ where \bar{X}_b is an antibaryon ($\bar{b} \bar{q}_1 \bar{q}_2$) and $\bar{q}_1 \bar{q}_2$ are light antiquarks (\bar{u}, \bar{d} or \bar{s}). In order to estimate this contribution, it is assumed that the spectator model can be used describe the decay of the \bar{X}_b (see figure 2.5) and hence the semileptonic branching ratio of the \bar{X}_b has been set to $Br(\bar{X}_b \rightarrow l^+ + X) \approx Br(b \rightarrow l^+ + X) = 0.21$. Table 2.2 gives the number of dilepton events produced. From all four processes, the total number of dileptons is given by $4.5 \times 10^{-3} N_{Z^0} \epsilon_1 \epsilon_2$. LEP can produce at least one million Z^0 in a year (after data quality selections, more than 1.0 million hadronic decays of the Z^0 will be detected at OPAL in the 1992 run). One million Z^0 would imply $4.5 \times 10^3 \epsilon_1 \epsilon_2$ dileptons. The number of dileptons actually observed clearly depends on the efficiencies of the lepton detection.

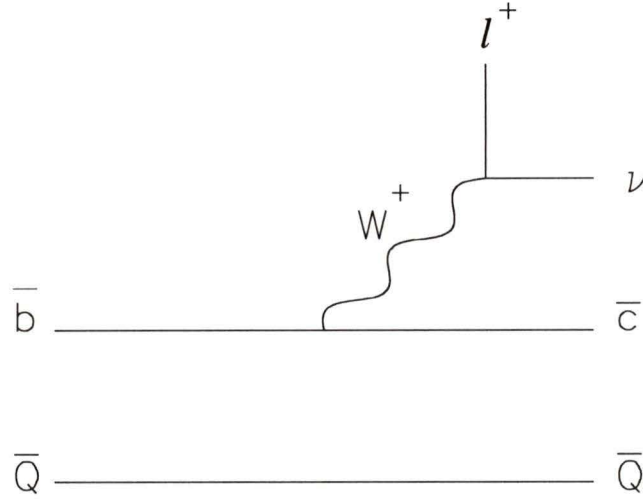


Figure 2.5: The spectator decay of a b antibaryon, \bar{X}_b , where \bar{Q} represents two light quarks.

Meson	N
$B^+ \bar{B}_s^0$	$1.8 \times 10^{-3} N_{Z^0} \epsilon_1 \epsilon_2 \approx 7.6 \times 10^{-4} N_{Z^0}$
$B_d^0 \bar{B}_s^0$	$1.8 \times 10^{-3} N_{Z^0} \epsilon_1 \epsilon_2 \approx 7.6 \times 10^{-4} N_{Z^0}$
$B_s^0 \bar{B}_s^0$	$4.4 \times 10^{-4} N_{Z^0} \epsilon_1 \epsilon_2 \approx 1.8 \times 10^{-4} N_{Z^0}$
$\bar{X}_b \bar{B}_s^0$	$4.4 \times 10^{-4} N_{Z^0} \epsilon_1 \epsilon_2 \approx 1.8 \times 10^{-4} N_{Z^0}$

Table 2.2: The number of dilepton events produced. Muons can be reconstructed with an efficiency of $\epsilon \approx 0.75$ and electrons with an efficiency of $\epsilon \approx 0.55$ [24]. Assuming that electrons and muons are created from B mesons in equal quantities, then $\epsilon_1 \epsilon_2 \approx \frac{1}{2}(0.75)(0.55) + \frac{1}{4}(0.75)(0.75) + \frac{1}{4}(0.55)(0.55) = 0.42$.

Decay	Branching Ratio
$D_s^+ \rightarrow \phi\pi^+$	2.7%
$\overline{K}^{*0} K^+$	2.6%
$\overline{K}^0 K^+$	2.6%
$K^{*+} \overline{K}^0$	3.2%
$\phi \rightarrow K^+ K^-$	50%

Table 2.3: Some branching ratios of D_s^+ and ϕ mesons.

Dilepton signatures can also come from sources other than the direct decays of B hadrons. Leptons may come from cascade decays of b quarks: $b \rightarrow c \rightarrow l$ or from directly produced charmed events ($e^+e^- \rightarrow c\bar{c} \rightarrow l$). The charm background can be reduced by making a selection criterion on the transverse momentum of the lepton with respect to the jet axis (e.g. $p_T > 1.2 \text{ GeV}/c$), since the higher the mass of the parent particle, the higher will be the average p_T of the lepton. Hence, leptons from the B_s^0 decays will have a higher p_T than leptons from D meson decays. Figure 2.6 [25] shows the unnormalized relative abundance of leptons as a function of p_T from the sources mentioned above.

Having obtained a dilepton signature, the identity of the B meson must be established (*i.e.* as a strange B meson). Use can be made of the fact that $Br(B_s^0 \rightarrow l^+ + X) \approx Br(B_s^0 \rightarrow l^+ + D_s^- + X)$ so that when the like and unlike signed leptons are observed, a lepton is tagged on “one side” and a lepton and a D_s on the “other side” [17]. Table 2.3 shows several decays of the D_s^+ [26] along with their branching ratios. If all of the decays in table 2.3 are used then the total effective branching ratio is $11\% \times \epsilon_3$ where ϵ_3 is the average efficiency for reconstructing the D_s in the

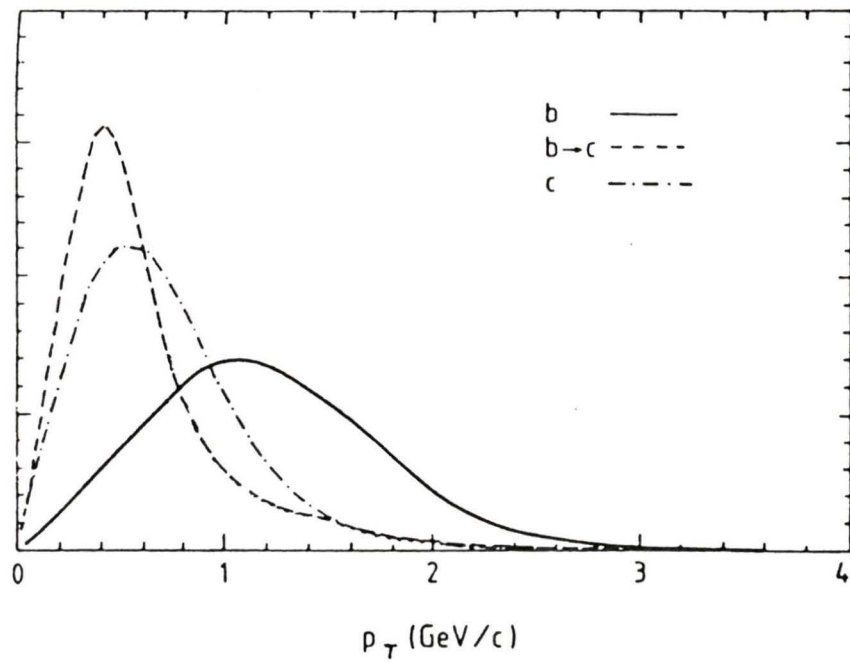


Figure 2.6: Figure showing the relative abundance of leptons as a function of p_T coming from various sources [25]. Note that for $p_T > 1.2$ GeV/c, the majority of leptons come from $b \rightarrow l$.

	$B^+ \overline{B}_s^0$	$B_d^0 \overline{B}_s^0$	$B_s^0 \overline{B}_s^0$	$\overline{X}_b \overline{B}_s^0$
N'	$2.0 \times 10^{-4} N_{Z^0 \epsilon_1 \epsilon_2 \epsilon_3}$	$2.0 \times 10^{-4} N_{Z^0 \epsilon_1 \epsilon_2 \epsilon_3}$	$4.8 \times 10^{-5} N_{Z^0 \epsilon_1 \epsilon_2 \epsilon_3}$	$4.8 \times 10^{-5} N_{Z^0 \epsilon_1 \epsilon_2 \epsilon_3}$

Table 2.4: The number of dileptons produced with a D_s tagged on one side.

decays shown above. The number of dileptons with a D_s tagged on one side becomes

$$N'_{B_q \overline{B}_s^0} = N_{B_q \overline{B}_s^0} \times 0.11 \epsilon_3 \quad (2.22)$$

with the results given in table 2.4. Hence, the total number of dileptons detected along with a D_s reconstruction is then $4.9 \times 10^{-4} N_{Z^0 \epsilon_1 \epsilon_2 \epsilon_3}$. So for one million Z^0 , the number of dileptons events in which a D_s is constructed is about $490 \epsilon_1 \epsilon_2 \epsilon_3$.

It is possible to get a D_s from a source other than B_s^0 . An example is shown in figure 2.7. However, a D_s^+ coming from a B_d^0 will be accompanied by a companion charmed meson (D^- in the figure) and so no lepton is produced with the D_s^+ . Leptons will only be produced from the decay of the D_s^+ or the D^- and so will have a lower momentum than leptons created with the D_s^+ ($b \rightarrow c$ in figure 2.6).

Excellent particle identification is essential. The D_s mainly decays into kaons. Each kaon must be identified and constrained to fit the appropriate place in the D_s decay chain. The product of the three reconstruction efficiencies can therefore be quite small. A rough estimate may be made as follows. The efficiency for reconstructing electrons is about 0.55 and for muons is on the order of 0.75 given realistic requirements [24]. Assuming that electrons and muons are created from B mesons in equal quantities, then $\epsilon_1 \epsilon_2 \approx \frac{1}{2}(0.75)(0.55) + \frac{1}{4}(0.75)(0.75) + \frac{1}{4}(0.55)(0.55) = 0.42$. The selection criterion imposed on the p_T of the leptons ($p_T > 1.2 \text{ GeV}/c$) would decrease this estimate. The D_s decays mainly into kaons. The efficiency for detecting charged kaons with a momentum greater than 2 GeV/c (the range relevant to this

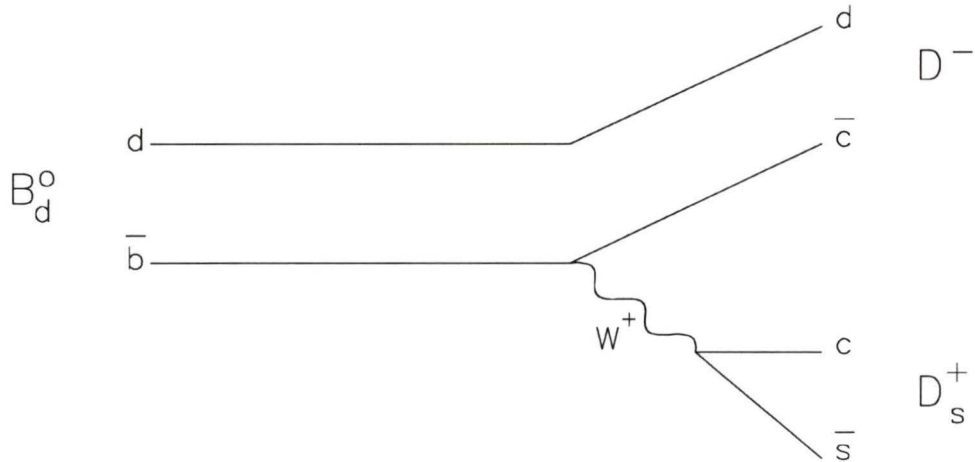


Figure 2.7: Diagram of an example of a D_s^+ produced by the decay of a B_d^0 .

thesis) is about 0.80 [24]. The efficiency for the identification of neutral kaons is expected to be worse. Each decay chain for D_s requires the tagging of two kaons. This reduces the reconstruction efficiency to $\epsilon_3 \approx (0.80)^2 = 0.64$ giving $\epsilon_1\epsilon_2\epsilon_3 \approx 0.27$. Since 490 $\epsilon_1\epsilon_2\epsilon_3$ dileptons are observed from 1 million Z^0 , then about 130 dileptons may be identified per one million Z^0 .

2.2.2 Primary Kaon Method

Another method of tagging $B_s^0 - \bar{B}_s^0$ was proposed by Ali and Barreiro [27]. This method, at the optimistic extreme of their assumptions, uniquely tags a B_s^0 oscillation. Ali and Barreiro proposed to measure B_s^0 oscillations by using charged kaons produced at the primary step of the B_s^0 production and by looking for leptons which are the direct decay products of B_s^0 mesons. They develop a signature for B_s^0 oscillation which is $B_s^0 \rightarrow \bar{B}_s^0 \rightarrow l^- K^+ K^+ X$ (or $\bar{B}_s^0 \rightarrow B_s^0 \rightarrow l^+ K^- K^- X$) where

X is any particle including possibly another kaon. However, this method requires distinguishing between kaons produced at the primary step of the B_s^0 production (the primary or leading kaons) and the kaons produced by the decay products of the B_s^0 . The momentum difference does not distinguish uniquely between these two types of kaons. For this reason, this method is impractical for detectors like OPAL. However, this primary kaon method is included in this thesis for completeness.

In order to create a \bar{B}_s^0 , an $s\bar{s}$ quark must be pulled out of the vacuum. One quark will associate with the b quark to make a \bar{B}_s^0 meson while the other s will often join with a \bar{d} quark to form a neutral leading kaon associated with the primary vertex or with a \bar{u} to form a leading charged kaon. Ali and Barreiro are only interested in leading charged kaons. This reaction would occur as (see figure 2.8a)

$$\begin{aligned}
 b &\rightarrow (b\bar{s}) + (s\bar{u}) + u \\
 &\quad \hookrightarrow K^- + X \\
 &\hookrightarrow \bar{B}_s^0 \rightarrow (D_s^+, D_s^{*+}, \dots) l^- \bar{\nu}_l \\
 &\quad \hookrightarrow K^\pm X
 \end{aligned} \tag{2.23}$$

(i.e. $b \rightarrow l^- K^- K^+ X$ and $b \rightarrow l^- K^- K^- X$) where X is any particle including another kaon. The case for \bar{b} quarks is given by charge conjugate states. The sign of the (negative) leading kaon tags the particle-antiparticle nature of the B_s^0 meson at its production while the sign of the lepton tags the particle-antiparticle nature of the B_s^0 meson at its decay.

A B^- can be created with a leading charged kaon (see figure 2.8b)

$$\begin{aligned}
 b &\rightarrow (b\bar{u}) + (u\bar{s}) + s \\
 &\quad \hookrightarrow K^+ + X \\
 &\hookrightarrow B^- \rightarrow (D^0, D^{*0}, \dots) l^- \bar{\nu}_l \\
 &\quad \hookrightarrow K^- X
 \end{aligned} \tag{2.24}$$

(i.e. $b \rightarrow l^- K^+ K^- X$).

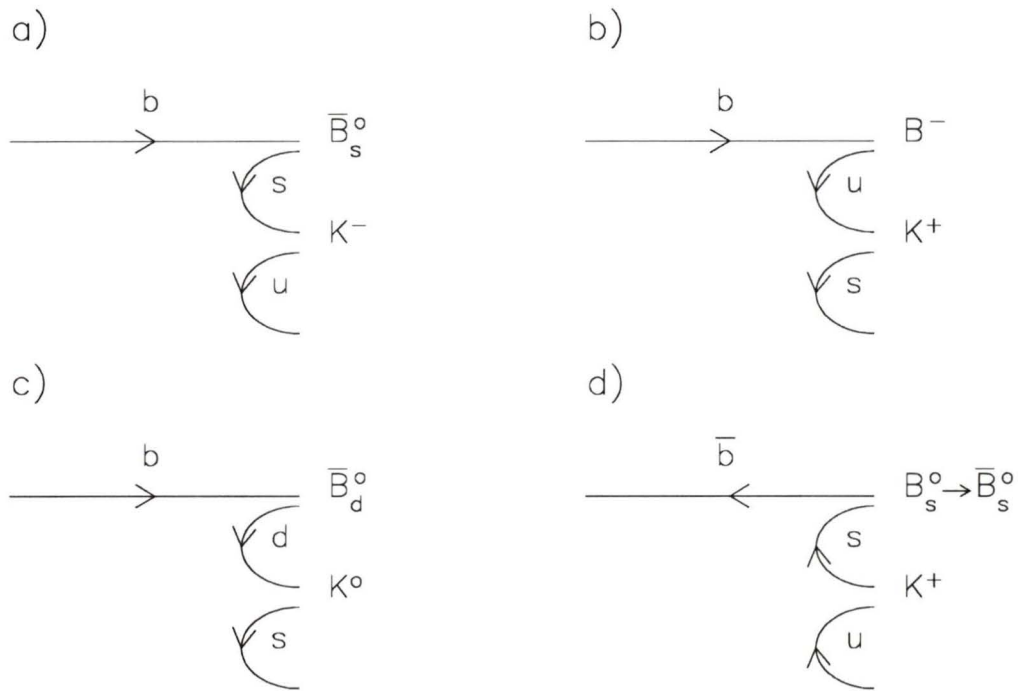


Figure 2.8: Diagrams of the production of leading kaons with (a) the \bar{B}_s^0 , (b) the B^- , (c) the \bar{B}_d^0 , and (d) the oscillation $B_s^0 - \bar{B}_s^0$. Diagram c) cannot have a leading charged kaon.

B meson	Decay mode
\overline{B}_s^0	$b \rightarrow l^- K^- K^- X$ $b \rightarrow l^- K^- K^+ X$
B^-	$b \rightarrow l^- K^+ K^- X$
\overline{B}_d^0	$b \rightarrow l^- K^0 K^- X$
$\overline{B}_d^0 \rightarrow B_d^0$	$\overline{b} \rightarrow l^+ K^0 K^+ X$
$B_s^0 \rightarrow \overline{B}_s^0$	$\overline{b} \rightarrow l^- K^+ K^+ X$ unique $\overline{b} \rightarrow l^- K^+ K^- X$

Table 2.5: Decays of the B meson for the primary kaon method. X is any particle including another kaon.

A leading charged kaon cannot be created in conjunction to a \overline{B}_d^0 (see figure 2.8c)

$$\begin{aligned}
 b &\rightarrow (b\overline{d}) + (d\overline{s}) + s \\
 &\quad \hookrightarrow K^0 + X \\
 &\hookrightarrow \overline{B}_d^0 \rightarrow (D^+, D^{*+}, \dots) l^- \overline{\nu}_l \\
 &\quad \hookrightarrow K^- X
 \end{aligned} \tag{2.25}$$

(i.e. $b \rightarrow l^- K^0 K^- X$). If the B_d^0 oscillates to a \overline{B}_d^0 before its decay, the sign of the lepton will change but the leading kaon will still be neutral.

The flavor oscillation of the B_s^0 is given by (see figure 2.8d)

$$\begin{aligned}
 \overline{b} &\rightarrow (\overline{b}s) + (\overline{s}u) + \overline{u} \\
 &\quad \Updownarrow \hookrightarrow K^+ + X \\
 (b\overline{s}) &\rightarrow \overline{B}_s^0 \rightarrow (D_s^+, D_s^{*+}, \dots) l^- \overline{\nu}_l \\
 &\quad \hookrightarrow K^\pm X
 \end{aligned} \tag{2.26}$$

(i.e. $\overline{b} \rightarrow b \rightarrow l^- K^+ K^+ X$ and $\overline{b} \rightarrow b \rightarrow l^- K^+ K^- X$).

Table 2.5 gives a summary of the decay signatures of the B mesons as discussed in this section. From this table, the signature for $B_s^0 - \overline{B}_s^0$ oscillations ($\overline{b} \rightarrow l^- K^+ K^+ X$) is unique. It must be noted that the signature $l^- K^+ K^+ X$ can also come from the decay of the B^- since the D^+ can decay to a K^+ . However,

this decay is Cabibbo suppressed and hence there is a suppression factor of about $\sin^2 \theta_c = 1/20$.

Ali and Barreiro proposed to make a measurement of the ratio

$$R = \frac{b \rightarrow l^+ K^- K^- X}{b \rightarrow l^- K^- K^- X} \quad (2.27)$$

in order to measure the level of mixing in the B_s^0 system. It is clear from this method that it is essential to distinguish clearly between the leading kaons and the kaons produced by the decay products of the B_s^0 . Since this would be very difficult to do at detectors like OPAL, this method is not considered as practical.

2.3 Measuring B Meson Oscillations

How can these oscillations be measured in an experiment? In the previous sections, the two tagging methods (dilepton method and primary kaon method) indicated how one can detect that a B_s^0 meson has changed flavor before decaying. In order to measure the frequency of oscillation of the flavor change, it is necessary to know the time of flight of these B_s^0 mesons. This requires the reconstruction of the primary (B_s^0 production) vertex and the secondary (B_s^0 decay) vertex. The distance between the coordinates of the secondary vertex and the coordinates of primary vertex gives the distance traveled by the B_s^0 meson. This value can be converted to a measurement of the time between the creation and the decay of the B_s^0 meson (the time of flight of the B_s^0 meson). The B_s^0 meson will travel a distance of $L = \gamma\beta c\tau$ where L is the value measured from the experiment and τ , the time of flight, is the desired quantity. The boost factor, $\gamma\beta = \frac{p_B}{M_B}$ which is at most ≈ 8 for B_s^0 mesons produced at the Z^0 [17], must be known. However, it is difficult to determine the momentum of the B_s^0 meson, p_B , from the decay particles of the B_s^0 meson since some of the decay particles may be neutrinos, or other neutral particles which escape detection

and carry off some of the momentum. The estimated boost factor from the decay products of the B_s^0 meson is given by $\gamma\beta = p_{observed}/M_{observed}$ where $p_{observed}$ is the total momentum of observed decay particles which have invariant mass $M_{observed}$. The error on this estimate will decrease as the boost factor increases [17]. For a low boost of 0 to 2, the fractional error will be about 13 percent while at a high boost of 7 to 8, the fractional error will be about 8 to 9 percent. An error in the boost implies an error in the decay length. By using this boost factor, the time of flight of the B_s^0 meson can be calculated from the equation $L = \gamma\beta c\tau$.

A time of flight is calculated for each B_s^0 meson. Then, in principle either of the tagging schemes described in 2.2, can be used to determine if this B_s^0 meson oscillated before decaying. If no oscillation occurred, then the time of flight of this meson is histogrammed. This procedure is then used on all reconstructed B_s^0 mesons. The histogram is then the intensity distribution for a B_s^0 not to change flavor before decaying as given in (2.12). No flavor change before decaying can also include an even number of flavor oscillations. The time of flight of B_s^0 mesons which did oscillate before decaying can also be histogrammed giving the intensity distribution of B_s^0 mesons which oscillate an odd number of times as given in (2.13). However, only the former type of time of flight distribution will be considered in the Monte Carlo modeling performed in this thesis.

For the time of flight of B_s^0 mesons which do not change flavor before decaying (as given in (2.12)), there will be an admixture of flight times which follow the intensity distribution (2.13) (B mesons which change flavor before decaying) due to mistagging. When a lepton is tagged on the B_s^0 side of the interaction, then it is possible that if the \bar{B} meson on the other side of the interaction is a \bar{B}_s^0 or a \bar{B}_d^0 , it can change flavor before decaying and thereby flip the sign of the decay lepton. The

fraction of mistagging is given by

$$a = \frac{Br(Z^0 \rightarrow B_s^0 \bar{B}_d^0) \chi_d + Br(Z^0 \rightarrow B_s^0 \bar{B}_s^0) \chi_s}{Br(Z^0 \rightarrow B_s^0 \bar{B}_d^0) + Br(Z^0 \rightarrow B_s^0 \bar{B}_s^0) + Br(Z^0 \rightarrow B_s^0 B^-) + Br(Z^0 \rightarrow B_s^0 \bar{X}_b)} \quad (2.28)$$

where $\chi_d = 0.17$ is the $B_d^0 - \bar{B}_d^0$ mixing probability, $\chi_s = 0.4 - 0.5$ is the $B_s^0 - \bar{B}_s^0$ mixing probability, and the branching ratios can be found in table 2.1. From these values, $a \approx 11$ to 12 percent. Since these branching ratios have not yet been experimentally verified, a range of 10 percent to 20 percent mistagging will be explored in the B_s^0 meson simulation programs described in chapter 5.

Also, the time of flight distribution is subject to effects such as smearing due to the finite time resolution of the detector (experimental errors in the decay length and boost determination). A contribution to the time smearing comes from the fact the mean lifetime of the D_s meson ≈ 0.5 ps and hence there will be experimental problems associated with distinguishing the B_s^0 and the D_s decay vertices. In addition, there will be “flat background noise”.

The frequency of oscillation is determined from the histogram contents which give a measurement of $\frac{\Delta M}{\Gamma}$. It must be noted that the detector can only resolve the time of flight to about $\frac{1}{10}$ the lifetime of the B_s^0 meson [28]; hence the bin size of the histogram will have to be about 0.1 to 0.2 ps. Since from equation (2.12) the time of flight histogram follows a $\cos^2 \frac{\Delta M}{2} t = \cos^2 \frac{\Delta M}{2\Gamma} \frac{t}{\tau}$ (and $\frac{\Delta M}{2\Gamma} = \omega$) the upper bound on the measurement of the frequency is given by $(\frac{\omega}{\tau})_{max} = \frac{\pi}{2\Delta_t}$ where Δ_t is the time of flight resolution of the detector as described in section 2.1. Hence, a time of flight resolution of $\Delta_t = 0.1$ ps implies $\frac{\Delta M}{\Gamma} \leq 43$ can be measured but values of $\frac{\Delta M}{\Gamma} \geq 43$ cannot be measured by a detector with a time of flight resolution of $\Delta_t = 0.1$ ps.

Chapter 3

The OPAL Detector

3.1 An Overview of the OPAL Detector

OPAL is an omni-purpose detector at LEP. The simulation of the B_s^0 oscillations described in this thesis is based on the properties of the OPAL detector. Part of this thesis describes tests made by the author on wafers from the OPAL silicon microvertex detector. A brief description of this detector is given below. Reference [29] gives a more complete description.

A diagram of OPAL is shown in figure 3.1 [29]. OPAL has a solenoidal magnetic field provided by a warm coil and an iron return yoke. There are four central tracking detectors: two concentric cylinders of silicon strip microvertex detectors around the beam pipe, a 1 m long vertex drift chamber, a 4 m long jet chamber with an inner diameter of 0.5 m and an outer diameter of 3.7 m, and the z-chambers which surround the jet chamber. All are used to track charged particles and measure their momentum and direction. The central tracking system operates at a pressure of 4 bars and tracks are linked by extrapolation to hits in the silicon microvertex detector. The spatial resolution of the OPAL silicon microvertex detector will be discussed in chapter 4.

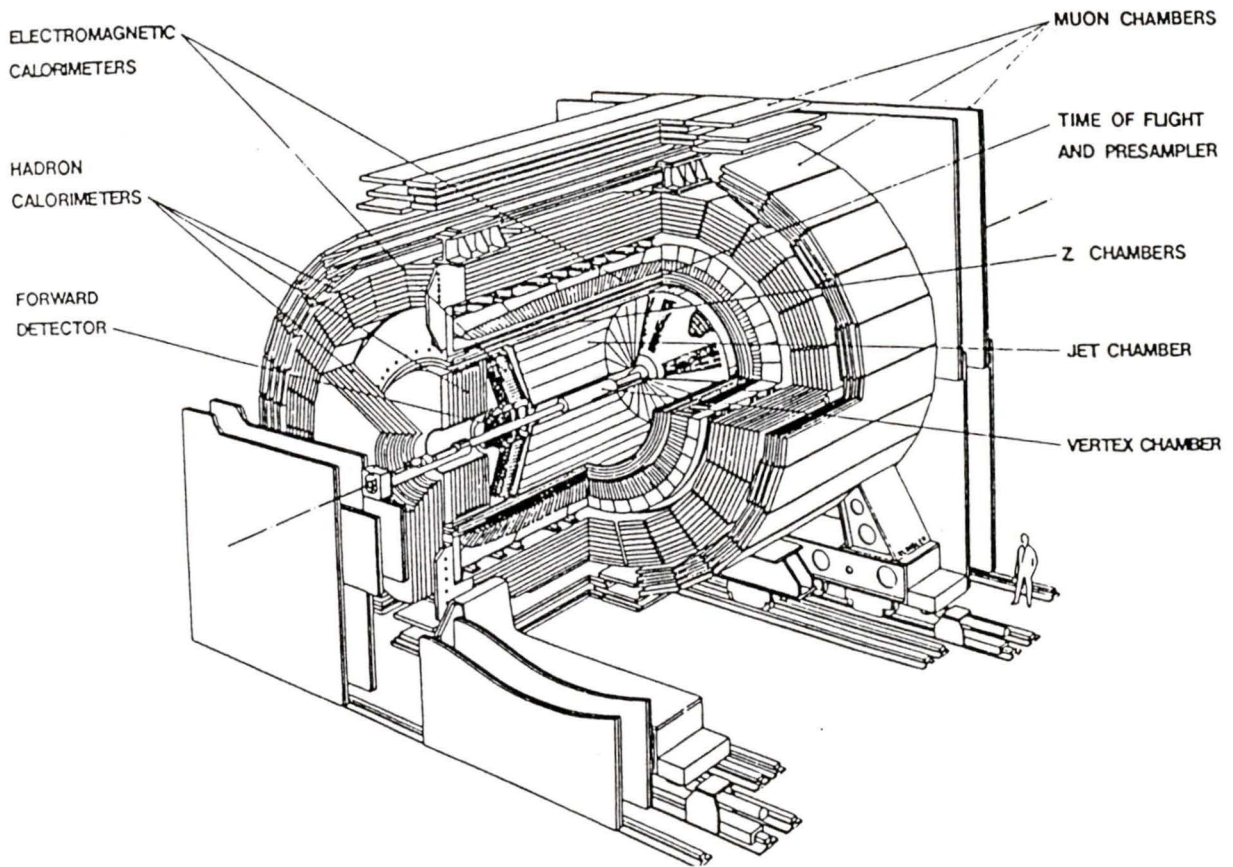


Figure 3.1: Diagram of the OPAL detector at the CERN laboratory in Switzerland from reference [29].

Particle identification is achieved by measurements of the average energy loss, $\frac{dE}{dx}$, in the gas of the jet chamber in conjunction with the momentum of the particle. The resolution of the average energy loss in the OPAL jet chamber is $\frac{\sigma_{dE/dx}}{dE/dx} \approx 0.038$ [29] while the momentum resolution of charged tracks in the plane perpendicular to the beam axis is $\frac{\sigma_{p_t}}{p_t} = ((0.02)^2 + (0.0015p_t)^2)^{\frac{1}{2}}$ [24]. The electromagnetic calorimeter consisting of approximately 10000 lead glass blocks is mounted between the coil and the return yoke. It measures the position and energy of photons, electrons, and positrons with an energy resolution of about $\frac{\sigma_E}{E} = 0.05/\sqrt{E}$ where E is in GeV. The iron slabs of the yoke of the magnet are instrumental to provide a hadron calorimeter. Outside the hadron calorimeter is a detector which measures the position and the direction of muons.

3.1.1 The Principles of the Silicon Microvertex Detector

Semiconductor detectors are made up of elements such as silicon or germanium [30]. In a silicon crystal, the energy levels of the silicon atom coalesce into bands which are so close together that they may be considered as continuous. The valence electrons of the silicon atoms occupy the valence band while the unoccupied levels make up the conduction band. The band gap, E_o , is the energy needed for an electron at the top of the valence band to go to the bottom of the conduction band. For a silicon crystal, $E_o = 1.12$ eV. The electron is free to travel within the conduction band and so E_o may be considered as the minimum energy necessary to “ionize” a silicon crystal.

Using a process known as doping, a small fraction of the silicon atoms are replaced with atoms that have either 3 or 5 valence electrons. This process introduces an energy level between the valence and conduction band which increases the concentration of free charge carriers.

Incident charged particles passing through the silicon will lose some of their energy which will lead to the production of electron-hole pairs. Since some energy is lost in exciting the lattice, approximately 3.6 eV is necessary to generate an electron-hole pair. Gases require for example about 30 eV to produce ion pairs. In 300 μm of silicon, a minimum ionizing particle will produce about 28000 pairs.

Silicon wafers are used to make up the silicon microvertex detector which is designed to improve the spatial definition of vertex detection. The OPAL silicon strip microvertex detector consists of two concentric barrels of detectors which are supported around the LEP beam pipe. The inner barrel contains 11 ladders each with three silicon wafers, and the external barrel has 14 similar ladders. Figure 3.2 shows the positioning of the ladders with respect to the beam pipe. Each silicon wafer is 33 mm wide, 60 mm long, and 300 μm thick. The detector provides only $r - \phi$ coordinates.

Diode strips (p^+) are implanted into the base of n-type silicon with a 25 μm pitch (see figure 3.3). In the current OPAL detector, these strips run parallel to the e^+e^- beam direction. The readout preamplifiers are connected directly to the aluminum strips which are capacitively coupled to alternate diode strips giving a readout pitch of 50 μm . There are several reasons why only every other strip is aluminized. The main reason is the high density of strips to be read out and the difficulties associated with this. If every strip were to be aluminized, then 40 channels per mm would require read out. However not much would be gained in terms of spatial resolution since the optimum strip pitch depends on the size of the electron cloud created by ionizing the radiation. The aluminum readout strips are capacitively coupled through thin SiO_2 insulators. A reverse bias is produced by applying a positive voltage to the opposite face of the detector. The individual biasing of strips is achieved via a Field Effect Transistors constructed on the Field OXide of

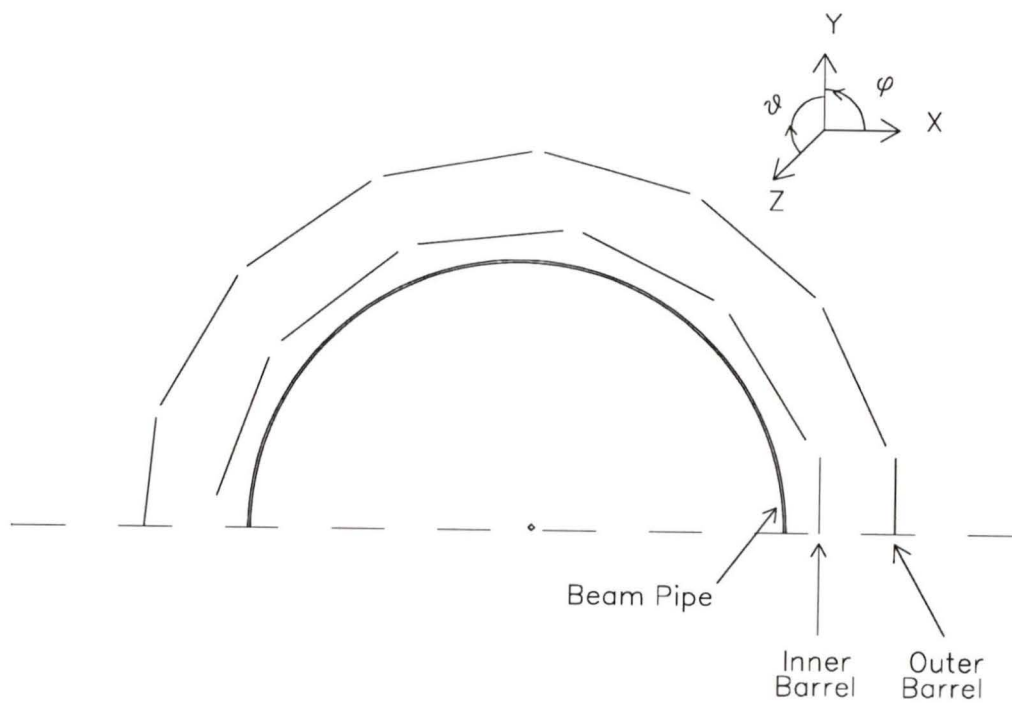


Figure 3.2: Diagram of the orientation of the ladders on the barrels of the OPAL silicon microvertex detector. The distance from the center of the beam pipe to the 1.1 mm Be beam pipe is 5.35 cm. The distance from the center of the beam pipe to the inner barrel and to the outer barrel are 6.08 cm and 7.52 cm respectively.

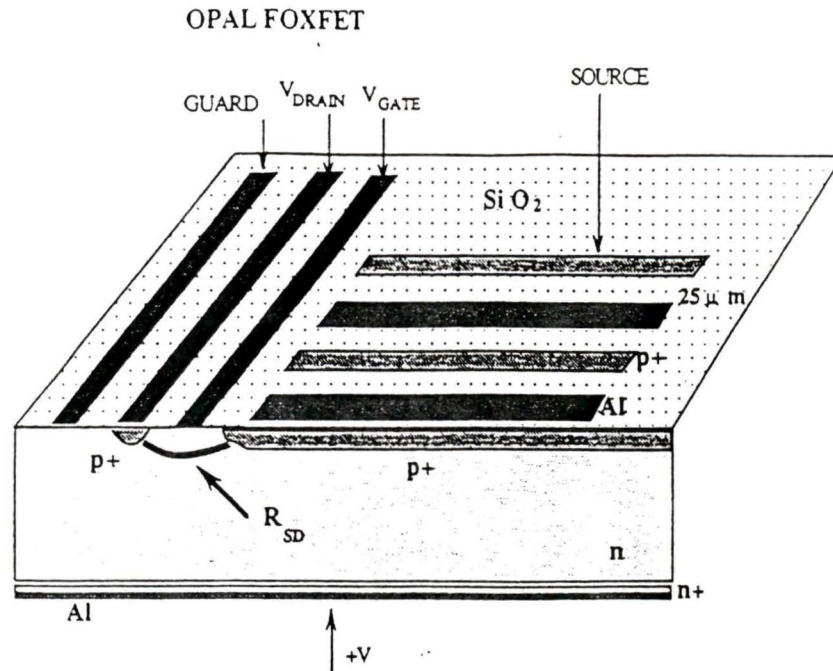


Figure 3.3: A diagram of a silicon wafer taken from reference [31].

the sensitive side of the detector (FOXFET). The electron-hole pairs created by the ionizing radiation in the detector are influenced by an external electric field such that the electrons drift to the opposite face of the detector which is aluminum coated and the holes collect on the strips all within about 10 ns.

MX3 or MX5 multiplexer and amplifier chips are bonded to the ends of these aluminum strips and used for the read out of pulse heights due to the accumulation of charge on each strip. Each chip is approximately $6.4 \text{ mm} \times 6.4 \text{ mm}$ and controls 128 read out channels. Five chips make up one 640 channel detector.

The spatial distribution of the drifting charge is assumed to be a Gaussian distribution with $\sigma \approx 12 \mu\text{m}$ for this detector. It is assumed that all of the charge is deposited on the strips within $\pm 3\sigma$ of the track flight path. Since the full width at half maximum of a Gaussian distribution is 2.36σ ($\approx 28\mu\text{m}$ for this detector), then the strip pitch of the microstrip detector is approximately equal to the full width

at half maximum of the Gaussian distribution of the drifting charge. Hence, it is assumed that most of the charge is deposited onto two readout strips. The charge deposited on the non-readout strips is divided between the two nearest readout strips.

A knowledge of the spatial resolution of the silicon microvertex detector is important for the work in the following chapters. However, before finding this spatial resolution, it is essential to understand the concepts of pulse height and detector noise. It would be difficult to obtain a good spatial resolution if the energy resolution or alternatively the signal-to-noise ratio were poor. In order to know more about the energy resolution of the detector, the author analyzed a sample run from the 1990 test beam data. The goal was to fit the energy deposition in silicon for a given data set with a Landau distribution convoluted with a Gaussian distribution. The data (run number 2168 which contained 27106 events at a rate of about 0.5 Hz) was obtained at the PS accelerator at CERN on November 20 to 21, 1990. The data from three single-sided silicon microvertex detectors placed one behind the other with their parallel strips exposed to an incident 5 GeV/c pion beam were analyzed. The two outer detectors were FOXFET detectors equipped with 5 MX3 chips each, while the inner FOXFET detector had 5 MX5 chips (a lower noise version of the MX3 chip). Figure 3.4 shows the layout of this experiment. The objectives of this study were:

1. to see if the data on energy loss is in agreement with the theory of Landau and
2. to determine a value for the detector noise and associated electronics noise for each type of detector and to verify that this value is consistent with the expected value.

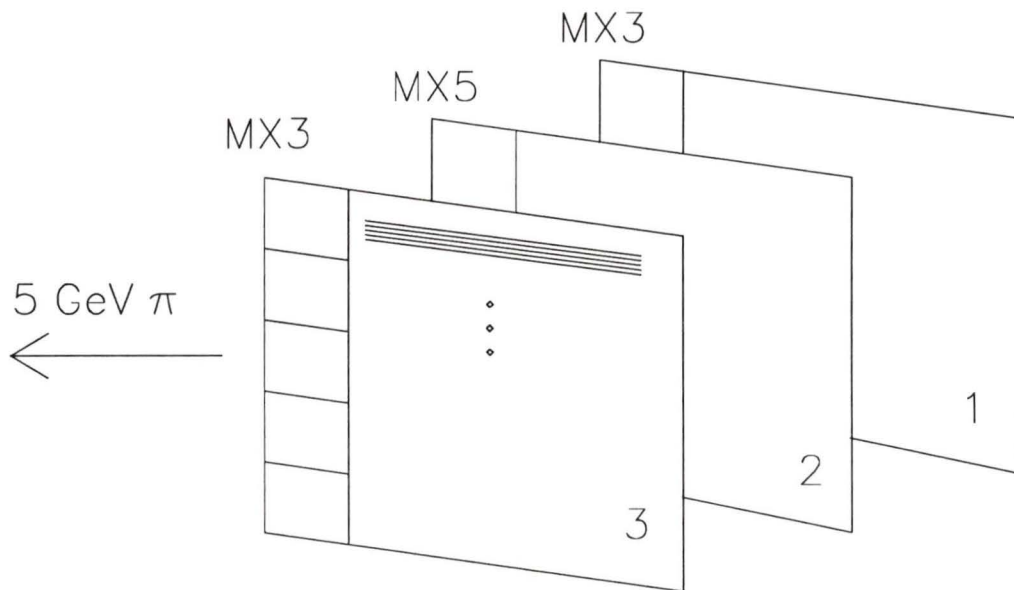


Figure 3.4: The layout of the test beam run which tested the performance of the silicon microvertex detector at the PS accelerator at CERN. The two outer detectors are FOXFET detectors equipped with 5 MX3 chips each while the inner FOXFET detector has 5 MX5 chips. A 5 GeV/c π beam was incident on these detectors. The separation distance between detector 1 and 2 is 2.54 ± 0.01 cm and the distance between detector 2 and 3 is 2.50 ± 0.01 cm.

The data tapes were read with the SITB110 program (from the OPAL SI110 silicon analysis program [32]) which created the histograms of the cluster pulse height for each detector. The LANDPAR2 program was developed by the author to fit these histograms to the convoluted Landau distributions.

3.2 Energy Loss Theory

As an incident charged particle passes through the silicon detector, some of its energy is lost by exciting or effectively ionizing electrons into the conduction band, hence creating electron-hole pairs. Some of its energy is also lost to exciting the lattice and to the creation of high energy recoil electrons called delta rays which can themselves ionize the silicon. The charge drifts under the influence of an electric field onto the detector's readout strips giving a pulse height proportional to the energy deposited in the silicon.

The Landau energy loss theory can be used when describing the energy loss of 5 GeV/c pions in 300 μm of silicon. Appendix A gives a description of the Landau energy loss theory. Figure 3.5 shows a Landau distribution for 5 GeV/c pions in 300 μm of silicon.

The energy loss distributions from the various detectors cannot simply be fitted to Landau distributions because the intrinsic noise of the detector and its electronic noise affect the measurement of the energy loss. The noise can best be described by the smearing of the measurement of the energy loss of an event with a Gaussian distribution. Each event is smeared with a Gaussian distribution. Hence, the function to be used when fitting the energy loss distribution is a Landau distribution convoluted with a Gaussian distribution. Given two functions $f(x)$ and $g(y)$, the

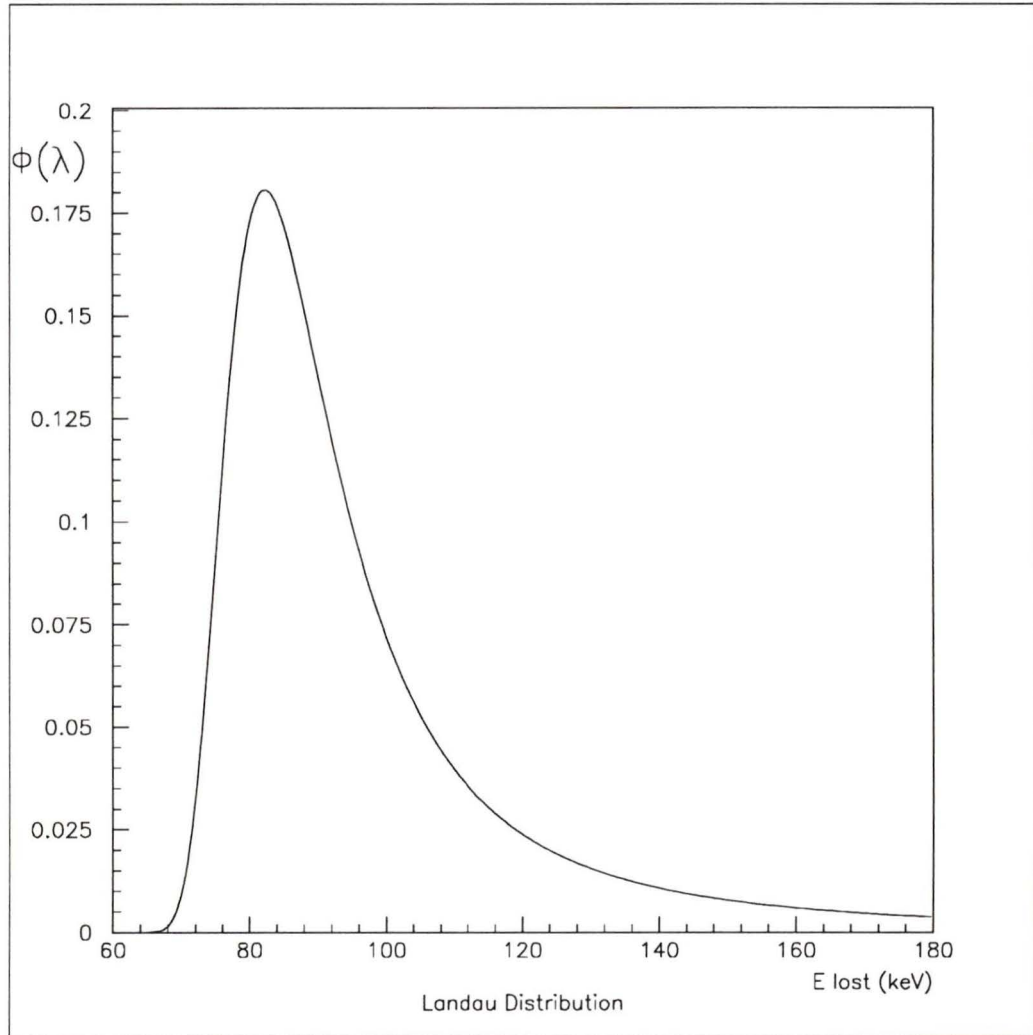


Figure 3.5: Plot of a Landau distribution for 5 GeV/c pions in 300 μm of silicon. $\phi(\lambda)$ is the Landau integral shown in equation (A.7).

convolution integral is

$$[g \otimes f](x) = \int_{-\infty}^{+\infty} f(x-y)g(y)dy. \quad (3.1)$$

This convolution was approximated in the program LANDPAR2 by taking the continuous Landau distribution, $f(x)$, and the Gaussian distribution divided into n equal segments, $g(y_i)$, and thus for a given x

$$[g \otimes f](x) \approx N \sum_{i=-\frac{n}{2}}^{+\frac{n}{2}} f(x-y_i)g(y_i) \quad (3.2)$$

where N is a normalization constant and $n = 100$. From the work as described in chapter 4 on the fitting of pulse height distributions to convoluted Landau distributions, it was estimated that the σ of the Gaussian distribution is about 10 keV.

Due to the assumptions made in the derivation of the Landau distribution, the effect of the electron binding energy for long distance interactions was neglected and so it must be taken into account [33]. This correction comes in the form of a Gaussian with a σ_c given by

$$\sigma_c^2 = \frac{8}{3}\xi[10^{-3}(2.319 + 0.670 \ln \beta)] \text{ MeV}^2 \quad (3.3)$$

and for 5 GeV/c pions

$$\sigma_c^2 = 33.1 \text{ keV}^2. \quad (3.4)$$

Therefore, the σ_T used in the Gaussian part of the convoluted Landau distribution becomes,

$$\sigma_T^2 = \sigma_c^2 + \sigma_{noise}^2 \quad (3.5)$$

where σ_{noise} is the standard deviation of the Gaussian noise distribution from the detector and electronics measured in the absence of a signal.

Chapter 4

Silicon Vertex Detector Analysis and Results

4.1 Energy Loss Analysis and Results

The energy loss analysis of the silicon microvertex detector will proceed as follows:

- A description of the method of selection of event clusters for each detector will be given.
- The distribution of cluster pulse height sums for each detector will be fitted to a Landau distribution convoluted with a Gaussian distribution in order to find the σ_T of the Gaussian and hence the noise of the detector.
- This σ_T from the convolution will be compared to the expected noise for these detectors.

The setup for this experiment is described in chapter 3 and a diagram of the position of the detectors with respect to the pion beam is shown in figure 3.4. The rate of pions incident on the detector typically ranged from 0.5 Hz to 10 Hz. The software which read out events from the detector also stored all events onto tape.

The program SITB110 then analyzed all events into tracks by performing least square fits. In this data, readout chip 1 of detector 1 and readout chip 5 of detector 3 were not functioning.

For each channel or detector readout strip, data were taken with no beam, and a mean (pedestal) and a width (σ) of the pulse height distribution were calculated. For the data collected with beam, only the channels with pulse heights greater than or equal to 3.75σ (where σ is the width of the pedestal pulse height distribution) were considered to be an event. A cluster was defined as a collection of adjacent channels with sufficiently large pulse heights which also satisfied a series of conditions imposed by SITB110 [32]. All potential clusters which survived these conditions were then stored.

The position of a cluster in the detector is found by taking the weighted mean of the channel with the highest pulse height and its highest neighbor [31]

$$y = \frac{S_1 Ch_1 + S_2 Ch_2}{S_1 + S_2} \quad (4.1)$$

where Ch_1 and Ch_2 are the channel numbers and S_1 and S_2 are the pulse heights.

A least squares fit was performed using all of these clusters in order to find the tracks crossing all three detectors. If x_i is the position of the i^{th} detector along the beam line and y_i is the vertical position of the cluster on the i^{th} detector then the χ^2 of the fit was

$$\chi^2 = \sum_i (y_i - a - bx_i)^2 \quad (4.2)$$

where a and b are the parameters of the track. The errors were assumed to be a constant for all clusters and hence ignored in the χ^2 fit. For a given cluster on detector 1, the χ^2 of all of the possible tracks using clusters in the other detectors was calculated. The track with the lowest χ^2 was considered to be the best track. The distribution of the lowest χ^2 for all the tracks is shown in figure 4.1. This

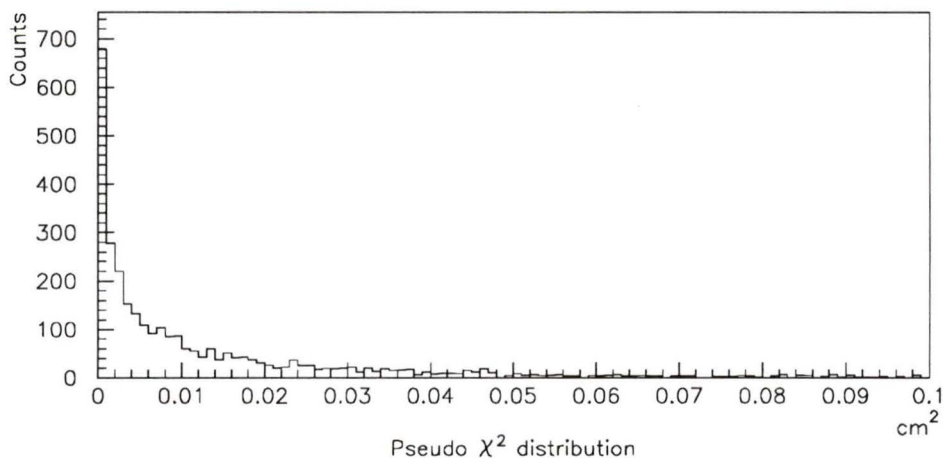


Figure 4.1: *Distribution of the lowest χ^2 of the tracks. This figure is referred to as a pseudo χ^2 because σ_i was ignored in the fit.*

procedure was repeated for all the clusters in detector 1. Only the clusters used in the best tracks were retained.

It is possible that some single channel noise hits which survived the 3.75σ requirement on one of the detectors are included as best tracks. A minimum pulse height requirement was made to discard these noise hits and still minimize the effect on the pulse height distribution of the clusters.

The remaining clusters were stored in cluster pulse height sum histograms (see figure 4.2) and were used as the energy loss distributions to be fitted with the convoluted Landau function. Detector 2 was read out via an MX5 chip which had a larger gain than the MX3 chips used to readout detectors 1 and 3. The gain for each chip in each detector was measured [31] and no significant differences in gains of the chips within a detector was found.

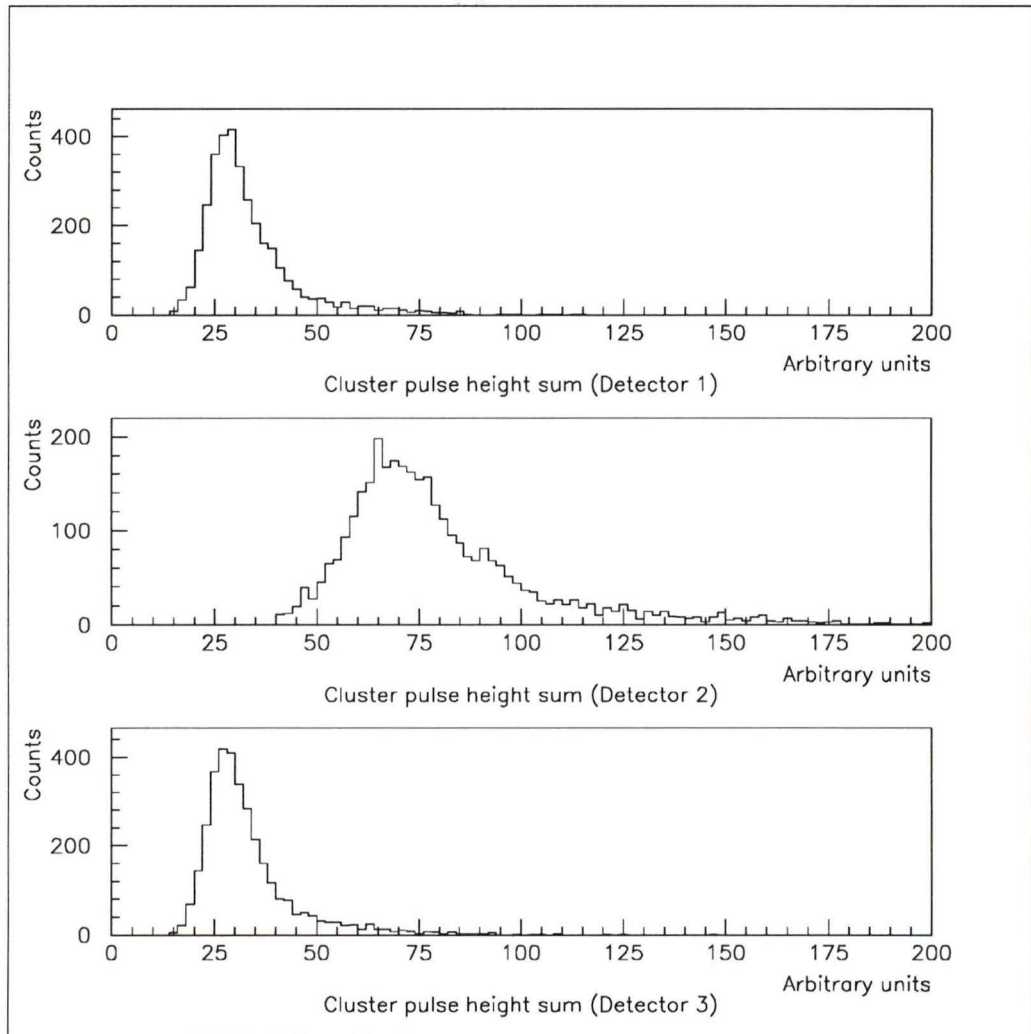


Figure 4.2: *Distribution of cluster pulse height sums. It should be noted that detector 2 was read out via an MX5 chip which has a larger gain than the MX3 chips used to readout detectors 1 and 3.*

A least squares fit was performed to the cluster pulse height sum histograms created with SITB110 using the program LANDPAR2 (written by the author) and the CERN MINUIT package [34]. The fitting function had two parameters which were free to vary within bounds: the σ_T in the Gaussian part of the convolution and N , the overall normalization of the fitting function. σ_T was allowed to vary from an initial value of 10.0 keV. The starting value of N was 75.0.

The parameters for the actual Landau distribution were fixed during the fit. A Landau distribution can be called from the CERN program libraries [35] with

$$\lambda = \frac{1}{A}[E - B] \quad (4.3)$$

and the fixed parameters were taken to be the calculated values $A = 5.35$ keV and $B = 83.50$ keV (see equation (A.11)).

The histograms for the cluster pulse height sums as defined through SITB110 were not calibrated in units of energy. In order to normalize the cluster pulse height sum histograms, the most probable value (MPV) of each histogram was found by fitting the four bins around the peak of the distributions for detectors 1 and 3 and the nine bins for detector 2, to a truncated Gaussian and using the mean value of this truncated Gaussian as the most probable value. This method avoided problems due to statistical fluctuations at the peaks. The histogram contents were normalized using this measured most probable value.

The fit of the convoluted Landau to the data was performed by minimizing the χ^2 given by

$$\chi^2 = \sum_{I=1}^M \left(\frac{C(I) - F(\sigma, N)}{E(I)} \right)^2 \quad (4.4)$$

where M equals the number of channels, F is the fitting function, $C(I)$ is the content of channel I , and $E(I)$ (the error) is the square root of the content of channel I .

In order for the parameters to be set to the same scale as the cluster pulse height sum histograms, they must be divided by the most probable value of a convoluted Landau function with the same fixed parameters. This MPV for a convoluted Landau function can be found through an iteration scheme.

- An initial value of $E_{MPV} = 82.2$ keV for the most probable value of the convoluted Landau function was assumed since 82.2 keV is the most probable value of the pure Landau distribution with $\lambda = \frac{1}{5.35 \text{ keV}}(E - 83.50 \text{ keV})$.
- The input parameters of the convoluted Landau function were divided by E_{MPV} and then were used to fit the cluster pulse height sum histograms. This fit produced the output parameter σ_{T1} from the Gaussian part of the convolution.
- A convoluted Landau distribution with σ_{T1} was then plotted and its MPV was found numerically.
- The input parameters of the convoluted Landau function were then divided by this new MPV and were used in the next fit of the cluster pulse height sum histograms giving a new σ_{T2} .

This iteration was continued until the change in σ_T was smaller than its error. The resulting most probable values used for the convoluted Landau are given in table 4.1. Note that smearing a Landau distribution with a Gaussian distribution shifts the most probable value of the distribution to a higher energy. The output parameters from the best fits (see figure 4.3) are given in table 4.2.

From figure 4.4, it can be seen that the σ_T for detector 2 is smaller than those for detectors 1 and 3. This result is as expected since the MX5 chip is supposed to have lower noise than the MX3 chip.

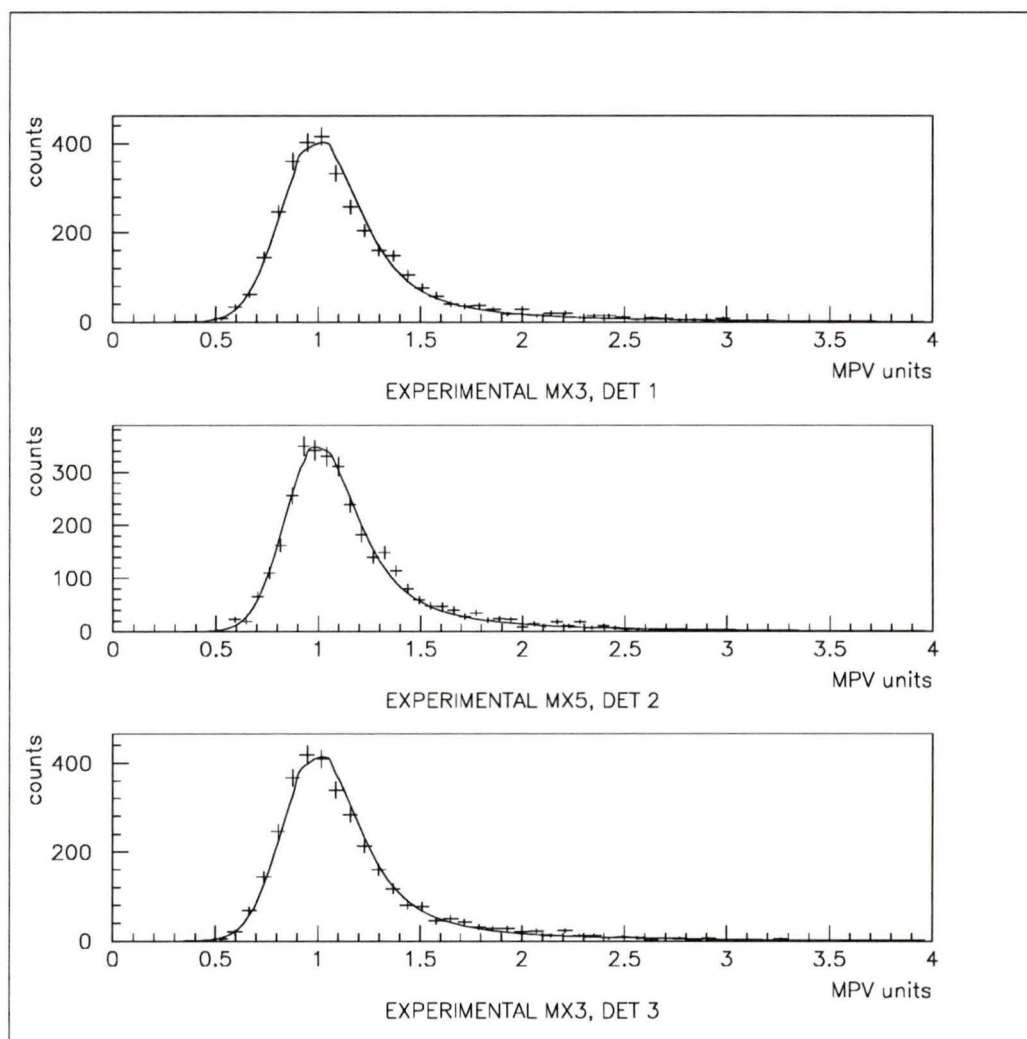


Figure 4.3: The distribution of cluster pulse height sums fitted to a Landau distribution convoluted with a Gaussian distribution.

MPV		
DETECTOR 1 (MX3)	DETECTOR 2 (MX5)	DETECTOR 3 (MX3)
(87.40±0.17) keV	(86.64±0.17) keV	(87.05±0.17) keV

Table 4.1: Table of most probable values of the convoluted Landau distribution found by the iteration scheme. The errors given in this table represent the smallest step size used when trying to find the MPV.

DETECTOR 1 (MX3)	DETECTOR 2 (MX5)	DETECTOR 3 (MX3)
$\sigma_T = (12.8 \pm 0.4)$ keV	(11.1 ± 0.4) keV	(12.1 ± 0.3) keV
$N = 77.5 \pm 1.4$	61.7 ± 1.1	77.3 ± 1.4
$\chi^2 = 69.2/38$ dof=1.8	$68.6/39$ dof=1.8	$58.8/40$ dof =1.5

Table 4.2: Table of output parameters of the convoluted Landau distributions fitted to the experimental energy loss histograms.

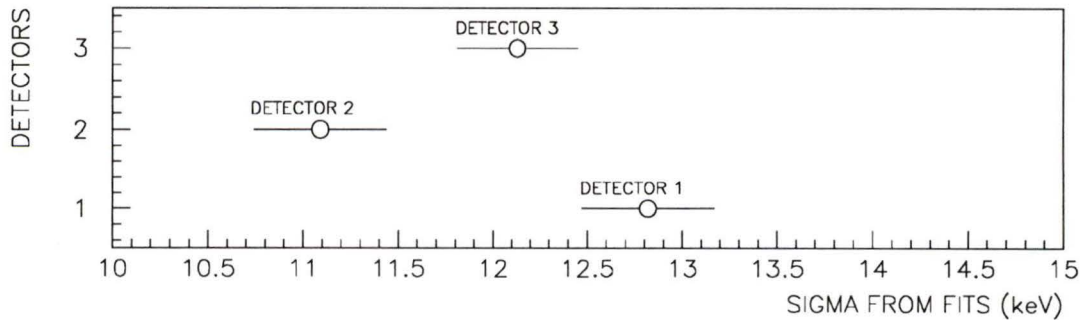


Figure 4.4: Detector by detector comparison of the σ_T from the least square fits.

σ_{noise}		
DETECTOR 1 (MX3)	DETECTOR 2 (MX5)	DETECTOR 3 (MX3)
(11.4 ± 0.4) keV	(9.5 ± 0.4) keV	(10.6 ± 0.4) keV

Table 4.3: Table of σ_{noise} values from the fits of the energy loss distributions.

By using equation (3.5), $\sigma_T = (33.1 \text{ keV}^2 + \sigma_{noise}^2)^{\frac{1}{2}}$, and the value of σ_T from the fits of the energy loss distributions (table 4.2), the σ_{noise} of detectors 1, 2, and 3 are given in table 4.3.

An estimate for σ_{noise} can also be found from the width of the pedestal distribution for each individual channel in each detector. This width has been measured for each channel contained in a good cluster. The value of σ determined from the pedestal distributions for each channel in a cluster is summed in quadrature assuming the noise values are uncorrelated. Figure 4.5 shows the histograms of the width of the pedestal added in quadrature for each channel in a cluster for all of the clusters in each detector. Recall that the gain in detector 2 is greater than in detectors 1 and 3.

The histograms in figure 4.5 are in ADC units and were subsequently converted to the appropriate energy units. The noise sum per cluster for detector 2 was then rebinned to have a similar number of bins as for the other two detectors. A good estimate for σ_{noise} is the most probable value of the noise sum per cluster histograms shown in figure 4.5. The most probable values for each distribution were found by fitting the bins around the peaks of the distributions to a truncated Gaussian (7 bins for detector 1, 5 bins of the rebinned histogram for detector 2, and 8 bins for detector 3). These values of σ_{noise} are given in table 4.4. The errors in table 4.4 were found by using the expression the SD/\sqrt{N} (standard deviation from the mean of the distribution divided by the square root of the number of bins) along with the errors

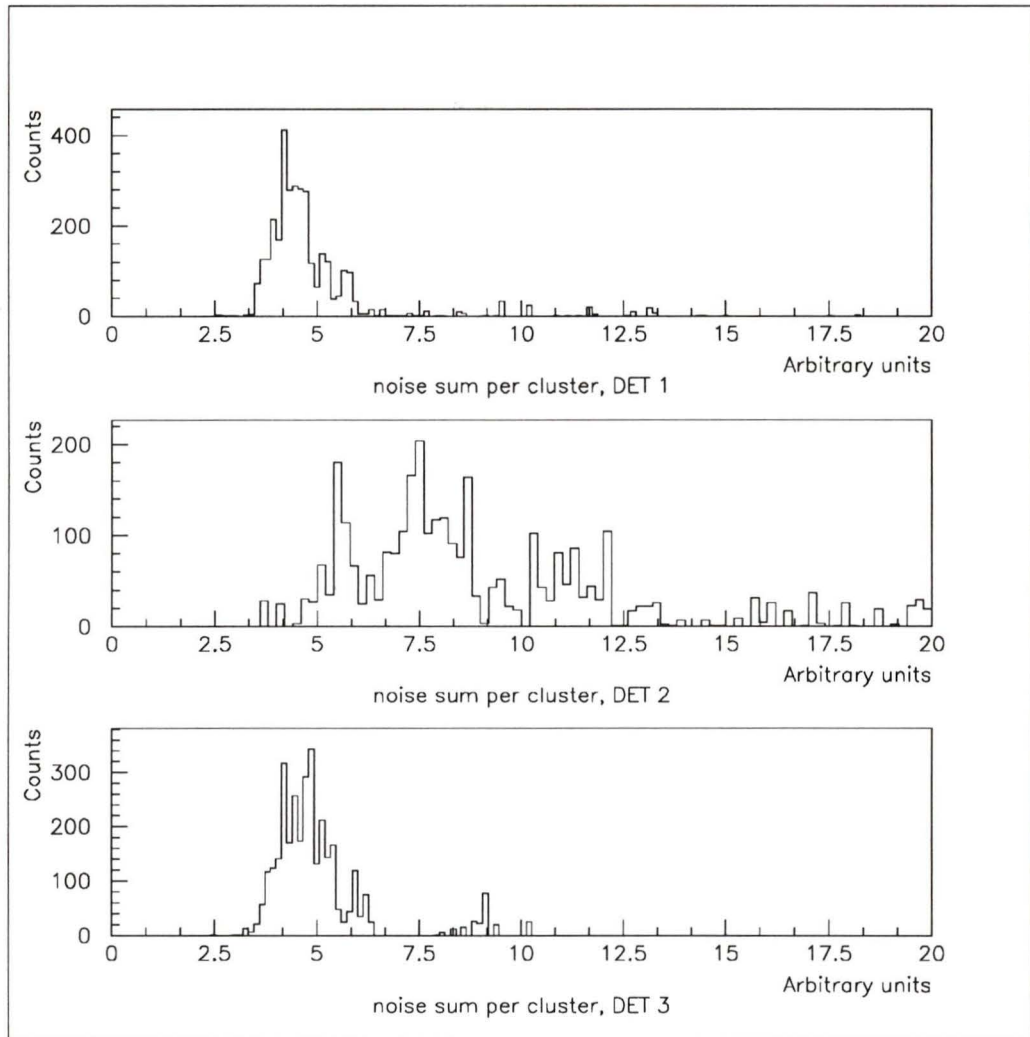


Figure 4.5: Distribution of the noise sum per cluster calculated at the pedestal level.

σ_{noise}		
DETECTOR 1 (MX3)	DETECTOR 2 (MX5)	DETECTOR 3 (MX3)
(13.7 ± 0.6) keV	(10.3 ± 0.7) keV	(13.9 ± 0.6) keV

Table 4.4: Table of σ_{noise} values from the truncated Gaussian fit of the peak.

Mean value		
DETECTOR 1 (MX3)	DETECTOR 2 (MX5)	DETECTOR 3 (MX3)
(15.1±0.6) keV	(11.2±0.7) keV	(15.2± 0.6) keV

Table 4.5: Table of mean values of the noise sum per cluster distributions.

associated with the most probable values of the convoluted Landau distributions found from the iteration scheme.

These values of σ_{noise} (the mean value of the truncated Gaussian fit) can be compared with the means of the histograms in figure 4.5. These mean values are given in table 4.5. Comparing table 4.4 and table 4.5 gives an estimate of the systematic errors in this method. The values from the mean seem to be about 1 keV higher than the σ_{noise} determined from the truncated Gaussian.

If the values for σ_{noise} determined by the truncated Gaussian (table 4.4) are compared to the values for σ_{noise} found from the convoluted Landau fits (table 4.3), it appears that using the width of the pedestal as a measure of the noise over estimates the smearing of the Landau distributions for detectors 1 and 3. However, the procedure appears to give a better agreement for detector 2.

4.1.1 Conclusions on Energy Loss from the silicon microvertex data

The cluster pulse height sum distributions of detector 1, 2, and 3 can be fitted by a convoluted Landau distribution. From the χ^2 s of the fits, it can be seen that the data are consistent with the theory of Landau distributions convoluted with a Gaussian distribution. The detector with the MX5 chips was found to have a lower electronic noise (σ_{noise}) than that of the other two detectors with MX3 chips as was expected.

The two methods for determining σ_{noise} (Landau fit and pedestal distributions)

are in good agreement for detector 2.

The σ_{noise} found from the fitting of the energy loss distribution to a convoluted Landau distribution gives a measure of the noise from the two arrangements of detector and readout chips.

4.2 Spatial Resolution Results

The resolution of the central detector can be determined by using information from the outer two detectors (recall that figure 3.4 shows this detector arrangement). The residual function [31] is defined as

$$\Delta = Y_2 - (aX_2 + b) \quad (4.5)$$

where

Δ is the difference between the position of the reconstructed cluster and the cluster position predicted by the outer two detectors,

Y_2 is the measured cluster position in the central detector,

X_2 is the distance between detectors 1 and 3, and

a, b are parameters in the line fit.

This function for various clusters is best described by two superposed Gaussians. The broader of the two Gaussians is due to the fact that one or more channels in a cluster had a significant contribution from a delta ray (a high energy recoil electron produced when energy is transferred from the pion beam to the silicon). Studies have been made [31] to choose appropriate selection criteria to get rid of these delta rays.

A final assumption is necessary for the determination of the spatial resolution. It is assumed that all detectors have identical signal-to-noise ratios. To ensure this,

values for Δ were extracted for events in which the signal-to-noise ratio was the same for each of the three detectors. These values for Δ were then fitted to a Gaussian in order to get $\sigma(\Delta)$. Then, for three equally spaced, identical detectors,

$$\sigma_{det 2} = \sqrt{\frac{2}{3}}\sigma(\Delta). \quad (4.6)$$

For a signal-to-noise ratio ranging between 12 and 15, the position resolution of the silicon microvertex detector is found to be $(4.1 \pm 0.2) \mu\text{m}$ [31].

An extensive study of the spatial resolution of the silicon microvertex is made in reference [31]. The energy resolution method used in [31] was obtained from this thesis.

The value of $4.1 \mu\text{m}$ for the spatial resolution of the silicon microvertex detector was calculated under the ideal test beam conditions and hence it represents a lower limit on the spatial resolution. Under normal OPAL conditions, particles do not always hit the detectors at normal incidence and so the spatial resolution may be expected to increase as $\frac{4.1 \mu\text{m}}{\cos \theta}$ where θ is the angle between the direction of the particle and the normal to the surface of the detector.

The OPAL silicon microvertex detectors are installed as two concentric barrels around a 1.1 mm thick beryllium (Be) beam pipe. The inner barrel consists of eleven ladders of three detectors and the outer barrel has fourteen ladders of three detectors. The distance from the center of the beam pipe to the first layer of detectors is 60.8 mm while the distance from the center of the beam pipe to the second layer of detectors is 75.2 mm. Figure 4.6 [36] shows a schematic cross section of part of this arrangement. In the actual detector arrangement, the silicon wafers are placed with their surfaces normal to the radius of the beam pipe.

The effective resolution of the microvertex detector will be worsened by multiple Coulomb scattering in the beam pipe (0.003 radiation lengths thick) and the inner

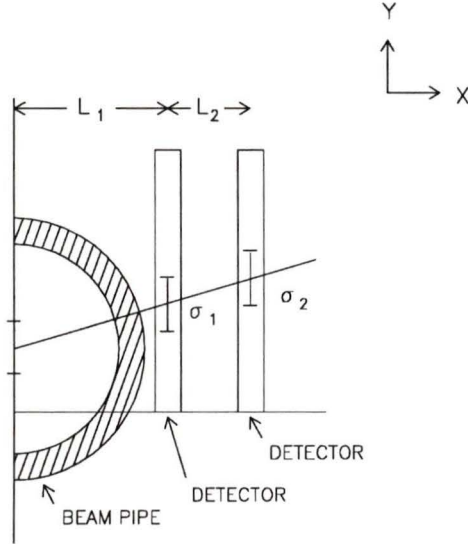


Figure 4.6: Schematic cross section of part of the OPAL detector. $L_1 = 60.8$ mm, $L_2 = 14.4$ mm, $\sigma_1 = \sigma_2 = 4.1$ μ m.

layer of the silicon detectors (also 0.003 radiation lengths thick). A 5 GeV/c pion will have a mean multiple scattering angle of 1.7×10^{-4} radians. In order to model this effect simply, the resolutions of the inner and outer silicon detector have been increased to 4.3 μ m and 6.0 μ m respectively.

4.3 The Error in Time Resolution

The average B_s^0 mesons (which have a momentum of about 30 GeV/c) will travel a mean distance of $L = \tau\gamma\beta c = \frac{\tau p}{m_o}$ before decaying. Since the lifetime of a B_s^0 meson is about $\tau = (1.37 \pm 0.07 \pm 0.06) \times 10^{-12}$ s [37] and assuming the mass of the B_s^0 meson to be about $m_o = 5.3$ GeV/c² [38], then the B_s^0 meson will travel about 2.2 mm before decaying. The error in this decay length will come from the errors in extrapolating tracks back to the B_s^0 decay vertex. On average, tracks of at least

two decay products of the B_s^0 will cross the two layers of silicon. The resolution in the decay length of the B_s^0 will depend on the opening angle, α , between these two tracks. From chapter 2, the angle between the jet axis of the B_s^0 decay products is about 10° . Hence, the opening angle will be $\alpha \approx 10^\circ - 20^\circ$. The resolution of the decay length of the B_s^0 can be expressed as

$$(\sigma_L)^2 = \frac{1}{\tan \alpha} \left[2 \left(1 + \left(\frac{L_1}{L_2} \right)^2 \right) (\sigma_{det 1})^2 + 2 \left(\frac{L_1}{L_2} \right)^2 (\sigma_{det 2})^2 \right] \quad (4.7)$$

with L_1 and L_2 as given in figure 4.6 and $\sigma_{det 1} = 4.3 \mu\text{m}$ and $\sigma_{det 2} = 6.0 \mu\text{m}$ are the effective resolutions as given in the previous section. For $\alpha \approx 10^\circ - 20^\circ$, then $\sigma_L \approx (120 - 250) \mu\text{m}$. Hence, $\frac{\sigma_L}{L} = 0.05 - 0.11$.

Since the time of flight of the B_s^0 is $\tau c = L/\beta\gamma$, the resolution of the time of flight is

$$\left(\frac{\sigma_{\tau c}}{\tau c} \right)^2 = \left(\frac{\sigma_L}{L} \right)^2 + \left(\frac{\sigma_{\beta\gamma}}{\beta\gamma} \right)^2. \quad (4.8)$$

From chapter 2, the fractional error on the boost is 0.08-0.13. From these results and the results derived above from the resolution of the decay length, the resolution of the time of flight of the B_s^0 at OPAL is $\sigma_\tau \approx (0.13 - 0.23)$ ps.

Chapter 5

B_s^0 Oscillation Simulations and Analyses

5.1 The Monte Carlo Method

The Monte Carlo method [39] uses random numbers to simulate processes which are too complex to derive analytically. However, it is more practical to use a reproducible list of numbers called pseudorandom numbers which are created by numerical algorithms.

Pseudorandom numbers which are uniformly distributed in the continuous interval $[0,1]$ can be generated by a CERN library routine [35]. These numbers can be transformed to new pseudorandom numbers whose density distribution is weighted by a given probability distribution function. The transformation can be accomplished analytically or by numerical methods such as the Von Neumann acceptance-rejection method [40].

These transformed pseudorandom numbers can be interpreted as sample possible outcomes of measurements of physical processes. Hence, these numbers are often called simulated events. The probability distribution function represents the density distribution of the possible outcome of measurements and as such will depend on

parameters specific to the physical process.

An application of the Monte Carlo method is the simulation by computer of stochastic processes which occur in particle physics. The author has written computer programs which use this Monte Carlo method. These programs use uniformly distributed pseudorandom numbers in the continuous interval $[0,1]$ which are transformed to other pseudorandom numbers that represent possible outcomes of the decay time in the rest frame of B_s^0 mesons that have not changed flavor before decaying. The creation of these sample events will be discussed in this chapter. The three methods used to recover the parameters of the parent probability distribution (mainly the frequency of oscillation) will also be explained in this chapter and are shown to work in the case of high B_s^0 statistics. In chapter 6, these three methods are applied to generated sets of sample events which contain a small number of sample events per set (25 to 200 sample events per set) in order to reflect the low number of identified B_s^0 expected from the experiment. The results of these analyses with low statistics will also be presented in chapter 6. The intent of these analyses is to see how well the frequency of oscillation of the parent distribution can be retrieved for low B_s^0 statistics.

5.2 The Simulation Programs

The Monte Carlo method is used to generate by computer a set of data that simulates the result of a measurement of B_s^0 oscillations. It is assumed the B_s^0 or \bar{B}_s^0 mesons have been identified and tagged as not having changed flavor before decaying using the techniques described in chapter 2. The decay lifetime will have already been measured from a much larger sample of identified B_s^0 meson decays that did not require the lepton tag of the associated \bar{B} meson in the opposite jet. In this work, the lifetime is taken to be 1.37 ps [37]. The data consist of decay times in the B_s^0

meson rest frame. The uncertainties on the measurement of the decay length in the laboratory and on the transformation to the rest frame have been calculated in chapter 2 for a typical LEP detector in and are folded together into a Gaussian resolution for the decay time in the rest frame.

A theoretical formula, (2.12), was developed in chapter 2 that describes the distribution of decay times expected for the data selected in the above manner. Writing equation (2.12) with the lifetime explicitly included, gives

$$I(B_s^o(t)) = e^{-\frac{t}{1.37}} \cos^2 \left(\frac{\omega}{1.37} t \right) \quad (5.1)$$

where t is in picoseconds and $I(B_s^o(t))$ is the intensity distribution of decay times for B_s^o and \bar{B}_s^o mesons that have not changed flavor before decaying. Approximately ten percent of events tagged as not having changed flavor before decaying will have in fact changed flavor but are misidentified because the lepton in the opposing jet has come from a B_s^o or a B_d^o meson that changed flavor before decaying. The exact percentage was shown in chapter 2 to depend on the oscillation frequency for B_d^o and B_s^o mesons. Therefore, a fraction of the data will be sampled from the distribution

$$I(\bar{B}_s^o(t)) = e^{-\frac{t}{1.37}} \sin^2 \left(\frac{\omega}{1.37} t \right). \quad (5.2)$$

where t is in picoseconds and $I(\bar{B}_s^o(t))$, equation (2.13), is the intensity distribution of decay times for B_s^o and \bar{B}_s^o mesons that have changed flavor before decaying.

Some events from background processes and detector limitations are expected and are included as a uniform distribution in time denoted by $U(t)$.

The sum of these three distributions is convoluted with the Gaussian distribution representing the time resolution of the experiment

$$g(t' - t) = \frac{1}{\sqrt{2\pi}\sigma} e^{-\left(\frac{t'-t}{\sqrt{2}\sigma}\right)^2} \quad (5.3)$$

where σ is the width of the resolution and $t' - t$ is the difference between the measured decay time and the actual decay time. The entire distribution can be written as

$$J(t) = \int_0^\infty \frac{1}{\sqrt{2\pi}\sigma} e^{-\left(\frac{t'-t}{\sqrt{2}\sigma}\right)^2} [(1-b)[(1-a)I(B_s^0(t')) + aI(\bar{B}_s^0(t'))] + b U(t')] dt' \quad (5.4)$$

where a is the fraction of incorrectly tagged B_s^0 mesons and b is the fraction of uniformly distributed background.

Rather than generate random samples of $J(t)$ through direct integration, it is more practical to break the problem up into several steps that are easy to solve numerically. The decay times are limited to the interval (0 to 7) ps or approximately five lifetimes. A set of uniform pseudorandom numbers over the interval (0 to 1) denoted by Λ are generated using the CERN library routine RNDM [35]. The following algorithm uses these numbers to generate a number randomly sampled from distribution (5.4).

1. A B_s^0 meson decay time or a background event is generated depending on whether a sample Λ_i from the set Λ is less than or greater than b ($\Lambda_i < b$ or $\Lambda_i > b$). In the former case, the next sample from Λ is transformed according to

$$U_i(t) = 7\Lambda_i \quad (5.5)$$

where Λ_i is an element of the pseudorandom numbers Λ and $U_i(t)$ represents a decay time sampled from the background event distribution $U(t)$. This transformation was used to create samples which were later analyzed by the fitting method. However, for sample events which were subsequently analyzed with the folding method, the transformation used was

$$U_i(t) = 10\Lambda_i. \quad (5.6)$$

The distribution extended to larger times was used because the folding method forces the use of a subset of the time axis of this decay lifetime distribution. Samples which were later analyzed with the Fast Fourier Transform (FFT) method were also generated with this larger transformation in order to compare its results with the folding method results as well as compare with a study [41] which used the FFT method on samples generated with a larger transformation.

2. In the latter case, $\Lambda_i > b$, a B_s^0 meson decay time is generated. The distribution (5.1) or (5.2) for non-oscillating or oscillating B_s^0 is used depending on whether another sample Λ_i is greater or less than a ($\Lambda_i > a$ or $\Lambda_i < a$). The Von Neumann Acceptance-Rejection method [40] uses elements of the pseudorandom number list Λ to yield a pseudorandom sample event $I_i(B_s^0(t))$ from distribution (5.1) over the interval (0 to 7) ps for the case $\Lambda_i > a$ or from a sample event $I_i(\overline{B}_s^0(t))$ from distribution 5.2 for the case $\Lambda_i < a$.
3. The result $U_i(t)$, $I_i(B_s^0(t))$, or $I_i(\overline{B}_s^0(t))$ from the first two steps must be corrected or “smeared” to account for the time resolution of the measurement. The convolution given in equation (5.4) is very easily accomplished numerically. A set of normally distributed pseudorandom numbers with mean equal to zero and standard deviation σ , denoted $g_i(t' - t)$, are generated with the CERN library computer code NORMCO [35]. Adding the number $g_i(t' - t)$ to whichever number $U_i(t)$ or $I_i(B_s^0(t))$ or $I_i(\overline{B}_s^0(t))$ was calculated in the first two parts yields a pseudorandom number $J_i(t)$ randomly chosen from the distribution (5.4) (*i.e.* a sample decay time from a simulated B_s^0 oscillation measurement).

The algorithm is repeated until the required number of events is generated.

The simulated data were then analyzed to see how well the parameters of the parent distributions could be recovered. Simulated data were generated with different numbers of events, a range of mistagging fractions and backgrounds, and a range of oscillation frequencies. Three different analysis techniques are described in this thesis. The main approach is a least squares fit to the data using a theoretical description that contains the maximum input from the Standard Model. It is expected that this should give the best sensitivity to the oscillation frequency. Two other methods are tried to estimate the amount of variation in sensitivity to the oscillation frequency expected from the differing techniques.

It is noted that the simulated data were actually calculated anew by each of the three analysis programs for each set of parent parameters and then immediately analyzed. The same Monte Carlo data generation algorithm is used by all three programs.

5.3 The Fitting Program

The first program discussed is called MCBMIN and will be referred to as the fitting method. This program fills a histogram with the Monte Carlo data generated according to the time evolution distribution given in (5.4) and fits the histogram contents with a theoretical function in an attempt to recover the original parameters of the parent distribution, especially the frequency of oscillation of the parent distribution. This section is devoted to the derivation of the theoretical function and the fitting method.

The derivation of the theoretical function used in the fitting of the generated data is based on the unsmeared distributions given in (5.1) and (5.2). If the percent

mistagging is defined as a , then the unsmeared time evolution is

$$f(x) = e^{-\frac{x}{\tau}} \left[(1-a) \cos^2\left(\frac{\omega x}{\tau}\right) + a \sin^2\left(\frac{\omega x}{\tau}\right) \right] \quad \text{for } x \geq 0 \quad (5.7)$$

and

$$f(x) = 0 \quad \text{for } x < 0. \quad (5.8)$$

where x is the decay time. This distribution is “smeared” with a Gaussian given by

$$g(x-t) = \frac{1}{\sqrt{2\pi}\sigma} e^{-\left(\frac{x-t}{\sqrt{2}\sigma}\right)^2}. \quad (5.9)$$

The smearing is accomplished by convoluting (5.7) with (5.9):

$$\begin{aligned} F(t) &= [f \otimes g](t) \\ &= \int_0^\infty \frac{1}{\sqrt{2\pi}\sigma} e^{-\left(\frac{x-t}{\sqrt{2}\sigma}\right)^2} e^{-\frac{x}{\tau}} \left[(1-a) \cos^2\left(\frac{\omega x}{\tau}\right) + a \sin^2\left(\frac{\omega x}{\tau}\right) \right] dx \end{aligned} \quad (5.10)$$

taking notice that the interval of integration is 0 to ∞ because the unsmeared function (5.7) is nonzero only in the time interval $x \geq 0$. Denoting the integrand by

$$h(x, t) = \frac{1}{\sqrt{2\pi}\sigma} e^{-\left(\frac{x-t}{\sqrt{2}\sigma}\right)^2} e^{-\frac{x}{\tau}} \left[(1-a) \cos^2\left(\frac{\omega x}{\tau}\right) + a \sin^2\left(\frac{\omega x}{\tau}\right) \right] \quad (5.11)$$

makes it possible to rewrite the integral as a sum of integrals

$$F(t) = [f \otimes g](t) = \int_0^\infty h(x, t) dx = \sum_{k=1}^\infty \int_{k-1}^k h(x, t) dx \quad (5.12)$$

where $x = y - 1 + k$ and k is an integer in the interval $(1, \infty)$. Therefore

$$F(t) = \sum_{k=1}^\infty \int_0^1 h(y - 1 + k, t) dy \quad (5.13)$$

or making the substitution $y = \frac{1}{2}(z + 1)$ gives

$$F(t) = \frac{1}{2} \sum_{k=1}^\infty \int_{-1}^1 h\left(\frac{1}{2}(z - 1) + k, t\right) dz. \quad (5.14)$$

The integral is then approximated to a finite sum by using Gaussian quadrature [42]. When using Gaussian quadrature, the function, $h(x, t)$, is replaced by an interpolating Legendre polynomial of degree $n - 1$. This polynomial is then fitted to the function $h(x, t)$ at the n zeros of the Legendre polynomial, z_i , with the corresponding weight factors, W_i , giving an approximation to the original integral. Using Gaussian quadrature, the function $F(t)$ is approximated to

$$F(t) \approx [f \otimes g](t) = \frac{1}{2} \sum_{k=1}^{\infty} \sum_{i=1}^n W_i h\left(\frac{1}{2}(z_i - 1) + k, t\right) \quad (5.15)$$

where the integrand is evaluated at tabulated [42] values of z_i and summed with tabulated weights W_i [42]. The integral is exact for any polynomial of degree less than or equal to $2n + 1$.

The exponential term $e^{-\frac{x}{\tau}}$ in the integral forces the function quickly to zero as x increases. Therefore, the substitution $\sum_{k=1}^{\infty}$ to $\sum_{k=1}^m$ can be made. Truncating the sum at $m = 7$ is sufficient to give a good approximation to the integral. Furthermore, the integral evaluated as a function of n shows no significant difference for $n = 5$ and $n = 10$, so the conservative value of $n = 10$ is used. Finally, writing the integral out in full gives

$$\begin{aligned} F(t) &= [f \otimes g](t) \\ &= \frac{1}{2\sigma} \frac{1}{\sqrt{2\pi}} \sum_{k=1}^7 \sum_{i=1}^{10} W_i e^{-\frac{(x_i - t)^2}{2\sigma^2}} e^{-\frac{x_i}{\tau}} \left[(1 - a) \cos^2\left(\frac{\omega x_i}{\tau}\right) + a \sin^2\left(\frac{\omega x_i}{\tau}\right) \right] \end{aligned} \quad (5.16)$$

where $x_i = \frac{1}{2}(z_i - 1) + k$. Note that the only time dependence is given by the Gaussian.

The flat background smeared with a Gaussian distribution is now included. The smearing is equivalent to the convolution

$$G(t) = \int_0^{\infty} \frac{1}{\sqrt{2\pi}\sigma} e^{-\left(\frac{x-t}{\sqrt{2}\sigma}\right)^2} dx = \frac{1}{2} \operatorname{erfc}\left(-\frac{t}{\sqrt{2}\sigma}\right). \quad (5.17)$$

Before adding $F(t)$ and $G(t)$ together, the normalization for each of these distributions must be calculated. The integral is considered to be significantly nonzero in the interval $-1 \leq t \leq 7$ (the integral at 7 ps is less than 0.01 times the value of the integral at 0 ps). The negative times are due to the smearing. Therefore normalizing $F(t)$ is equivalent to calculating

$$F_1 = \int_{-1}^7 F(t) dt = \frac{1}{2} \sum_{k=1}^7 \sum_{i=1}^{10} \left[\left(-\frac{1}{2} \right) \left[\operatorname{erf} \left(\frac{x_i - 7}{\sqrt{2}\sigma} \right) - \operatorname{erf} \left(\frac{x_i + 1}{\sqrt{2}\sigma} \right) \right] \right] \times \\ W_i e^{-\frac{x_i}{\tau}} \left[(1 - a) \cos^2 \left(\frac{\omega x_i}{\tau} \right) + a \sin^2 \left(\frac{\omega x_i}{\tau} \right) \right]. \quad (5.18)$$

Similarly, normalizing $G(t)$ involves calculating

$$G_1 = \int_{-1}^7 G(t) dt \\ = \frac{1}{2} \left[7 \operatorname{erfc} \left(-\frac{7}{\sqrt{2}\sigma} \right) + \operatorname{erfc} \left(-\frac{-1}{\sqrt{2}\sigma} \right) - \frac{\sqrt{2}\sigma}{\sqrt{\pi}} \left(e^{-\frac{7^2}{2\sigma^2}} - e^{-\frac{(-1)^2}{2\sigma^2}} \right) \right] = 7. \quad (5.19)$$

where G_1 is equal to 7 to better than 1 part in 10^{14} .

Thus, the theoretical function describing the data is

$$I(t) = \frac{(1 - b)}{F_1} F(t) + \frac{b}{G_1} G(t). \quad (5.20)$$

where b is the fraction of uniform background.

The effects of mistagging, smearing, and of adding flat background to the distribution of decay times for non-oscillating B_s^0 and \bar{B}_s^0 mesons is shown in figure 5.1. Figure 5.1a is a plot of distribution (5.1). Figure 5.1b shows that ten percent mistagging fills in the troughs and reduces the peaks of the distribution. Figure 5.1c shows that smearing extends the probability distribution to negative t . Adding a flat background keeps the probability distribution from reaching zero at large time as can be seen in figure 5.1d.

The CERN minimization package MINUIT [34] was used in order to fit $I(t)$ to the data generated from distribution (5.4). Four parameters were varied: $\frac{\omega}{\tau}$, a , b ,

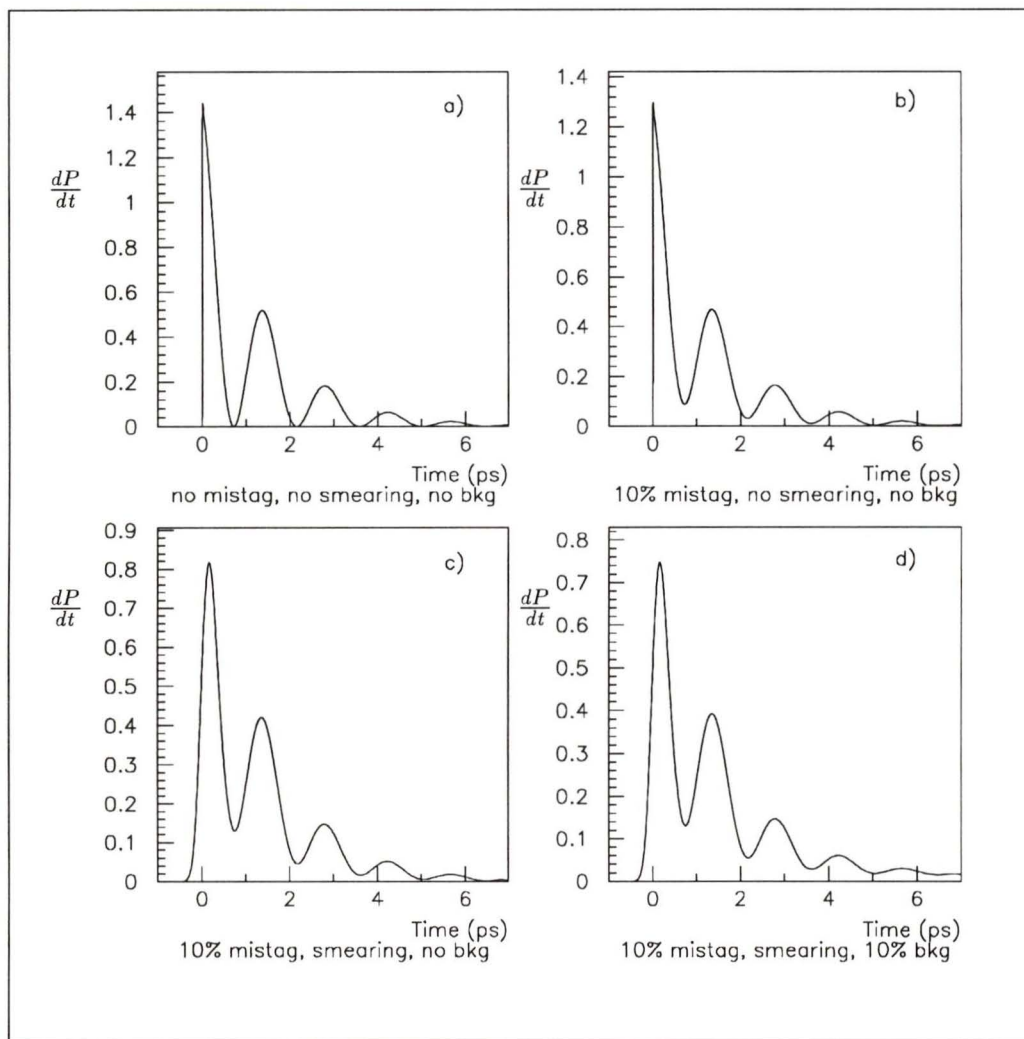


Figure 5.1: Probability distribution of observing a non-oscillating B^0 for $\frac{\epsilon}{\tau} = 2.19 \text{ ps}^{-1}$ and $\tau = 1.37 \text{ ps}$ with: a) no mistagging, no smearing, and no flat background; b) 10 percent mistagging, no smearing, and no flat background; c) 10 percent mistagging, 10 percent smearing, and no flat background; and d) 10 percent mistagging, 10 percent smearing, and 10 percent flat background. The area under these curves is 1. Note the change in scale in the y-axis of these curves.

and an overall normalization, A which was used to match the function, $I(t)$, to the number of entries in the histogram.

One of the main purposes of this program is to find out how few data measured in an experiment with a parent distribution (5.4) are needed in order to be able to still fit the distribution and hence be able to measure the quantity $\frac{\mathcal{E}}{\tau} = \frac{1}{2}\Delta M$. In chapter two where the tagging of the B mesons was explored, it was shown that one million Z^0 implied getting less than a few hundred properly identified B^0 oscillations. If a sample of 100 to 200 events are generated from the time evolution equation (5.4) and these numbers are binned in 0.1 ps bins over an interval of -1 ps to 7 ps (80 bins in all), the number of events per bin will be small. Therefore, a method such as finding the maximum log likelihood using Poisson statistics to fit a function to data with low statistics should be used. The Poisson distribution is appropriate because the probability of a decay time being in any given time bin is small.

Consider the Poisson distribution

$$P_p(n_i, Y_i) = \frac{Y_i^{n_i}}{n_i!} e^{-Y_i} \quad (5.21)$$

where Y_i is the expected content of bin i and n_i is the actual bin content of bin i . The total probability for N bins is the product

$$P_{TOT} = \prod_{i=1}^N P_p(n_i, Y_i) = \prod_{i=1}^N \frac{Y_i^{n_i}}{n_i!} e^{-Y_i} \quad (5.22)$$

and so the natural logarithm is the sum

$$\ln P_{TOT} = \sum_{i=1}^N (-Y_i + n_i \ln Y_i - \ln(n_i!)). \quad (5.23)$$

The last term in this expression is a constant so maximizing $\ln P_{TOT}$ is equivalent to maximizing

$$\sum_{i=1}^N (-Y_i + n_i \ln Y_i)$$

or minimizing the negative,

$$\sum_{i=1}^N (Y_i - n_i \ln Y_i). \quad (5.24)$$

The above expression is minimized using the CERN minimization package MINUIT [34]. Using the maximum log likelihood method with Poisson statistics at high statistics (i.e. greater than about 30 events per bin) gives equivalent results to using the χ^2 method.

In the expression (5.24), the expected bin content at bin i , Y_i , is the theoretical function value at bin i . Since the bin has a finite size, then where within the bin must the function be evaluated? Using the value of the theoretical function at the center of the bin only is correct if the function is linear over the bin. In general for a theoretical function defined as $f(t)$, then the correct value to use is the average over the bin size (the interval (a,b))

$$\frac{\int_a^b f(t) dt}{b - a}.$$

It is easy to see that for $f(t) = mt + c$, the above integral gives the function at the center of the bin, $f(\frac{a+b}{2})$, as expected. Hence in expression (5.24), the value

$$Y_i = \frac{\int_{bin\ i} I(t) dt}{bin\ size}$$

where $I(t)$ is equation (5.20).

A high B_s^0 statistics run was performed to verify that the derived fitting function (5.20) is correct. 10000 events were generated according to distribution (5.4) with the parameters $\omega/\tau = 2.19 \text{ ps}^{-1}$, 10 percent mistagging and 10 percent background and histogrammed with a time bin size of 0.1 ps. Figure 5.2 shows the fitting function superposed on the generated data. The resulting parameters from the fit were $\omega/\tau = (2.19 \pm 0.01) \text{ ps}^{-1}$, mistagging = 0.10 ± 0.01 , and background =

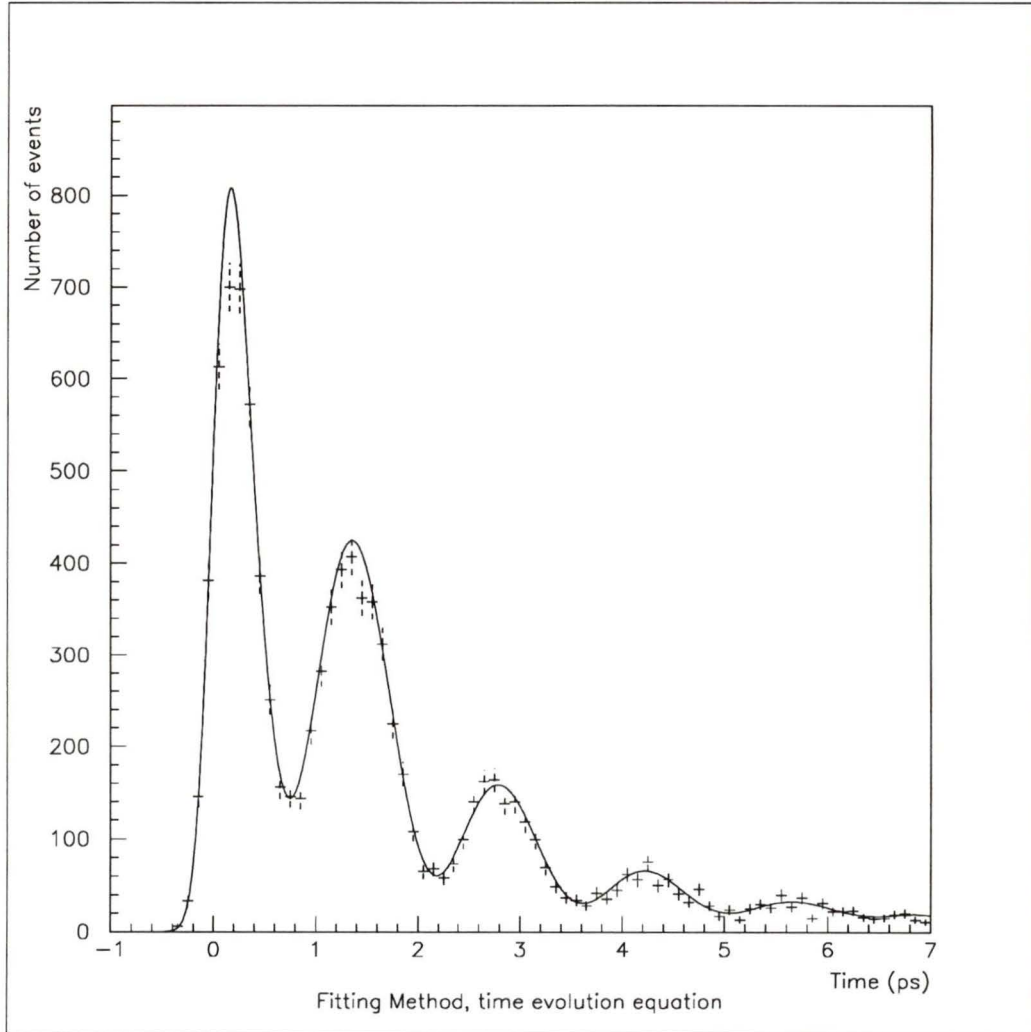


Figure 5.2: A high statistics run for the fitting method where the fitting function is superposed on the 10000 generated data for the input parameters: $\frac{\omega}{\tau} = 2.19 \text{ ps}^{-1}$, $\sigma = 0.13$, $\tau = 1.37 \text{ ps}$, mistagging = 0.10, background = 0.10, and 0.1 ps bin size. The output parameters of the fit were: $\omega/\tau = (2.19 \pm 0.01) \text{ ps}^{-1}$, mistagging = 0.10 ± 0.01 , and background = 0.10 ± 0.01 .

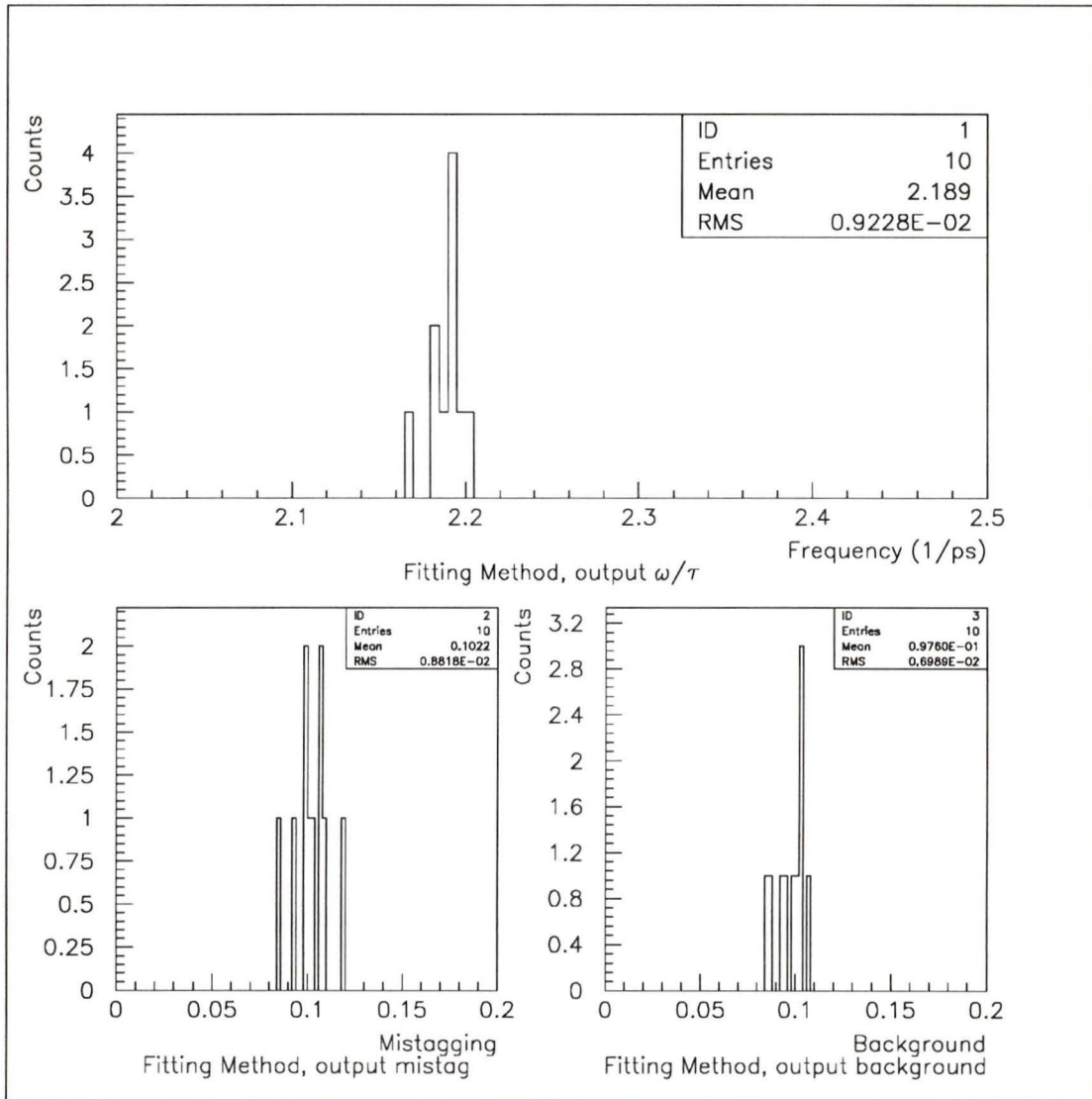


Figure 5.3: Results of high statistics fits with the fitting method which were repeated for 10 sets of 10000 events. The 10000 events for each fit were generated with the input parameters: $\frac{\omega}{\tau} = 2.19 \text{ ps}^{-1}$, $\sigma = 0.13$, $\tau = 1.37 \text{ ps}$, mistagging = 0.10, background = 0.10, and 0.2 ps bin size. The mean and standard deviation (SD) values for the output parameters of the fit were: mean = 2.19 ps^{-1} and SD = 0.01 ps^{-1} for the output ω/τ distribution, mean = 0.10 and SD = 0.01 for the output mistagging distribution, and mean = 0.1 and SD = 0.01 for the output background distribution.

0.10 ± 0.01 . This fitting function was able to successfully recover the parameters of the parent distribution.

This high statistics fit was repeated for 10 sets of 10000 events generated from equation (5.4) with the resulting ω/τ , percent mistagging, and percent background from each fit of 10000 events stored in histograms. Figure 5.3 shows that the results from these fits are consistent with the input values.

5.4 The Folding Program

The second program discussed, MCB2, was written to compare the fitting method which makes full use of the theoretical prediction of the Standard Model with a more general approach. It will be referred to as the folding method. A folding technique discussed below was used on the data to find the frequency of oscillation of the parent distribution used to generate the Monte Carlo data by searching for the dominant periodicity in the data.

The Folding Method

The folding method goes as follows:

- The program generates data as described before and bins it with a bin size, x_{bin} , chosen by the user. See for example figure 5.4a where the bin size is about 0.2 ps.
- The time axis of this distribution is then sectioned into time intervals of size x_{int} also chosen by the user by starting at the lowest bin, -0.5 ps. In figure 5.4b the interval size is about 1.4 ps.
- Then, the bin contents of the first bin (which has size x_{bin}) of each of the intervals of size x_{int} are added together and histogrammed, the bin contents of

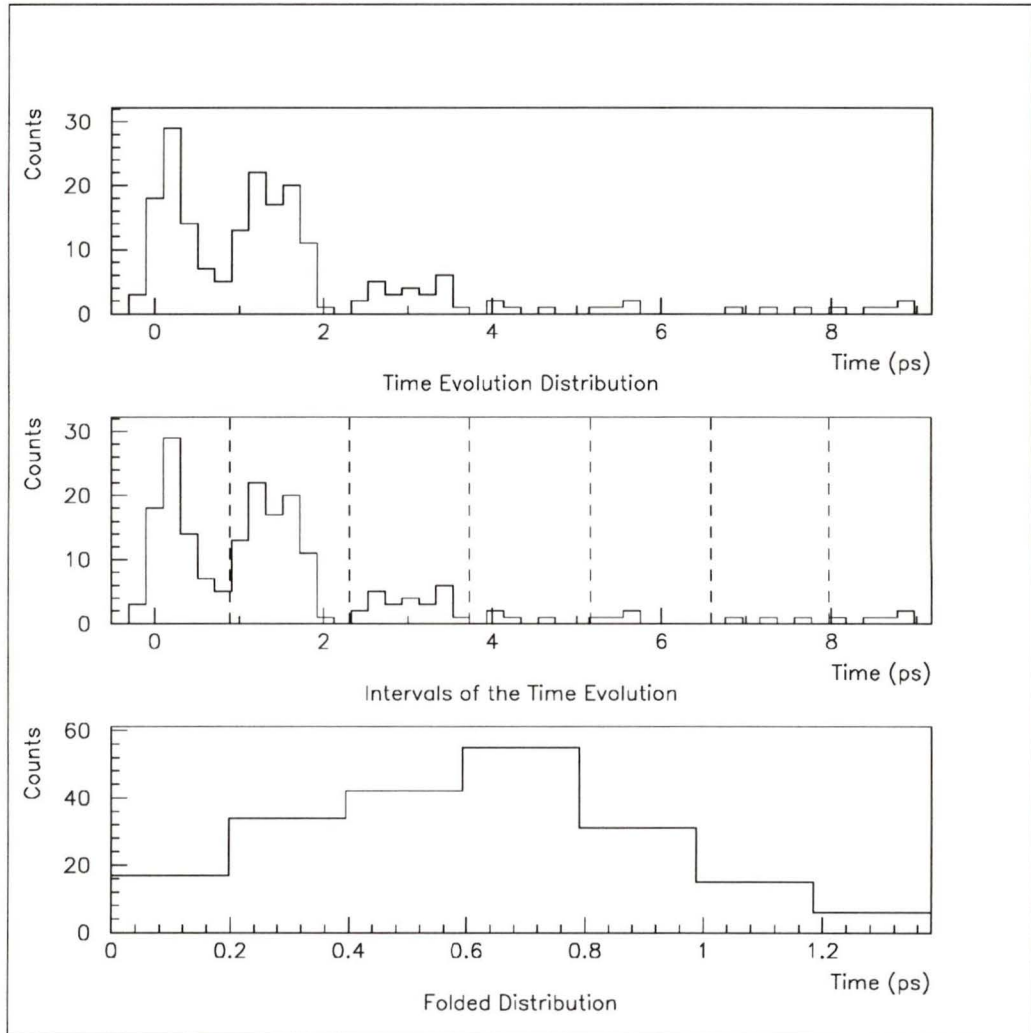


Figure 5.4: a) Distribution binned with bin size $x_{bin} \approx 0.2$ ps for $\frac{\omega}{\tau} = 2.19$ ps $^{-1}$, $\sigma = 0.13$ $\tau = 1.37$ ps, 10 percent mistagging, and 10 percent background. b) The distribution in a) is divided into intervals of $x_{int} \approx 1.4$ ps. c) The resulting distribution after folding.

the second bin of each of the intervals are added together and histogrammed etc... until all the bins in the interval have been used. It is as if the time axis is folded into intervals of x_{int} and the corresponding bins from each interval were added.

The result of this folding is a histogram of size x_{int} and bin size x_{bin} (see figure 5.4c).

The CERN minimization package MINUIT [34] performs the folding of this distribution while varying x_{int} and x_{bin} within preset bounds until the height difference between the highest point and lowest point of the folded distribution is a maximum. This maximum occurs when x_{int} is equal to the period of the function. This can easily be seen with a cosine wave. When the size of the interval, x_{int} , is equal to half a period the folding will add destructively and the resulting folding distribution will be flat. At x_{int} equal to the period, the folding will add constructively resulting in a folded distribution which looks like one period of a cosine wave. Folding with x_{int} between zero and one period will result in an oscillation with amplitude less than the amplitude at x_{int} equal to one period.

There is a limitation with this method. Since the highest point of the folded distribution must be compared with the lowest point, the distribution must have at least two bins within the interval. Hence, the minimum interval size is two bin widths.

The bin width must be chosen with experimental considerations in mind. The fact that the time resolution of a detector is of the order of 0.1 ps has been previously discussed. It makes no sense to choose a bin size less than 0.1 ps. Also, the bin size must not be chosen too large since it was mentioned above that the interval width must be at least two bin widths wide and hence a large bin width would limit the minimum size of time interval that can be explored. For these reasons, the author has chosen the bounds of the bin size over which MINUIT can vary to be 0.1 ps

to 0.2 ps. This implies that the minimum time interval that can be used is 0.4 ps. Since $\frac{\omega}{\tau} = \frac{\pi}{\text{period}}$ in distribution (5.4), frequencies $\frac{\omega}{\tau}$ up to 7.85 ps^{-1} (or $\omega = 10.76$) can be explored.

High statistics runs were also performed with the folding method in order to verify the performance of this method. The folding method was applied to 10000 events generated according to a $\cos^2(\frac{\omega}{\tau}t)$ distribution where $\omega/\tau = 2.19 \text{ ps}^{-1}$. This folding method was repeated with 25 sets of 10000 events. Figure 5.5 shows the results of the output frequency for these 25 sets. From this figure, it is shown that the folding method is able to successfully recover the frequency of the parent distribution $\cos^2(\frac{\omega}{\tau}t)$.

The folding method was also applied to 100 sets of 10000 events generated according to distribution (5.4) for the input parameters $\omega/\tau = 2.19 \text{ ps}^{-1}$, 10 percent mistagging, 10 percent background, and a time bin size of 0.03 ps. The results of these foldings are shown in figure 5.6 where it can be seen that the output frequency is not consistent with the input ω/τ . This same folding method was applied to data generated with a higher input ω/τ and the results were found to be consistent with the input ω/τ within the time bin size of 0.03 ps. The discrepancy at lower frequency is attributed to the exponential term in equation (5.4) which most affects low input ω/τ by shifting the measured frequency.

It must be noted that the folding method measures any periodicity in the data but offers no further understanding to the phenomenon of B_S^O oscillations.

5.5 The Fast Fourier Program

The final program to be discussed, MCB2FFT, uses a Fast Fourier Transform (FFT) method. An FFT of the data is used to find the frequency of oscillation of the data generated from distribution (5.4). The results of this program will be used as a

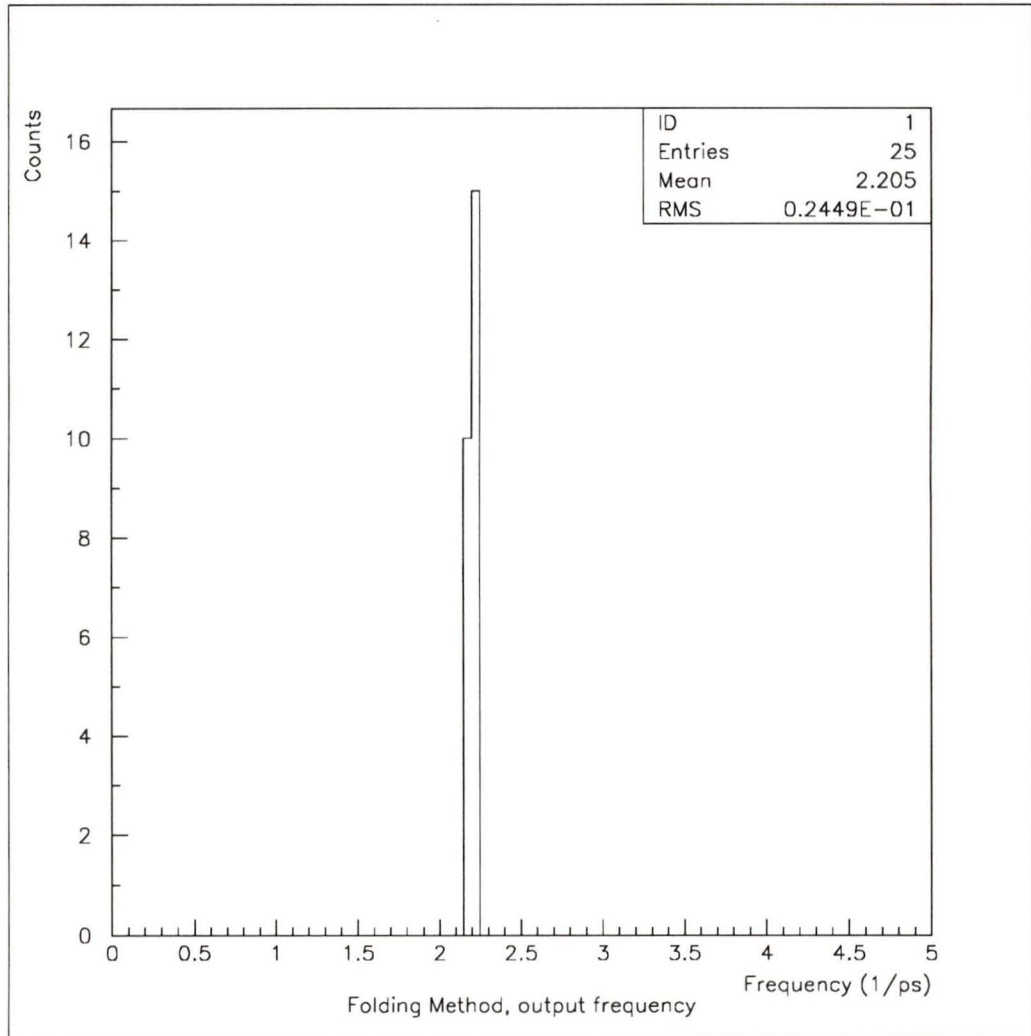


Figure 5.5: Results of high statistics runs with the folding method on a $\cos^2(\frac{\omega}{\tau}t)$ distribution which were repeated for 25 sets of 10000 events. The input ω/τ was 2.19 ps^{-1} with a 0.03 ps bin size. The mean of the output frequency distribution which has a bin size of 0.05 ps^{-1} is 2.20 ps^{-1} with a standard deviation of 0.02 ps^{-1} .

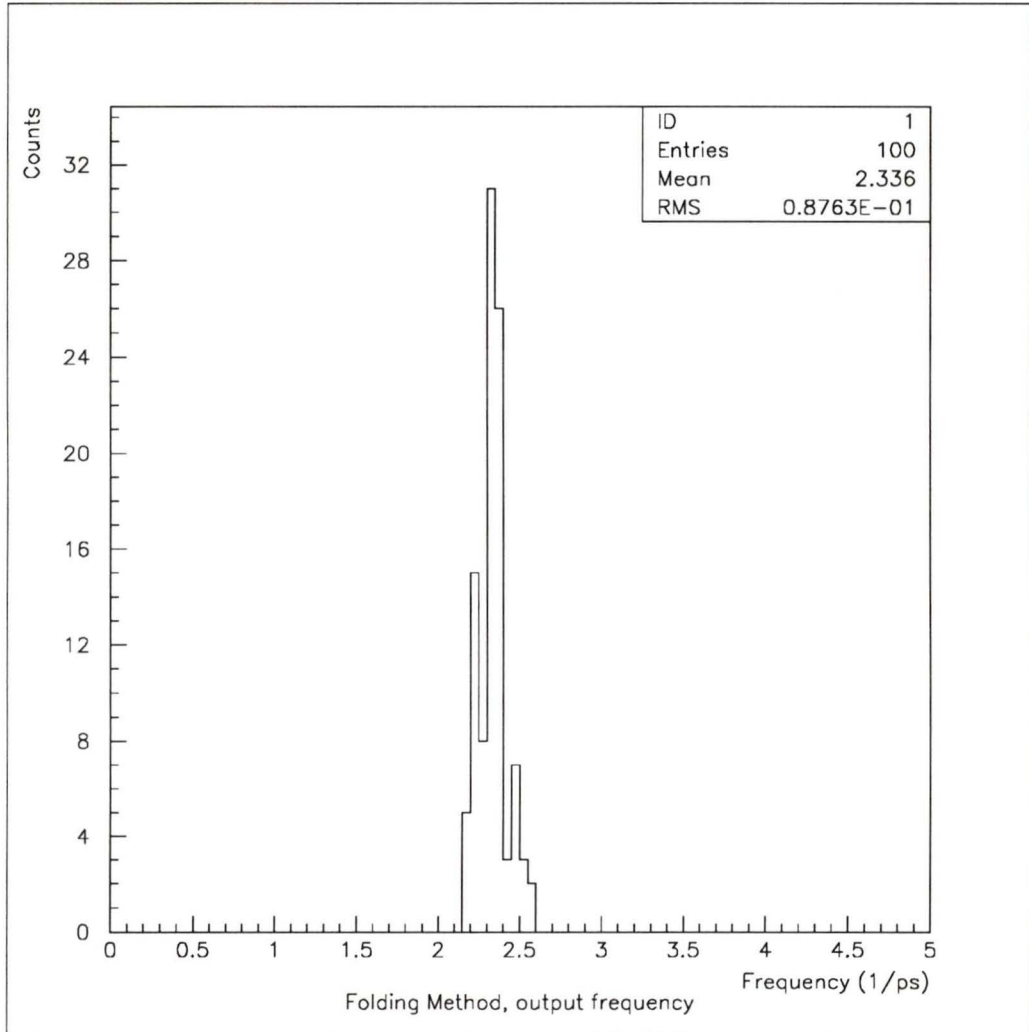


Figure 5.6: Results of high statistics runs with the folding method which were repeated for 100 sets of 10000 events. The 10000 events for each folding were generated with the input parameters: $\frac{\omega}{\tau} = 2.19 \text{ ps}^{-1}$, $\sigma = 0.13 \tau = 1.37 \text{ ps}$, mistagging = 0.10, background = 0.10, and 0.03 ps bin size. The mean and standard deviation values for the output frequency distribution which has a 0.05 ps^{-1} bin size are 2.34 ps^{-1} and 0.09 ps^{-1} respectively.

verification of the results from the fitting method.

Fast Fourier Transforms

A Fast Fourier Transform is performed on the data generated according to the distribution (5.4) in order to find its frequency of oscillation. This method was proposed and studied by Moser [41] in 1990.

A distribution in time, $g(t)$, has a Fourier Transform given by

$$G(\nu) = \int_{-\infty}^{\infty} g(t) e^{-2\pi i \nu t} dt \quad (5.25)$$

where ν is the frequency. The Fourier transform can be approximated by a Fast Fourier Transform

$$G_k = \frac{1}{N} \sum_{n=0}^{N-1} g_n e^{-\frac{2\pi i k n}{N}} \quad (5.26)$$

for $N = 2^m$ where m is a positive integer and $k = 0, 1, \dots, 2^{(m-1)} + 1$. The numbers g_n are the bin contents of a histogram of $g(t)$ consisting of N equal time bins. G_k is an array of complex numbers representing histograms of the real and imaginary parts of the Fourier Transform of $g(t)$.

The CERN program library [35] routine, RFFT, is used to calculate the FFT of an array necessarily 2^m elements long, of the bin contents of a histogram of the simulated B_s^0 decay times produced by Monte Carlo. The program is run with $m = 6$ (or 64 bins) and $m = 7$ (or 128 bins). This corresponds to time bins of 0.164 ps and 0.082 ps respectively.

The amplitude distribution or frequency spectrum is calculated as the square root of the sum of the squares of the real and imaginary parts of the output of the FFT. It peaks at the dominant frequency of the parent distribution. The maximum frequency of the amplitude distribution depends on the bin size of the time distribution g_n . The critical frequency is $\omega_c = \left(\frac{\omega}{\tau}\right)_{max} = \frac{\pi}{(\text{time bin width})}$. Hence $\left(\frac{\omega}{\tau}\right)_{max} =$

19 ps⁻¹ for 2⁶ time bins and $(\frac{\omega}{\tau})_{max} = 38$ ps⁻¹ for 2⁷ time bins. The bin width of the amplitude distribution is given by

$$\frac{(\frac{\omega}{\tau})_{max}}{2^{(m-1)} + 1}$$

which gives an amplitude distribution bin width of about 0.6 ps⁻¹ for $m = 6$ and $m = 7$. Hence, using 2⁷ bins allows a larger range of output frequency to be explored but does not improve on the resolution of the amplitude distribution. This frequency bin width of the amplitude distribution depends mostly on the length of the span of time which the data cover. This relation is given by

$$\begin{aligned} \text{bin width} &= \frac{(\frac{\omega}{\tau})_{max}}{2^{(m-1)} + 1} = \left(\frac{\pi}{\Delta t}\right) \left(\frac{1}{2^{(m-1)} + 1}\right) \\ &= \frac{2^m \pi}{T_{tot}} \frac{1}{2^{(m-1)} + 1} \approx \frac{2\pi}{T_{tot}} \end{aligned}$$

where Δt is the time bin width of the decay time histogram and T_{tot} is Δt times the number of bins or the total time interval of the histogram. The data represent the times of flight before decay of the B_s^0 mesons and since the lifetime of the B_s^0 is about 1.37 ps, the time span which these times of flight cover is of the order of 10 ps. Hence, a realistic frequency bin width is about 0.6 ps⁻¹.

Figure 5.7a) shows an amplitude distribution which is the output of an FFT applied to 50000 sample events generated from distribution (5.4) and binned into 2⁸ = 256 bins. A larger $T_{tot} = 50.5$ ps or a frequency bin size for the amplitude distribution of 0.12 ps⁻¹ was used for this high statistics run to minimize the effect of large frequency bins. The input ω/τ was 2.19 ps⁻¹ with 10 percent mistagging, 10 percent background, a time bin size for events generated from distribution (5.4) of 0.2 ps. The arrow in figure 5.7a) shows the peak frequency of the distribution. Since distribution (5.4) is a $\cos^2 \frac{\omega}{\tau} t$ distribution, dividing this peak value by 2 gives the appropriate $\frac{\omega}{\tau}$ (the output $\frac{\omega}{\tau}$ is about 2.28 ps⁻¹ in this figure). The $1/\omega$ curve at

low frequency in this figure is due to the exponential term in distribution (5.4). The program used the first local maximum after the $1/\omega$ curve as the peak frequency of the distribution. The difference between the peak of this amplitude distribution and the input ω/τ is within the bin size of the amplitude distribution. Figure 5.7b) is the amplitude distribution with the analytically calculated fourier transform of the exponential term convoluted with a Gaussian subtracted out. Random peaks in the amplitude distribution appear for a small total number of events because of statistical fluctuations in the contents of the time bins. The peak of this distribution is still 2.28 ps^{-1} and so any discrepancy between the peak of the amplitude distribution in figure 5.7a) and the input ω/τ due to the exponential term in distribution (5.4) is hidden by the bin size of the amplitude distribution.

This high statistics FFT was also performed with the more experimentally realistic frequency bin size of 0.6 ps^{-1} and $2^6 = 64$ time bins. Figure 5.8a) and b) show the amplitude distributions with and without the exponential term. The peaks of both distributions are 2.32 ps^{-1} which is consistent with the input 2.19 ps^{-1} for such a large frequency bin width.

In a sense, the folding method and the FFT method are alike since both methods find the main frequency component of the parent distribution.

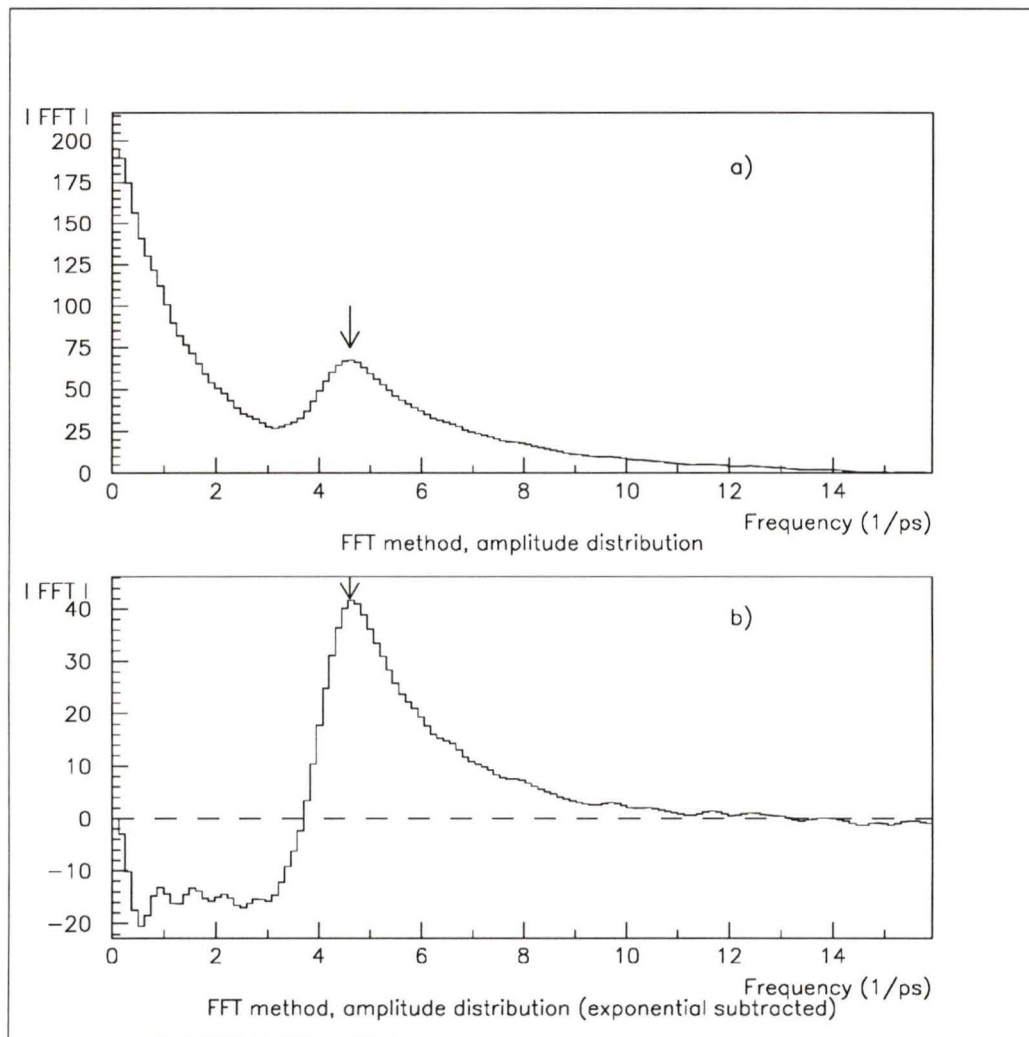


Figure 5.7: a) Amplitude distribution from an FFT applied to 50000 events binned into 0.2 ps bins for $\frac{\omega}{\tau} = 2.19 \text{ ps}^{-1}$, $\sigma = 0.13 \text{ ps}$, $\tau = 1.37 \text{ ps}$, 10 percent mistagging, 10 percent background, and frequency bin size of 0.12 ps^{-1} . The arrow shows the peak frequency at 2.28 ps^{-1} . b) Amplitude distribution from an FFT applied to 50000 events with the exponential term subtracted and binned into 0.2 ps bins for $\frac{\omega}{\tau} = 2.19 \text{ ps}^{-1}$, $\sigma = 0.13 \text{ ps}$, $\tau = 1.37 \text{ ps}$, 10 percent mistagging, 10 percent background, and frequency bin size of 0.12 ps^{-1} . The arrow shows the peak frequency at 2.28 ps^{-1} .

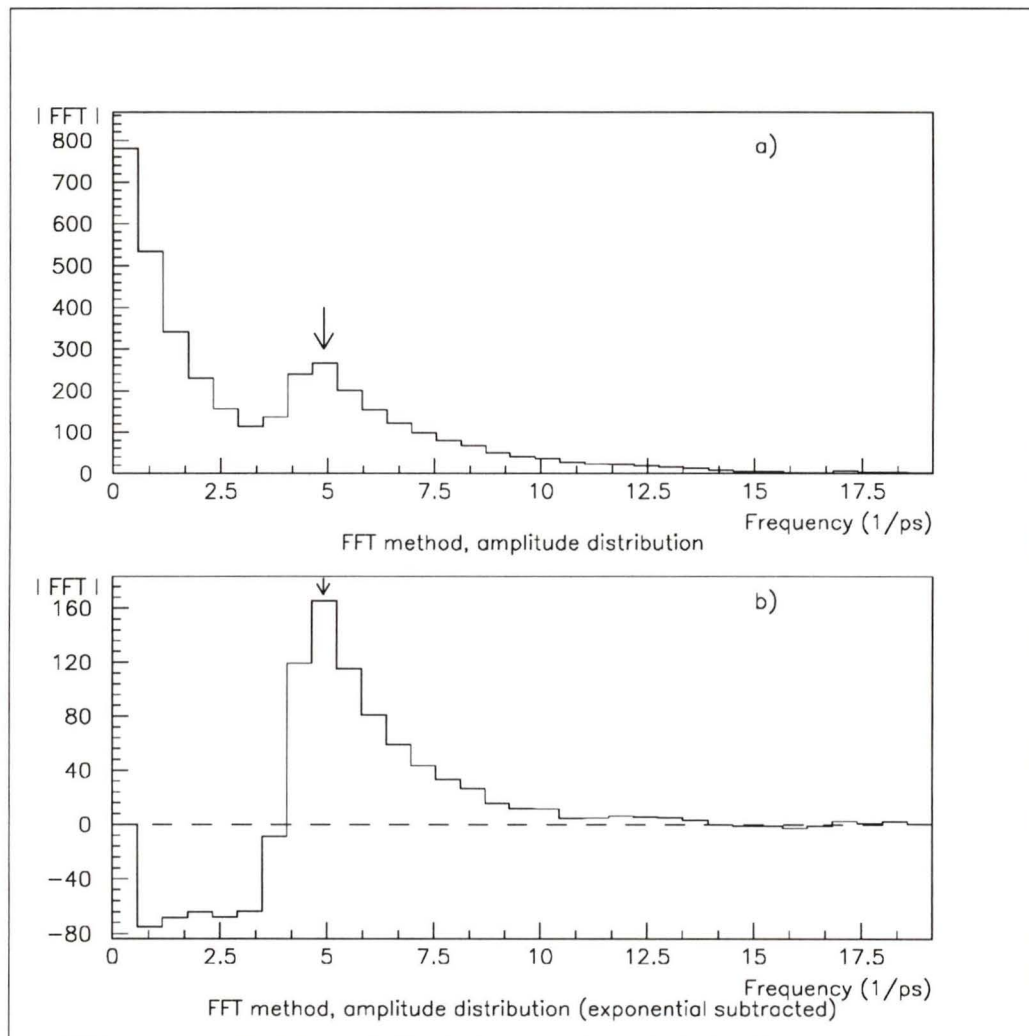


Figure 5.8: a) Amplitude distribution from an FFT applied to 50000 events binned into 0.16 ps bins for $\frac{\omega}{\tau} = 2.19 \text{ ps}^{-1}$, $\sigma = 0.13 \text{ ps}$, $\tau = 1.37 \text{ ps}$, 10 percent mistagging, 10 percent background, and frequency bin size of 0.6 ps^{-1} . The arrow shows the peak frequency at 2.32 ps^{-1} . b) Amplitude distribution from an FFT applied to 50000 events with the exponential term subtracted and binned into 0.16 ps bins for $\frac{\omega}{\tau} = 2.19 \text{ ps}^{-1}$, $\sigma = 0.13 \text{ ps}$, $\tau = 1.37 \text{ ps}$, 10 percent mistagging, 10 percent background, and frequency bin size of 0.6 ps^{-1} . The arrow shows the peak frequency at 2.32 ps^{-1} .

Chapter 6

B Meson Oscillation Simulation Results

6.1 Summary of the Runs Performed

As described in chapter 5, three programs were written by the author to investigate three different methods of measuring B_s^0 meson oscillations. For each of the three programs, 100 sets of either 200, 100, 50, or 25 sample events were generated according to distribution (5.4) for various values of input $\frac{\omega}{\tau}$, percentage mistagging, percentage flat background, and bin size. The aim of the programs is to see how well the frequency of oscillation of the parent distribution can be recovered.

6.2 The Fitting Method

The fitting method attempts to determine the four parameters of the theoretical function (5.20) ($\frac{\omega}{\tau}$, percentage mistagging, percentage background, and an overall normalization) by selecting 200, 100, 50, or 25 sample events generated from distribution (5.4) and fitting these sample events with the theoretical function. Repeating the selection of sample events 100 times results in 100 sets of four parameters estimated from the data. The reconstructed parameter $\frac{\omega}{\tau}$ was histogrammed for all 100

sets in order to reveal the distribution of reconstructed $\frac{\omega}{\tau}$. Figure 6.1a shows a typical distribution of reconstructed $\frac{\omega}{\tau}$ for an input $\frac{\omega}{\tau} = 0.73 \text{ ps}^{-1}$. This distribution shows a Gaussian-like structure with non-Gaussian tails. The appearance of this distribution will vary with different values of input parameters and different number of events used. For a high number of events and a low input $\frac{\omega}{\tau}$, the distribution resembles a Gaussian distribution (see figure 6.1b) while for low number of events and high input $\frac{\omega}{\tau}$, the distribution may show a large spread in the reconstructed values of $\frac{\omega}{\tau}$ (see figure 6.1c).

The reconstructed value of ω/τ has very little dependence on the other two parameters of distribution (5.4) (the mistagging and the background). The fitting method was repeated 100 times on sets of 200 events generated from (5.4) with the following input parameters: $\omega/\tau = 3.65 \text{ ps}^{-1}$, 0.2 ps bin size, 10 percent mistagging and 10 percent background. The resulting ω/τ distribution from the 100 fits are shown in figure 6.2. They have a mean of 3.67 ps^{-1} and a standard deviation from the mean (SD) of 0.29 ps^{-1} . The run was repeated with the same data except that in the fit the mistagging and the background were fixed to a value of 0.0. Figure 6.3 shows the results from these fits where now the data have a mean of 3.66 ps^{-1} and an SD of 0.05 ps^{-1} . A comparison of these two figures shows the means are approximately the same and therefore changing the mistag and background parameters is a small effect. However, including the other parameters in the fit increases the standard deviation of the output ω/τ distribution.

The values of ω/τ calculated by MINUIT were entered into a histogram for each run. The mean and standard deviation of the data were calculated using the actual entered values. The distribution of the reconstructed $\frac{\omega}{\tau}$ was visually inspected for evidence of a peak structure for each run. Some distributions had no clear peak. When a candidate peak structure was identified, the number of the histogram bin

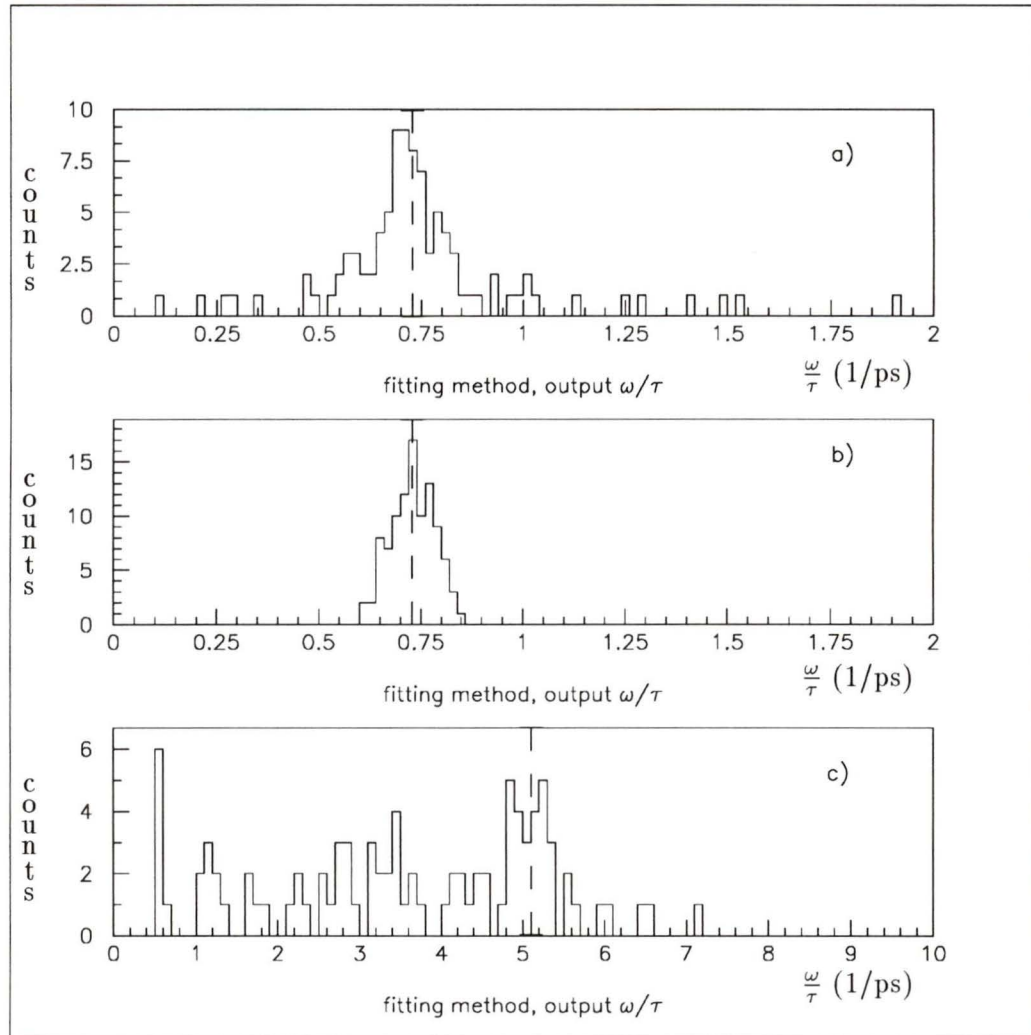


Figure 6.1: a) A typical output frequency distribution for the fitting Monte Carlo with input $\frac{\omega}{\tau} = 0.73 \text{ ps}^{-1}$ and where 100 sets of 25 sample events were used. b) A low frequency (input $\frac{\omega}{\tau} = 0.73 \text{ ps}^{-1}$) and high number of events (100 sets of 200 sample events) distribution. c) A high frequency (input $\frac{\omega}{\tau} = 5.11 \text{ ps}^{-1}$) and low number of events (100 sets of 25 sample events) distribution. The dashed lines indicate the value of the input ω/τ .

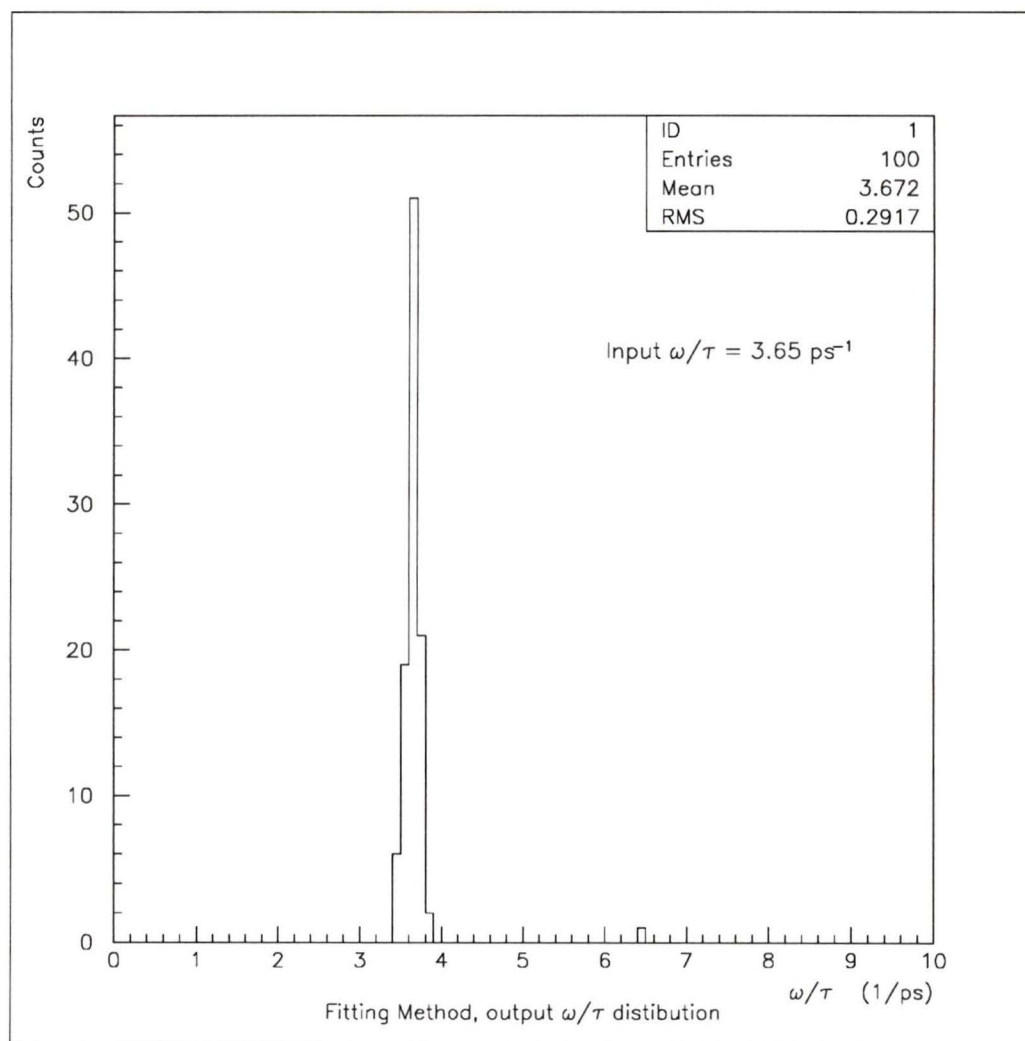


Figure 6.2: The fitted ω/τ distribution from the fitting method performed on 100 sets of 200 sample events generated with the parent parameters: $\omega/\tau = 3.65 \text{ ps}^{-1}$, 0.2 ps bin size, 10 percent mistagging and 10 percent background. The mean of this distribution is 3.67 ps^{-1} with an SD of 0.29 ps^{-1} .

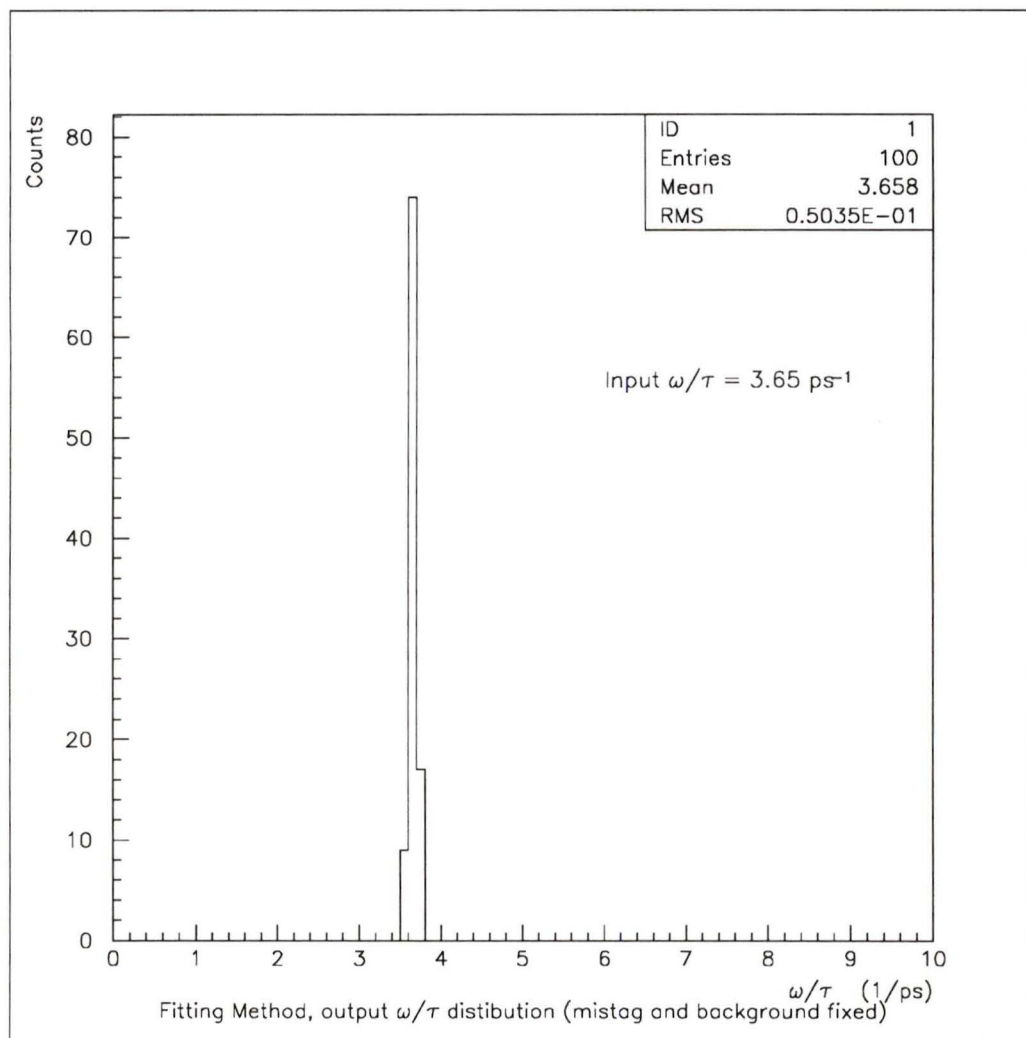


Figure 6.3: The fitted ω/τ distribution from the fitting method performed on 100 sets of 200 sample events generated with the parent parameters: $\omega/\tau = 3.65 \text{ ps}^{-1}$, 0.2 ps bin size, 10 percent mistagging and 10 percent background. The fit was performed with the mistagging and background fixed at zero. The mean of this distribution is 3.66 ps^{-1} with an SD of 0.05 ps^{-1} .

containing the maximum value was recorded as well as its full width at half maximum (FWHM). For a Gaussian distribution, the FWHM is equal to 2.36σ . However, the visual inspection can give the peak value but not easily the mean value. Statistical fluctuations of the bin contents near the mean affect the peak value. The following iteration scheme was used to determine the mean value assuming a Gaussian-like distribution.

1. The peak value and the σ estimated by visual inspection of the reconstructed $\frac{\omega}{\tau}$ distributions (see figure 6.4a), were used to define a subset of the data consisting of values of ω/τ within $\pm 3\sigma$ of the estimated most probable value. The CERN MINUIT package [34] was used to fit this subset of data with a Gaussian distribution (see figure 6.4b). (The region $\pm 3\sigma$ of the peak was chosen because for a true Gaussian distribution, it encompasses 99.7 percent of the area of a Gaussian.) All events outside of the $\pm 3\sigma$ region were ignored in the fit. This Gaussian fit provided an improved mean and σ , denoted σ_1 , for the distribution.
2. A final iteration was performed. Another Gaussian fit was made with sample events within $\pm 3\sigma_1$ of the mean found in the previous fit (see figure 6.4c). This fit gives the corrected mean and the σ , denoted σ_2 , of the distribution. As well, the percentage of the 100 runs which yielded a value of ω/τ inside the $\pm 3\sigma_2$ range was recorded.

This iterative procedure was used for sample events created from the different parent parameters stated in table 6.1. In section 6.2.1, the mean and standard deviation of the entire reconstructed $\frac{\omega}{\tau}$ distributions will be compared with the mean and sigma found from the Gaussian structures of the reconstructed $\frac{\omega}{\tau}$ distributions. Appendix B gives the results of the final iteration of the Gaussian fit and the mean

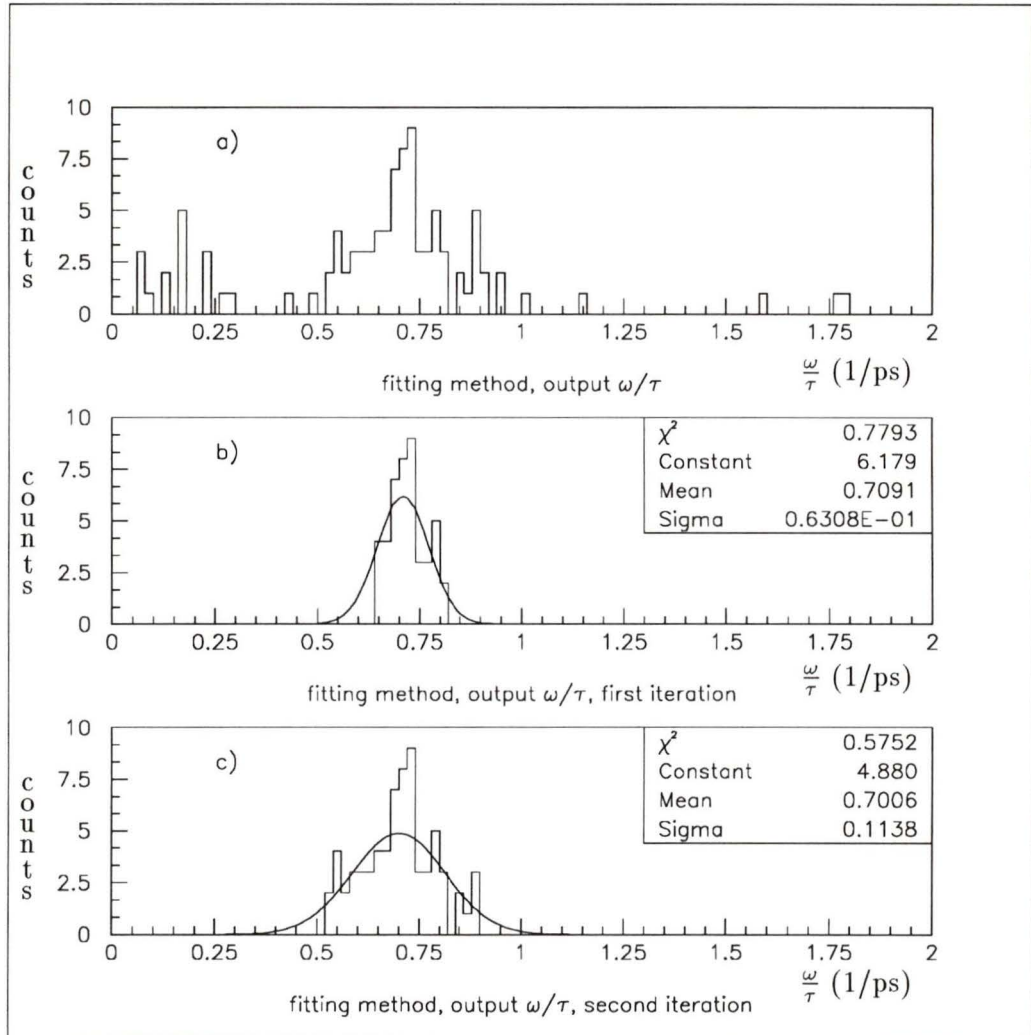


Figure 6.4: a) An output frequency distribution for the fitting program with input $\frac{\omega}{\tau} = 0.73 \text{ ps}^{-1}$ and 100 sets of 100 sample events were used. b) The same distribution after the first iteration of the Gaussian fit. c) The same distribution after the second iteration of the Gaussian fit. The fit results with the χ^2 per degree of freedom of the fits are shown in the boxes.

<i>The Fitting Method</i>					
Run	# of events/set	input $\frac{\omega}{\tau}$ (ps ⁻¹)	bin size (ps)	mistag	bkg
1	200, 100, 50, 25	0.73, 2.19, 3.65, 5.11, 6.57	0.2	0.1	0.1
2	200, 100, 50, 25	0.73, 2.19, 3.65, 5.11, 6.57	0.1	0.1	0.1
3	200, 100, 50, 25	0.73, 2.19, 3.65, 5.11, 6.57	0.2	0.2	0.1
4	200, 100, 50, 25	0.73, 2.19, 3.65, 5.11, 6.57	0.2	0.1	0.2

Table 6.1: Table of runs performed with the fitting program.

and standard deviation of all of the reconstructed $\frac{\omega}{\tau}$ distributions.

6.2.1 The Results of the Fitting Method

The mean and standard deviation of the reconstructed $\frac{\omega}{\tau}$ distributions for the runs listed in table 6.1 were found and the results are given in Appendix B. One hundred sets of 200, 100, 50, or 25 sample events were generated according to distribution (5.4) with a parent parameter $\frac{\omega}{\tau} = 0.73, 2.19, 3.65, 5.11, \text{ and } 6.57 \text{ ps}^{-1}$. It should be noted that the variation in the parameters in runs 1 through 4 (bin size, percentage mistagging, and percentage flat background) represents a possible range which may be encountered in an experiment on B_s^0 oscillations. Plots made showing the behavior of the mean and standard deviation as a function of the various input parameters are presented in this section.

Figure 6.5 shows the absolute value of the percentage difference of the mean of the output $\frac{\omega}{\tau}$ distribution from the input $\frac{\omega}{\tau}$ ($\frac{\omega}{\tau} = 2.19 \text{ ps}^{-1}$ in figure 6.5) as the number of sample events per set, N , increases from $N = 25$ to 200 events for all four runs. This figure clearly shows the convergence of the percentage difference to zero as N increases. From the high statistics run performed in chapter 5, this percentage difference indeed converges to zero as N becomes very large. The signed difference between the mean value of the output $\frac{\omega}{\tau}$ and the input $\frac{\omega}{\tau}$ was examined

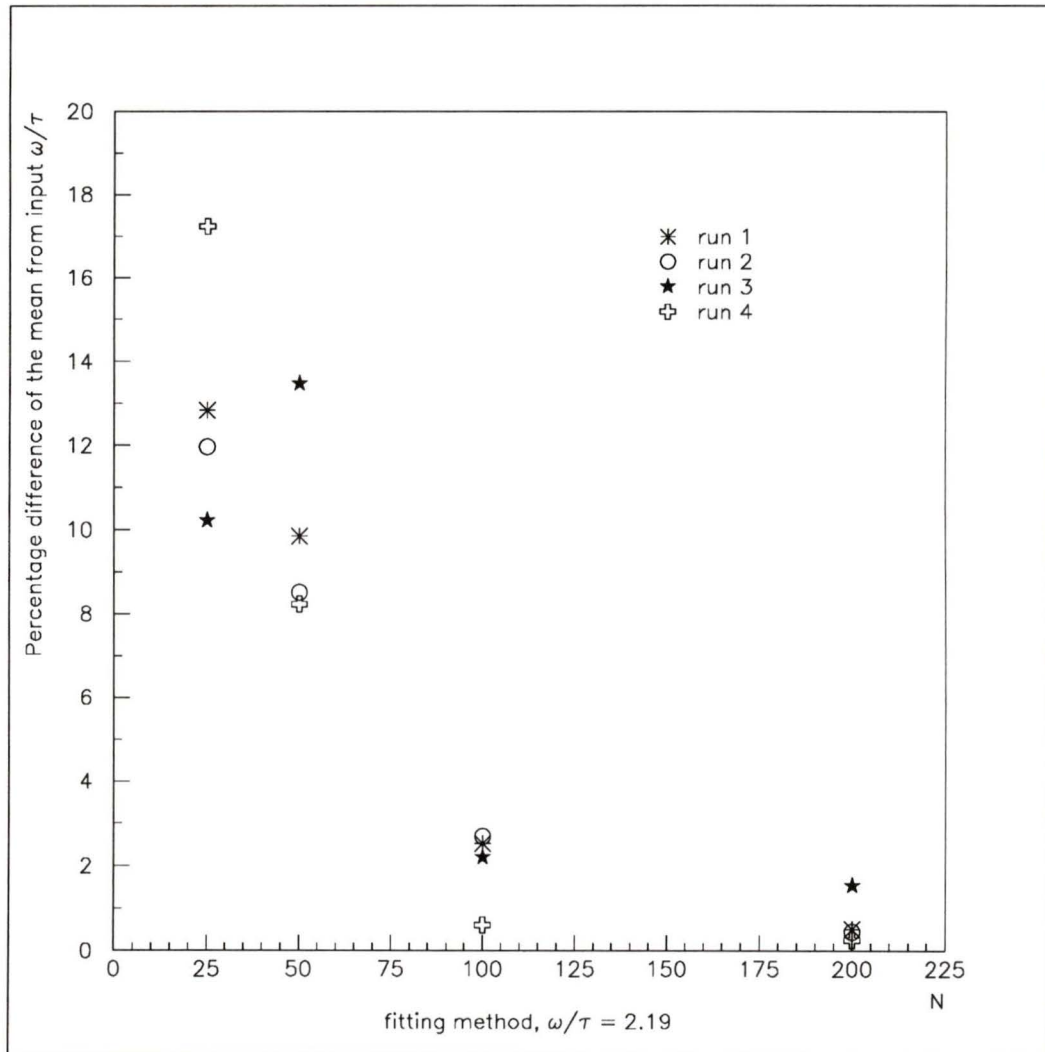


Figure 6.5: Fitting method plot of the absolute percentage difference of the mean of the output ω/τ distribution from the input ω/τ versus N for an input $\omega/\tau = 2.19 \text{ ps}^{-1}$. The plot converges to zero at large N .

for any evidence of systematic shifts. Recovered values of $\frac{\omega}{\tau}$ within $\pm 1.0 \text{ ps}^{-1}$ were symmetrically distributed. More poorly recovered values had a tendency of being too large.

Figure 6.6 is a plot of $\frac{SD}{\sqrt{N}}$ versus N with an input $\frac{\omega}{\tau} = 2.19 \text{ ps}^{-1}$ for all four runs where the SD is the standard deviation from the mean of the reconstructed $\frac{\omega}{\tau}$ distribution. As expected, the values of SD of reconstructed $\frac{\omega}{\tau}$ distributions increase as the number of events per set decreases. Some differences between the four runs become apparent in this figure. Run 3 (20 percent mistagging) appears to have consistently larger SD for all values of N . The values of SD for run 1 appear to be slightly higher than run 2 (0.1 ps bin size) for low N . Increasing the percentage of background (run 4) does not appear to have any significant impact on the values of SD as compared to the other runs. The high statistics run from chapter 5 confirms the fact that the $\frac{SD}{\sqrt{N}}$ approaches zero for $N \geq 200$ in figure 6.6 while the $\frac{SD}{\sqrt{N}}$ is an increasing function for low statistics. The SD of the high statistics run ($N = 10000$) is 0.009. The SD = 0.057 for 200 events with the same input frequency, mistagging, background, and binning. The ratio of SD(10000) to SD(200) is 6.33 while the ratio of the statistics $\sqrt{10000}$ to $\sqrt{200}$ is 7.07. This is evidence that for 200 events or more, the errors scale with the statistics. The same calculation using the SD determined for 100 events gives a ratio that is different from statistical scaling by about 400 percent. Therefore, one might expect that 200 events will be near the minimum number needed to successfully recover the input ω/τ of the distribution.

Since runs 1 through 4 represent the range of parameters (bin size, percentage of mistagging, and percentage of flat background) which may be encountered in a B_s^0 oscillation experiment, averaging a result over the four runs gives a number whose error represents an uncertainty within the limits of the model. In figure 6.7, the percentage difference of the mean from the input ω/τ (for input $\omega/\tau = 0.73, 2.19,$

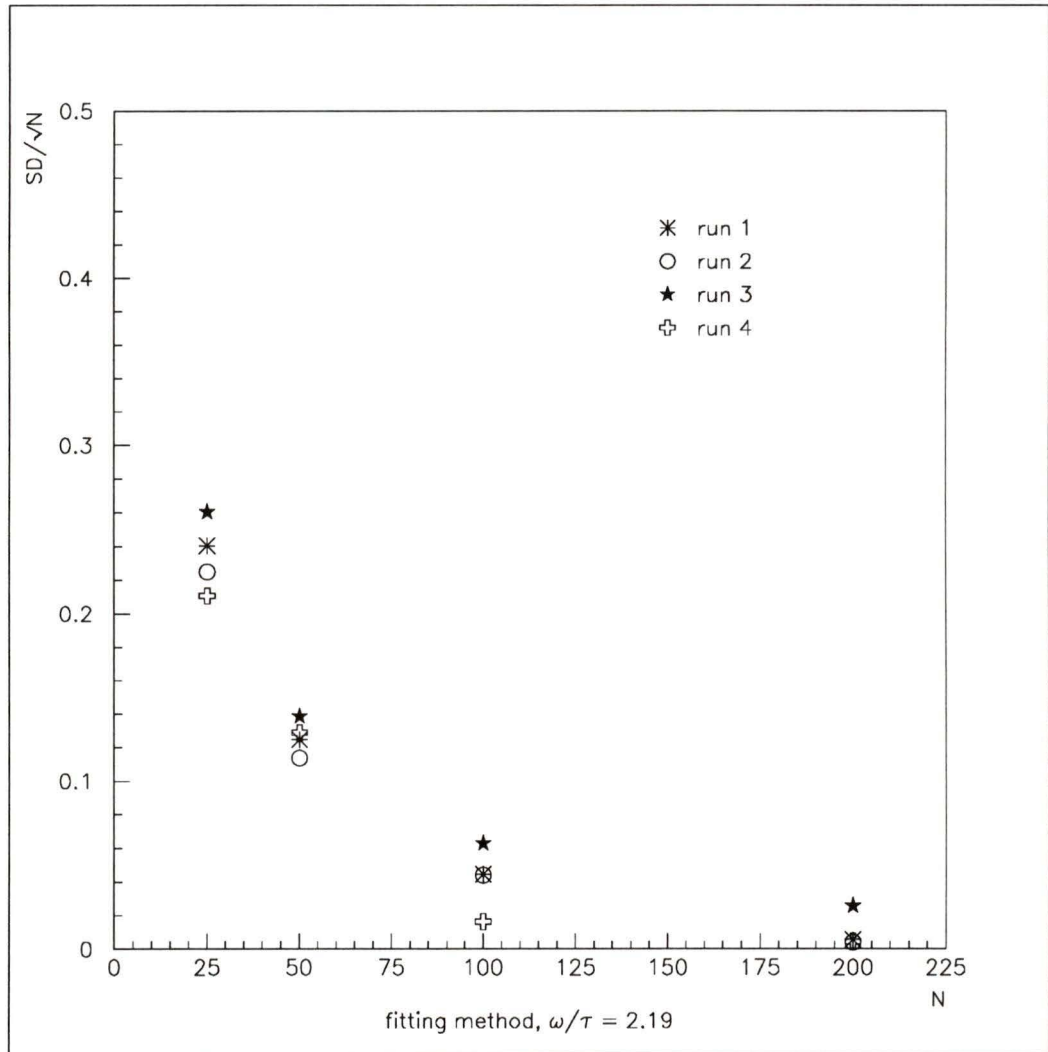


Figure 6.6: Fitting method plot of SD/\sqrt{N} versus N of the output ω/τ distribution for an input $\omega/\tau = 2.19 \text{ ps}^{-1}$. The plot converges to zero for large N and is an increasing function at small N .

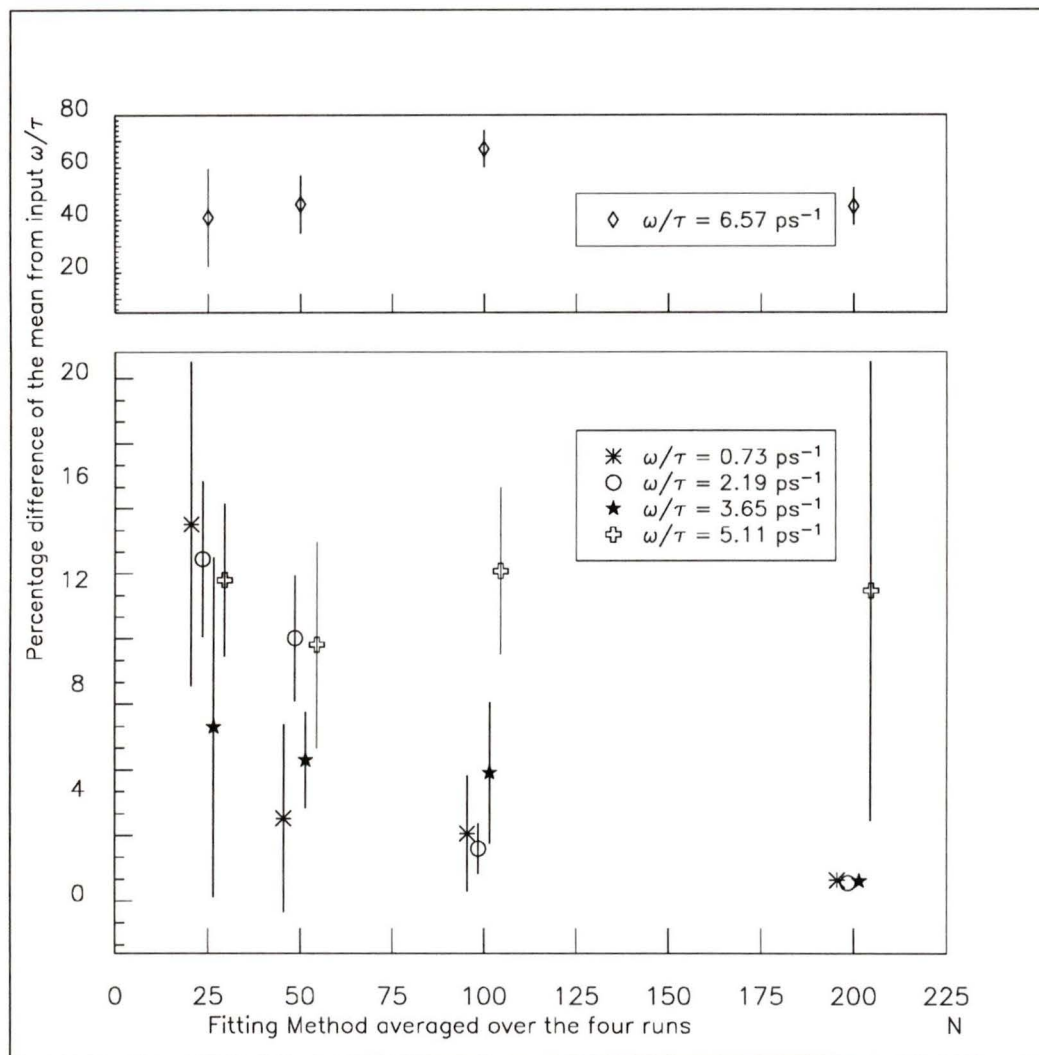


Figure 6.7: Fitting method plot of the absolute percentage difference of the mean of the output ω/τ distribution from the input ω/τ averaged over the four runs versus N . Data at $N = 25, 50, 100$, and 200 have been slightly offset for clarity. Note that there is a change in scale for the y-axis of the upper plot. The three data points at $N = 200$ have error bars which are too small to be displayed. Note that the y-axis starts at -2 percent.

3.65, 5.11, and 6.57 ps⁻¹) is averaged over the four runs and is plotted with its errors (the standard deviation about the mean) versus the number of events (N) per set. This percent difference for all N is less than 20 percent for $\omega/\tau = 0.73, 2.19, 3.65,$ and 5.11 ps⁻¹. The value of $\omega/\tau = 5.11$ ps⁻¹ appears to indicate the limit of this fitting method due to low statistics since $\omega/\tau = 6.57$ ps⁻¹ gives percent differences of 30 to 75 percent.

In figure 6.8, the value of $\frac{SD}{\sqrt{N}}$ determined for each input $\frac{\omega}{\tau}$ is averaged over the four runs for all values of N. The increase in the values of SD with increasing input $\frac{\omega}{\tau}$ is very apparent with the $\frac{SD}{\sqrt{N}}$ value converging to zero at high N. As was seen in figure 6.6, the values of SD also increase as N decreases.

As was stated at the beginning of this chapter, all reconstructed $\frac{\omega}{\tau}$ distributions from the fitting program were visually inspected for a Gaussian-like structure and then fitted to get the mean, σ , and the percentage of runs within $\pm 3\sigma$. A comparison of the Gaussian mean and σ with the mean and standard deviation of these distributions is used to estimate the likelihood of the reconstructed $\frac{\omega}{\tau}$ distribution being well described by a Gaussian. The percentage of runs which yield results within $\pm 3\sigma$ of the mean was used as a definition of the stability of the fit. If the distributions were perfectly Gaussian, then 99.7 percent of the events would be within $\pm 3\sigma$ of the mean. A distribution was considered as reasonably Gaussian if 90 percent of the events fall within this $\pm 3\sigma$ range.

Figure 6.9 shows the percentage of events within $\pm 3\sigma$ versus N for an input $\frac{\omega}{\tau} = 2.19$ ps⁻¹ for all four runs. Increasing the percentage mistagging appears to affect the output $\frac{\omega}{\tau}$ distribution since run 3 seems to have consistently less number of entries within $\pm 3\sigma$ than the other runs. This figure shows that for an input $\frac{\omega}{\tau} = 2.19$ ps⁻¹, N = 100 events are required in order to have a 90 percent probability that a measurement of $\frac{\omega}{\tau}$ will be within $\pm 3\sigma$ of the mean of the distribution. Table 6.2

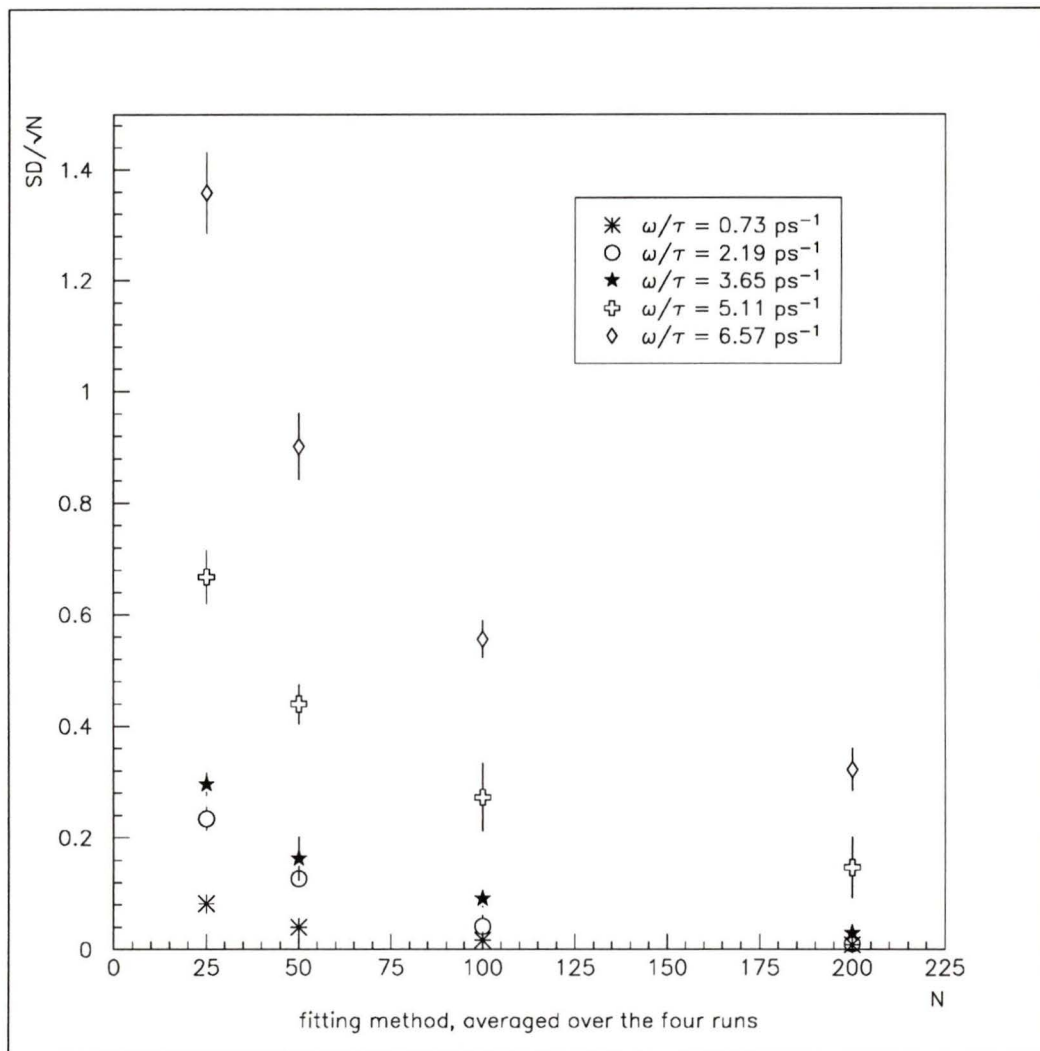


Figure 6.8: Fitting method plot of SD/\sqrt{N} of the output ω/τ distribution averaged over the four runs versus N .

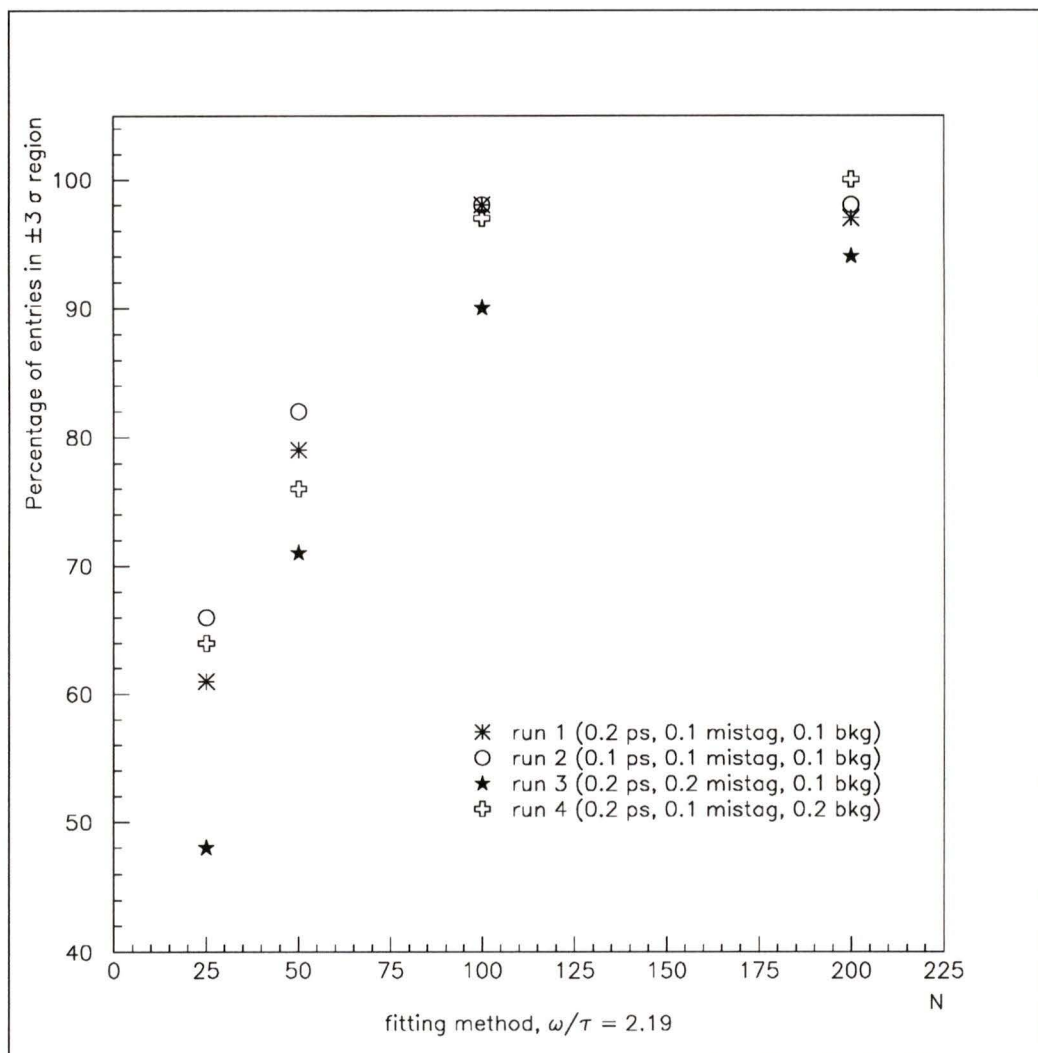


Figure 6.9: Fitting method plot of the percentage of entries within the $\pm 3\sigma$ region of the output ω/τ distribution versus N for an input $\omega/\tau = 2.19 \text{ ps}^{-1}$. Note that the y-axis starts at 40 percent.

gives a list of the runs which had 90 percent of events within $\pm 3\sigma$ for the different values of N and input ω/τ . The mean and σ of the Gaussian were compared with with the mean and standard deviation of the full distributions. Some of the SD are considerably larger than the corresponding σ of the Gaussian fit. These larger values of SD are due to a few points in the output ω/τ distribution which are far away from the $\pm 3\sigma$ region.

The analysis supports the following conclusions:

- It appears that the reconstructed $\frac{\omega}{\tau}$ distribution is approximately Gaussian for $\omega/\tau = 0.73 \text{ ps}^{-1}$ and $N = 50, 100, \text{ and } 200$, for $\omega/\tau = 2.19 \text{ ps}^{-1}$ and $N = 100$ and 200 , and for $\omega/\tau = 3.65 \text{ ps}^{-1}$ and $N = 200$.
- Changing the percentage mistagging (run 3) appears to have a bigger effect on the reconstructed $\frac{\omega}{\tau}$ distributions compared with changing the background. Increasing the percentage mistagging increases the values of SD of the distributions and reduces the Gaussian nature of the reconstructed $\frac{\omega}{\tau}$ distributions.
- Increasing the percentage flat background has little effect on the features of the reconstructed $\frac{\omega}{\tau}$ distributions including the likelihood of the distribution being described by a Gaussian.
- Decreasing the bin size (run 2) has a small effect on the distributions. Figure 6.9 shows that a reconstructed $\frac{\omega}{\tau}$ distribution from a smaller bin size has consistently slightly more events within the $\pm 3\sigma$ range. As well, figure 6.6 shows that run 2 has smaller values of SD than run 1.
- The $\frac{SD}{\sqrt{N}}$ values, when averaged over the four runs, show systematic differences. The values of SD/\sqrt{N} increase as the values of input $\frac{\omega}{\tau}$ increase for a fixed N . The SD scale with statistics for 200 events or more.

Run	ω	$\frac{\omega}{\tau}$	N	<i>Gaussian fit</i>					% in $\pm 3\sigma$
				mean	error on mean	σ	mean	SD	
1	1	0.73	200	0.73	0.01	0.05	0.73	0.05	100
			100	0.73	0.01	0.06	0.72	0.09	97
			50	0.72	0.02	0.11	0.72	0.20	90
	3	2.19	200	2.18	0.01	0.06	2.18	0.08	97
			100	2.19	0.01	0.08	2.24	0.44	98
	5	3.65	200	3.65	0.01	0.07	3.67	0.29	97
2	1	0.73	200	0.73	0.01	0.05	0.73	0.05	100
			50	0.73	0.02	0.12	0.71	0.20	92
	3	2.19	200	2.18	0.01	0.05	2.18	0.06	98
			100	2.18	0.01	0.08	2.25	0.44	98
	5	3.54	200	3.65	0.01	0.07	3.69	0.45	97
3	3	2.19	200	2.19	0.01	0.08	2.22	0.36	94
			100	2.18	0.01	0.11	2.49	0.98	90
4	1	0.73	200	0.74	0.01	0.07	0.73	0.07	100
			100	0.74	0.01	0.08	0.73	0.13	97
			50	0.78	0.03	0.19	0.79	0.33	91
	3	2.19	200	2.18	0.01	0.07	2.18	0.07	100
			100	2.19	0.01	0.09	2.20	0.16	97
	5	3.65	200	3.62	0.01	0.10	3.67	0.27	97

Table 6.2: Table of fitting method runs which have 90 percent of events within $\pm 3\sigma$. This table compares the mean, the error on the mean found by the fitting procedure, and the σ of the Gaussian fit with the mean and and the SD of the entire reconstructed ω/τ distribution.

6.3 The Folding Method

The folding program was used to analyze a set of 200, 100, 50, or 25 sample events generated according to distribution (5.4) in an attempt to reconstruct the frequency of the parent distribution. The analysis was repeated 100 times on 100 sample distributions to produce 100 estimates of the period x_{int} . Each period was converted to a frequency via the relation $\text{frequency} = \frac{\pi}{x_{int}}$ and then entered into a histogram. The histograms for various sets of input parent parameters are very much like those of figures 6.1 found for the fitting method. They exhibit the same features at high and low input $\frac{\omega}{\tau}$ and at high and low numbers of events (see figure 6.10a, b, c). It should be noted that the fitting and folding methods can yield different results. The fitting method extracts the frequency of the sinusoidal term used to generate the time distribution of B_s^0 oscillation, while the folding method will simply reveal a periodicity in the distribution if one exists.

The procedure described in section 6.2 for the fitting method was also used to calculate the mean and the standard deviation of the entire folding frequency distributions. All folding frequency histograms were visually inspected for a candidate peak and the FWHM was determined (and hence σ for a Gaussian structure). A Gaussian fit was made including only events within $\pm 3\sigma$ of the peak to get a new estimate of the mean and the width, denoted σ_1 , of each distribution. A second Gaussian fit was made to the sample events within $\pm 3\sigma_1$ of the new mean to get a corrected mean and σ_2 , as well as and the errors on the fitting parameters for all of the folding frequency distributions. The percentage of all events within $\pm 3\sigma_2$, the mean, σ_2 , and errors are recorded in Appendix B along with the mean and SD of the full histogram. The list of parent parameters used to generate the distributions is given in table 6.3. The mean and SD of the folding frequency distributions will

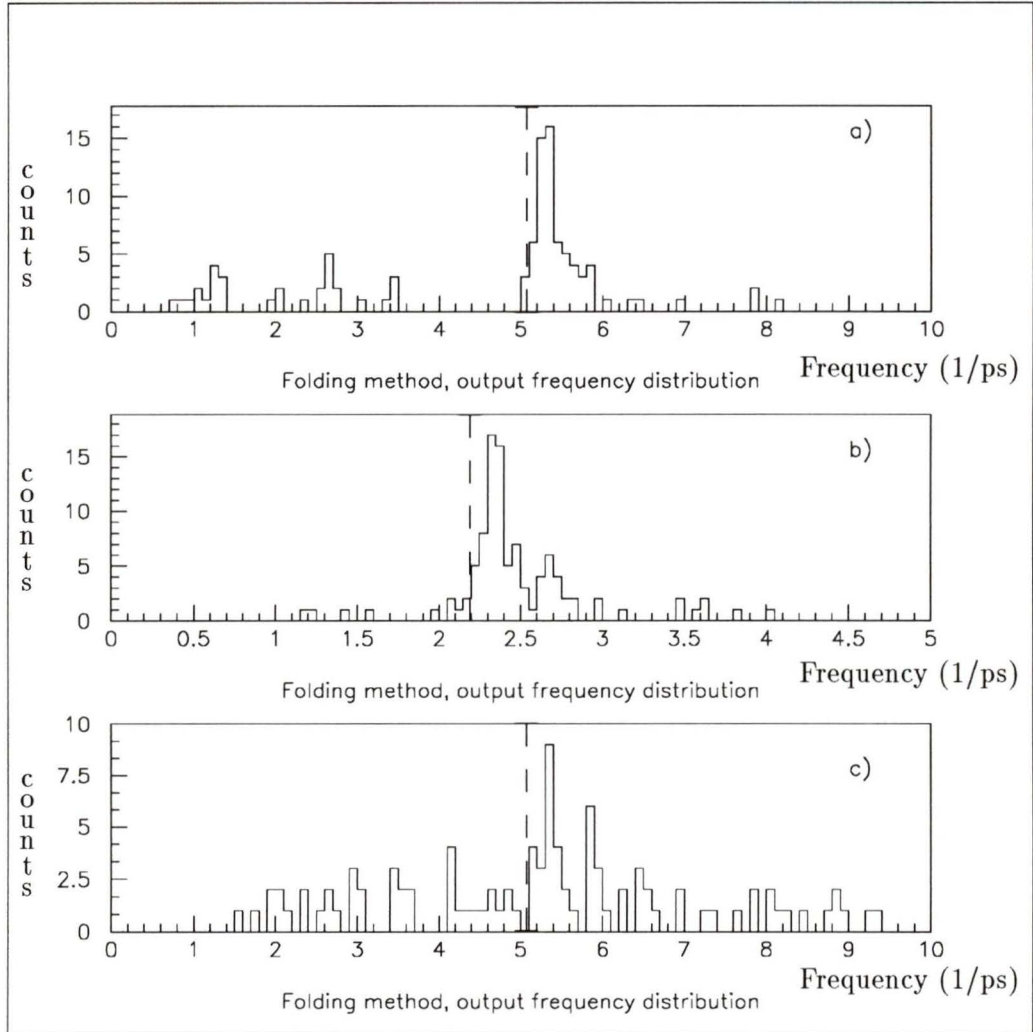


Figure 6.10: a) A typical output frequency distribution for the folding method with input $\frac{\omega}{\tau} = 5.11 \text{ ps}^{-1}$ and 100 sets of 200 sample events were used. b) A low frequency (input $\frac{\omega}{\tau} = 2.19 \text{ ps}^{-1}$) and high number of events (100 sets of 200 sample events) distribution. c) A high frequency (input $\frac{\omega}{\tau} = 5.11 \text{ ps}^{-1}$) and low number of events (100 sets of 25 sample events) distribution. The dashed lines indicate the value of the input ω/τ .

<i>The Folding Method</i>				
Run	# of events/set	input $\frac{\omega}{\tau}$ (ps ⁻¹)	mistag	bkg
1	200, 100, 50, 25	0.73, 2.19, 3.65, 5.11, 6.57	0.1	0.1
2	200, 100, 50, 25	0.73, 2.19, 3.65, 5.11, 6.57	0.2	0.1
3	200, 100, 50, 25	0.73, 2.19, 3.65, 5.11, 6.57	0.1	0.2

Table 6.3: *Table of runs performed with the folding program.*

be compared in section 6.3.1 to the mean and sigma found from the Gaussian fits.

6.3.1 The Results of the Folding Method

Table 6.3 shows the runs for which the mean and SD of the output folding frequency distributions were calculated in an attempt to reconstruct the frequency of the parent distribution. One hundred sets of 200, 100, 50, or 25 sample events were generated from distribution (5.4) with a parent parameter $\omega/\tau = 0.73, 2.19, 3.65, 5.11,$ and 6.57 ps^{-1} . Plots of the mean and SD of the folding frequency distributions were made for the various values of the parameters.

Figure 6.11 shows a plot of the absolute value of the percentage difference between the mean of the folding frequency distributions and the input $\frac{\omega}{\tau}$ versus the number of events (N) in each of the 100 sets. The trend, an increasing percentage difference as N decreases, seen in the fitting method reappears in the folding method. However, the percentage difference appears to be converging at about 12 percent as N becomes large. Since there exists a finite time bin size, x_{bin} , used by the folding method, the actual value of the folding frequency must lie in the range $\frac{\pi}{x_{int}}$ to $\frac{\pi}{x_{int}-x_{bin}}$ because x_{int} represents the upper edge of a bin. Hence, there is an intrinsic uncertainty due to this finite bin size in the percentage difference between the observed mean and the input $\frac{\omega}{\tau}$ of $\frac{\pi/x_{int}-\pi/(x_{int}-x_{bin})}{\pi/x_{int}} = \frac{x_{bin}}{x_{int}-x_{bin}}$. For $\frac{\omega}{\tau} = 2.19 \text{ ps}^{-1}$ and for $x_{bin} = 0.1$ to 0.2 ps , the range of uncertainty is about 8 to 16

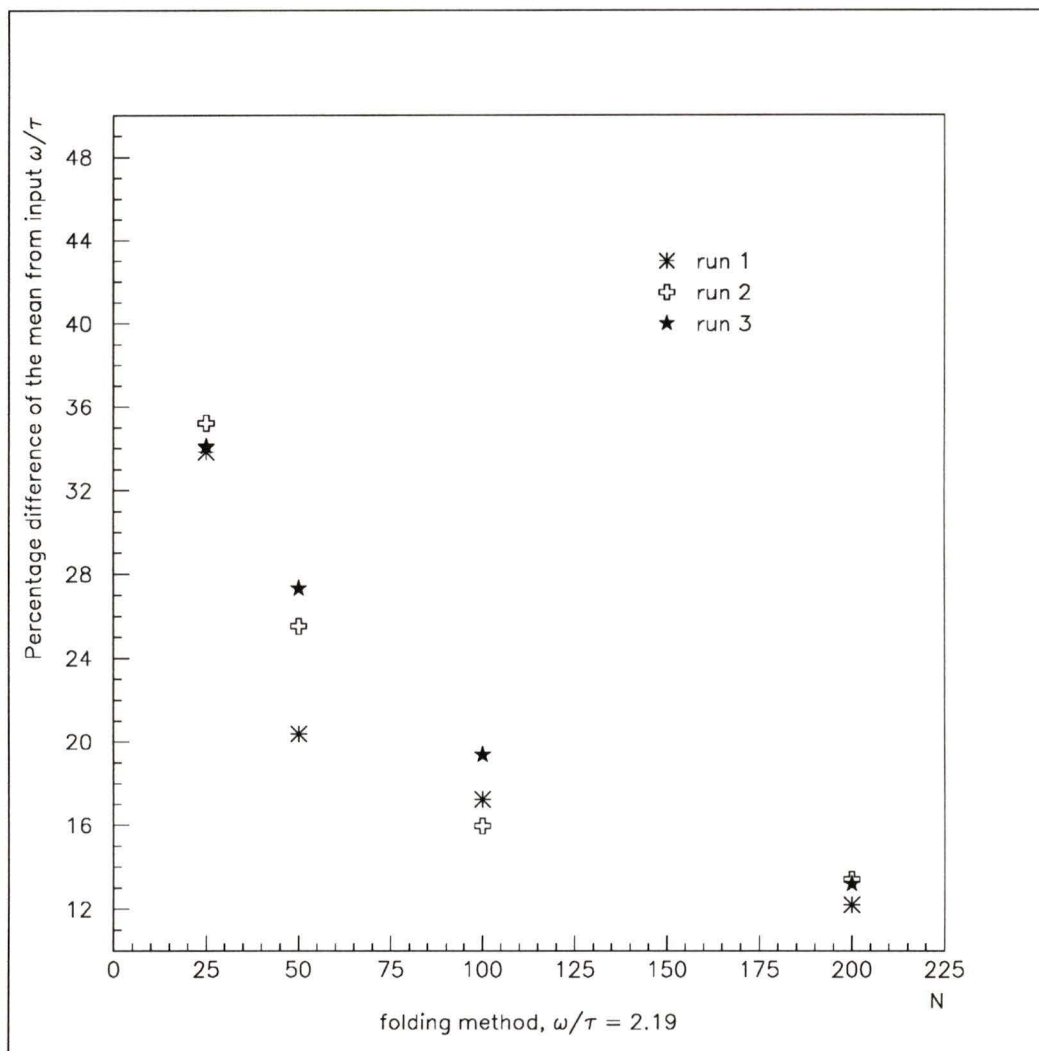


Figure 6.11: *Folding method plot of the absolute percentage difference of the mean from the input ω/τ versus N for an input $\omega/\tau = 2.19 \text{ ps}^{-1}$. Note that the y-axis starts at 10 percent. The plot converges to about 12 percent at $N = 200$.*

percent. Therefore, the percentage difference of about 12 percent seen in figure 6.11 is within the uncertainty inherent in the measurement. The percentage difference for $\frac{\omega}{\tau} \geq 2.19 \text{ ps}^{-1}$ at $N = 200$ for all of the runs falls within this uncertainty, and so any deviation of the mean from the input $\frac{\omega}{\tau}$ due to the presence of an exponential term in distribution (5.4) is hidden within this uncertainty. At $\frac{\omega}{\tau} = 0.73 \text{ ps}^{-1}$ and low N , the observed mean is 300 percent off. At larger values of period x_{int} (low $\frac{\omega}{\tau}$), the data is divided into more bins because of the upper limit on x_{bin} and therefore more statistics are required. The folding method therefore is not good for very small values of $\frac{\omega}{\tau}$. The signed difference between the mean value of the output frequency and the input $\frac{\omega}{\tau}$ was examined for evidence of any systematic effects. The distribution was symmetric around zero and about three times broader than the same distribution for the fitting method.

Figure 6.12 shows the $\frac{SD}{\sqrt{N}}$ of the folding frequency distribution versus N for all three runs as N increases from 25 to 200 events. As with the fitting method, the SD increases as N decreases. It also appears that run 2 (20 percent mistagging) has larger values of SD for smaller N than other runs while run 3 (20 percent flat background) appears to have similar values of SD to run 1 at low N .

As was done with the fitting method, the percentage difference of the mean from the input $\frac{\omega}{\tau}$ and the $\frac{SD}{\sqrt{N}}$ values were averaged over the three runs for each input value of $\frac{\omega}{\tau}$ in order to get results and errors (the standard deviations) which are representative of the variation of the parameters which may be encountered in an experiment on B_s^0 oscillations. Figure 6.13 presents the averaged percentage difference of the mean from the input $\frac{\omega}{\tau}$ over the three runs for input $\omega/\tau = 0.73, 2.19, 3.65, 5.11, \text{ and } 6.57 \text{ ps}^{-1}$. It can clearly be seen from this figure that the percentage difference for $\omega/\tau = 0.73 \text{ ps}^{-1}$ varies from 100 percent at high N to 350 percent at low N and therefore the folding method is not appropriate for low frequency. The

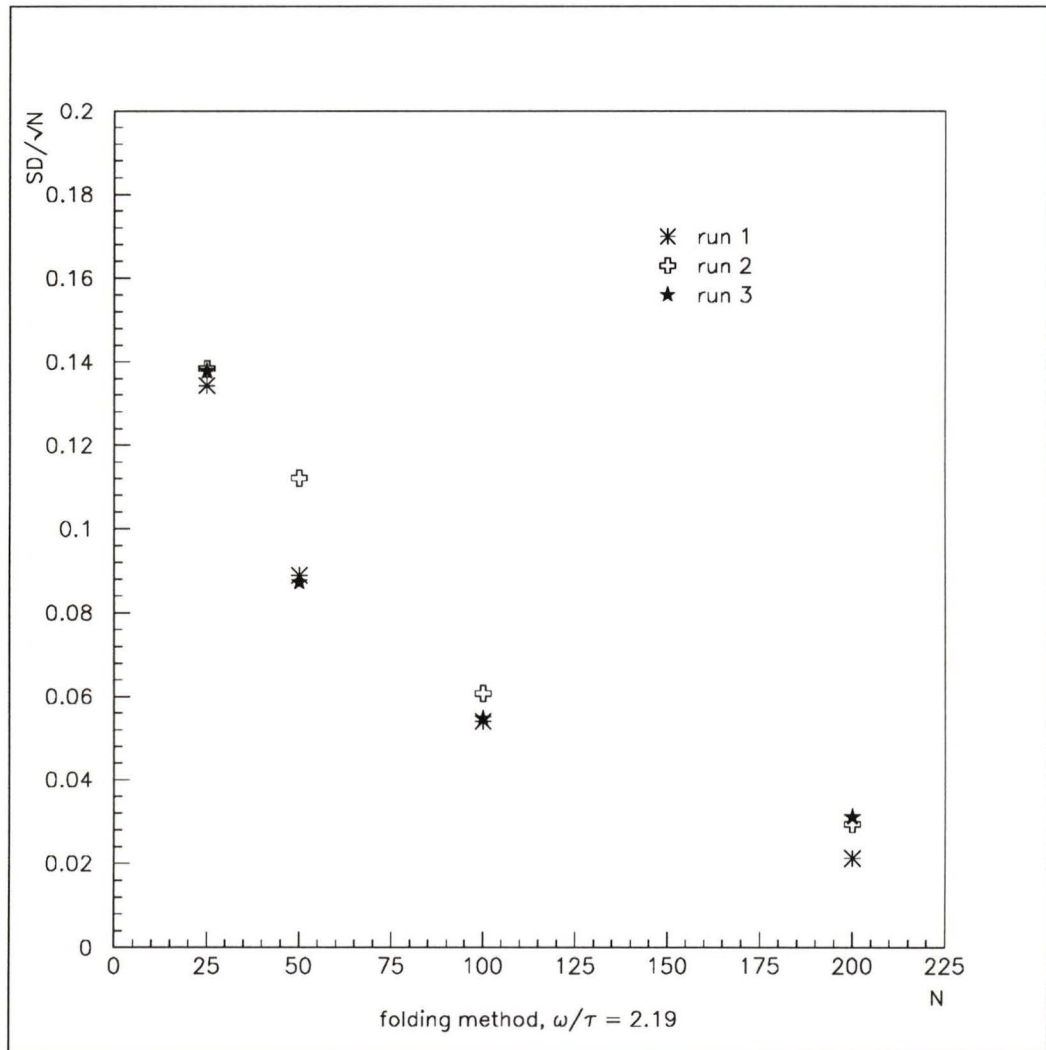


Figure 6.12: Folding method plot of SD/\sqrt{N} of the folding frequency distribution versus N for an input $\omega/\tau = 2.19 \text{ ps}^{-1}$.

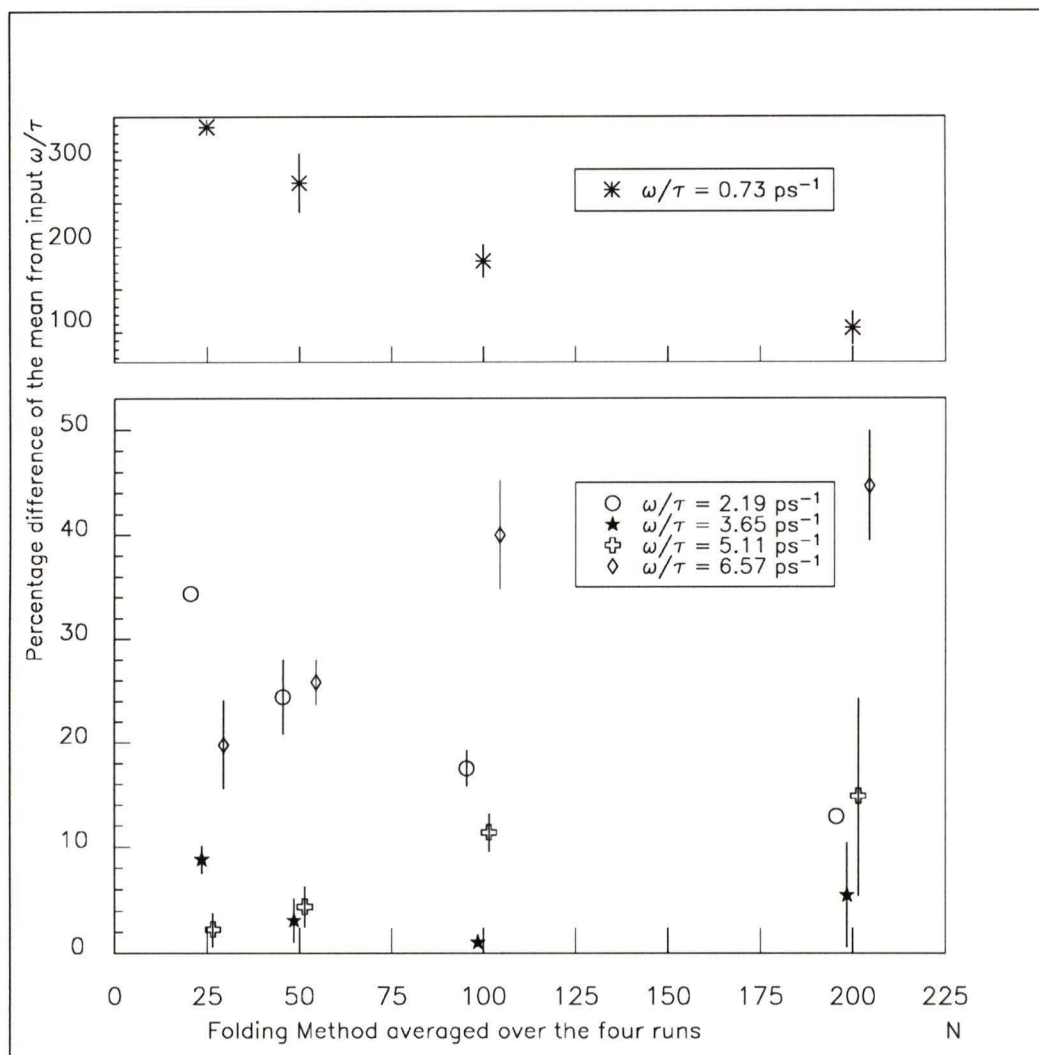


Figure 6.13: Folding method plot of the absolute percentage difference of the mean of the output frequency distribution from the input ω/τ averaged over the three runs versus N . Data at $N = 25, 50, 100$, and 200 have been slightly offset for clarity. Note that there is a change in scale for the y-axis of the upper plot.

effect can be predicted from both the effect of increasing the number of bins for longer periods and the presence of the exponential term in distribution (5.4). For all other input ω/τ , the percentage differences remain between 0 to 50 percent and are within the uncertainty due to the finite time bin width, x_{bin} . For $\omega/\tau = 2.19$ and 3.65 ps^{-1} , the percent difference increases as N decreases as expected. However, at $\omega/\tau = 5.11$ and 6.57 ps^{-1} , the percent difference increases as N increases which could reflect the fact that folding method becomes less applicable as the ω/τ value approaches the maximum value, $\omega/\tau = 7.85 \text{ ps}^{-1}$ (see section 5.4), where the folding method is no longer valid. It is likely that the folding method will jump between the fundamental and first harmonic as the period becomes close to the bin size.

Figure 6.14 shows a plot of the averaged $\frac{SD}{\sqrt{N}}$ over the three types of runs versus N . Once again, this plot shows systematic differences. The values of $\frac{SD}{\sqrt{N}}$ values increase with increasing input ω for fixed N . The SD follow the same trend of increasing with decreasing N .

The percentage of the sample runs within a $\pm 3\sigma$ window defined by the iterated Gaussian fit can again be used to give a measure of the stability of the fit. Figure 6.15 is a plot of the percentage of events within $\pm 3\sigma$ versus N for a nominal $\frac{\omega}{\tau} = 2.19 \text{ ps}^{-1}$. Only one point lies in the region where greater than 90 percent of the runs produce a results within $\pm 3\sigma$. However, from the results of all of the runs given in Appendix B, the runs that do satisfy the $\pm 3\sigma$ criterion all have large values for the Gaussian σ from the fit. There are no systematic trends evident in figure 6.15. It appears that changes in the percentage mistagging (run 2) and percentage flat background (run 3) have an insignificant effect on the output folding frequency distributions.

A few conclusions are drawn from the figures in this section:

- There is a 12 percent difference even at large N between the input $\frac{\omega}{\tau} = 2.19 \text{ ps}^{-1}$ and the folding frequency. This percentage difference is within the

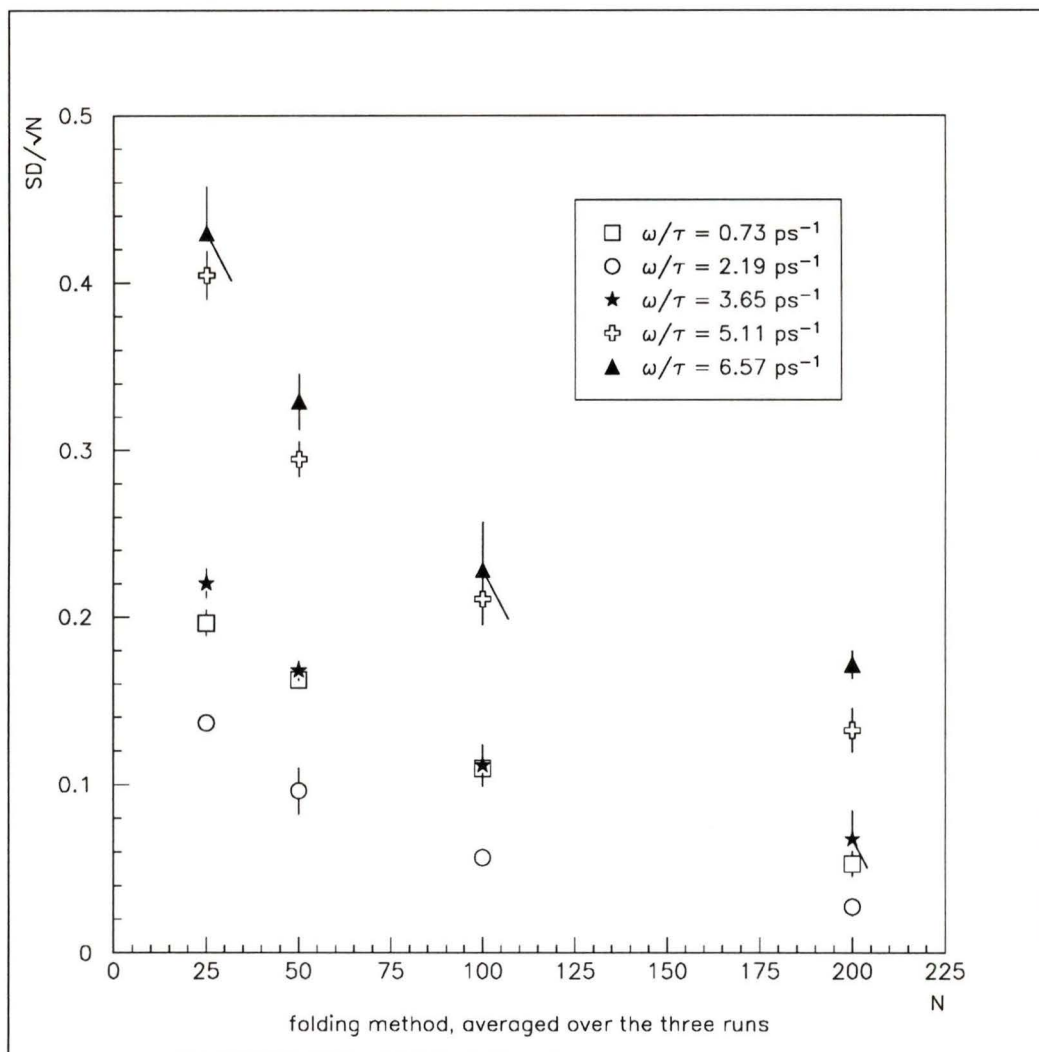


Figure 6.14: Folding method plot of SD/\sqrt{N} averaged over the three runs versus N .

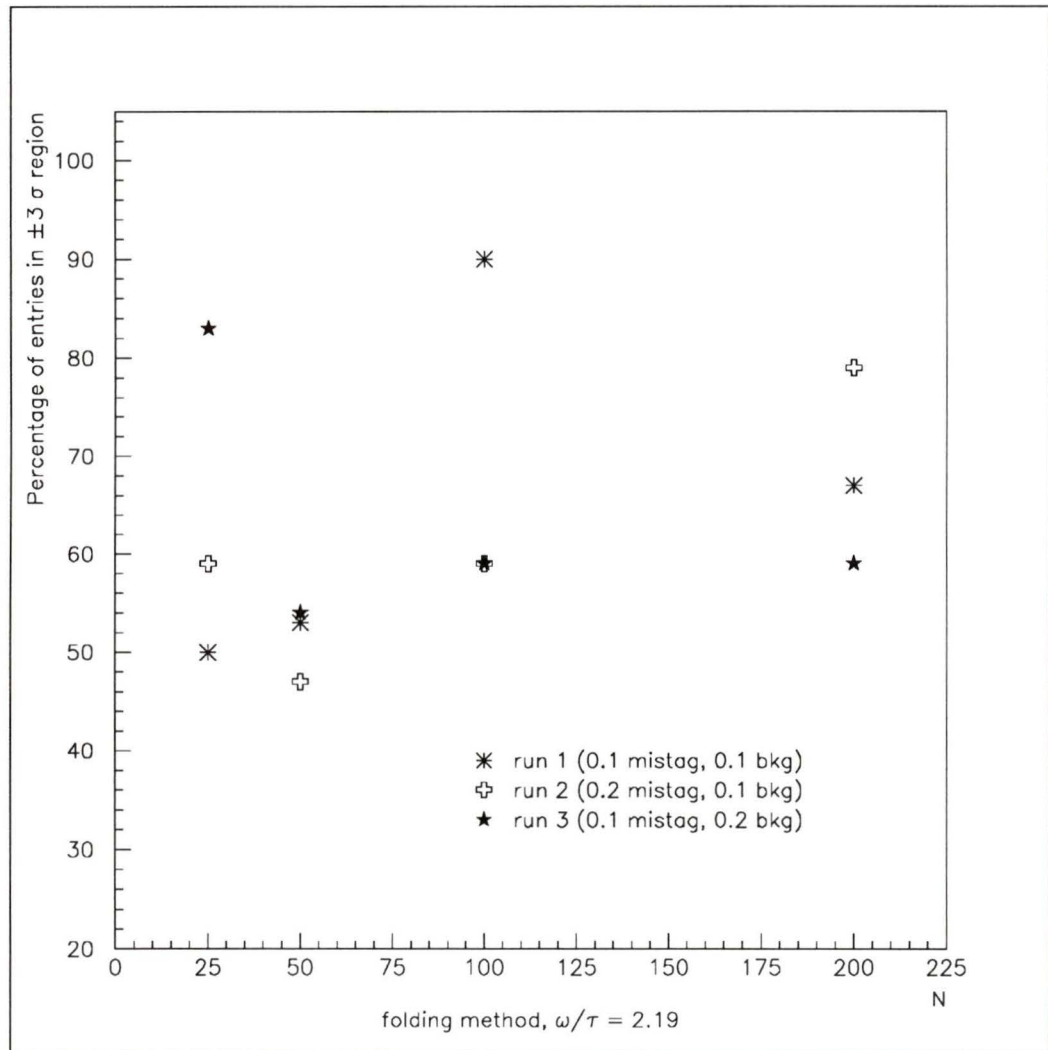


Figure 6.15: Folding method plot of the percentage of entries within the $\pm 3\sigma$ region versus N for an input $\omega/\tau = 2.19 \text{ ps}^{-1}$. Note that the y-axis starts at 20 percent.

uncertainty due to the finite time bin size, x_{bin} , and represents an inherent inaccuracy in the folding method.

- The folding method is not appropriate at low frequencies because the exponential term in distribution (5.4) shifts the folding frequency and more statistics are required for longer periods.
- The folding method appears to be an appropriate method of analysis only in situations where one has no prior knowledge of the analytic form of the measured distributions and good statistical precision. It will reveal a periodicity, but if the resulting frequency is low, it should be treated with caution. For the low statistics environment which will most likely be encountered in an experiment (about 200 or less B_s^0 events as discussed in this thesis), the folding method is inappropriate.

6.4 The Fast Fourier Transform Method

A Fast Fourier Transform was applied to 200, 100, 50, and 25 event samples generated according to distribution (5.4) in the range -0.5 ps to 10.0 ps resulting in the frequency spectrum of the sample events (see figure 5.7a). The peak of the frequency spectrum (the first local maximum after the $1/\omega$ curve due to the exponential term) was recorded and this procedure was repeated for 100 sets of sample events. The resulting 100 frequency peaks were entered into a histogram. Typical distributions of the peak frequency are shown in figure 6.16. The distribution is not Gaussian-like and hence the iterative procedure of Gaussian fits was not used.

Instead of using iterative Gaussian fits, the mean and the SD of the frequency spectrum were recorded. The FFT method was used on the sets of sample events created from the parent parameters described in table 6.4. The mean and SD of the

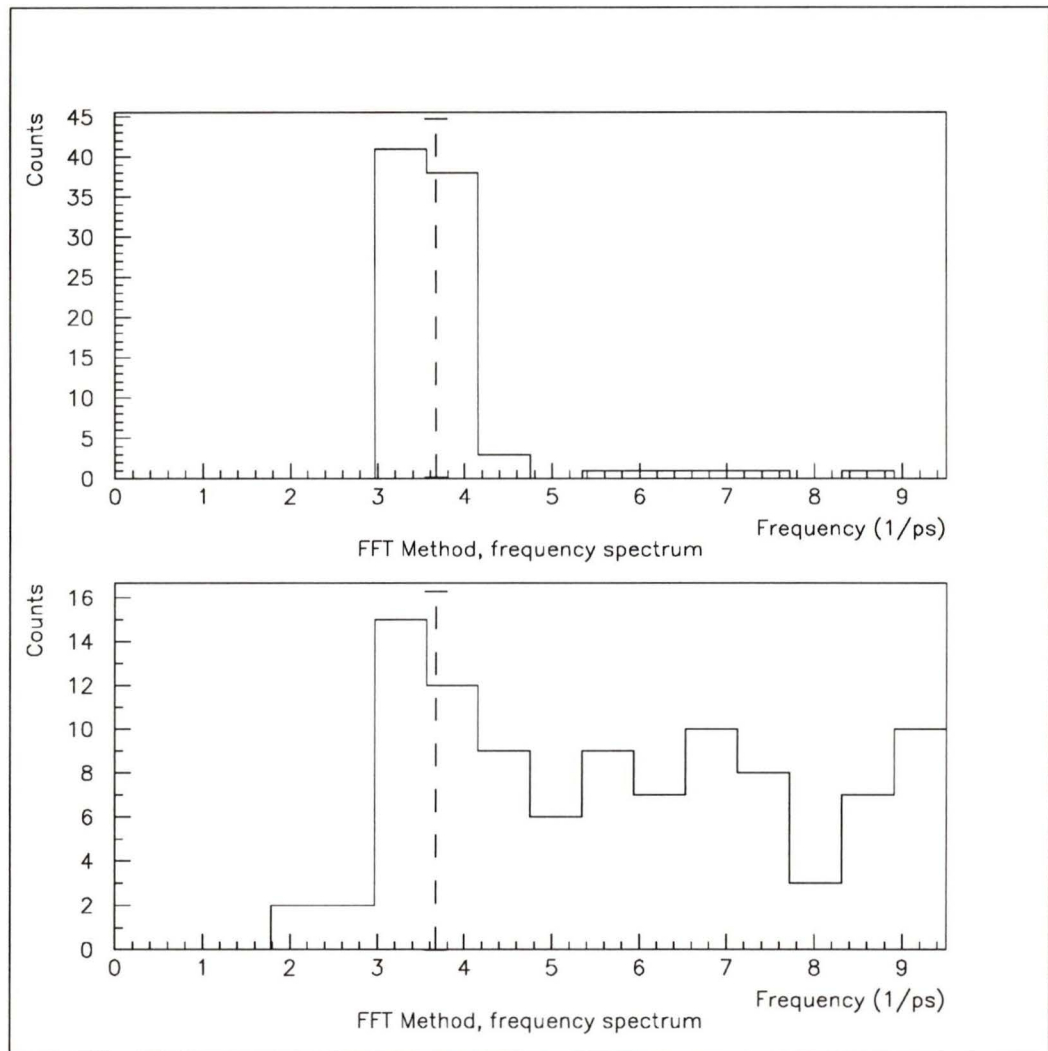


Figure 6.16: a) An output frequency distribution for the FFT method with input $\frac{\omega}{\tau} = 3.65 \text{ ps}^{-1}$ and 100 sets of 200 sample events were used. b) Another output frequency distribution with input $\frac{\omega}{\tau} = 3.65 \text{ ps}^{-1}$ and 100 sets of 25 sample events were used. The dashed lines indicate the value of the input $\frac{\omega}{\tau}$.

<i>The FFT Method</i>					
Run	# of events/set	input $\frac{\omega}{\tau}$ (ps^{-1})	bin size (ps)	mistag	bkg
1	200, 100, 50, 25	0.73, 2.19, 3.65, 5.11, 6.57	0.164	0.1	0.1
2	200, 100, 50, 25	0.73, 2.19, 3.65, 5.11, 6.57	0.082	0.1	0.1
3	200, 100, 50, 25	0.73, 2.19, 3.65, 5.11, 6.57	0.164	0.2	0.1
4	200, 100, 50, 25	0.73, 2.19, 3.65, 5.11, 6.57	0.164	0.1	0.2

Table 6.4: Table of runs performed with the FFT program.

entire reconstructed $\frac{\omega}{\tau}$ distributions will be discussed in section 6.4.1. The results of the FFT method can be found in Appendix B.

6.4.1 The Results of the FFT Method

The FFT method was used to analyze 100 sets of 200, 100, 50, or 25 sample events generated according to distribution (5.4) with parent parameters given in table 6.4. The results of these runs were frequency (or amplitude) distributions from the FFT. The mean and the SD of the distributions of peak frequency of the amplitude distribution were found and the following section shows plots of these quantities for various input parameters.

Figure 6.17 is a plot of the absolute value of the percentage difference of the mean of the peak frequency distribution from the input $\frac{\omega}{\tau} = 2.19 \text{ ps}^{-1}$. As with the corresponding plots for the other two methods, the percentage difference increases as the number of sample events used per set for 100 sets decreases. Run 2, which corresponds to a lower bin size of the time evolution of the B_s^0 oscillation period, shows substantially higher percentage difference than the other three runs. Chapter 5 described how decreasing the bin size of the time distribution allows a larger range of $\frac{\omega}{\tau}$ to be explored but does not improve the frequency resolution of the distribution. Statistical fluctuations at high ω/τ can create peaks which are higher than

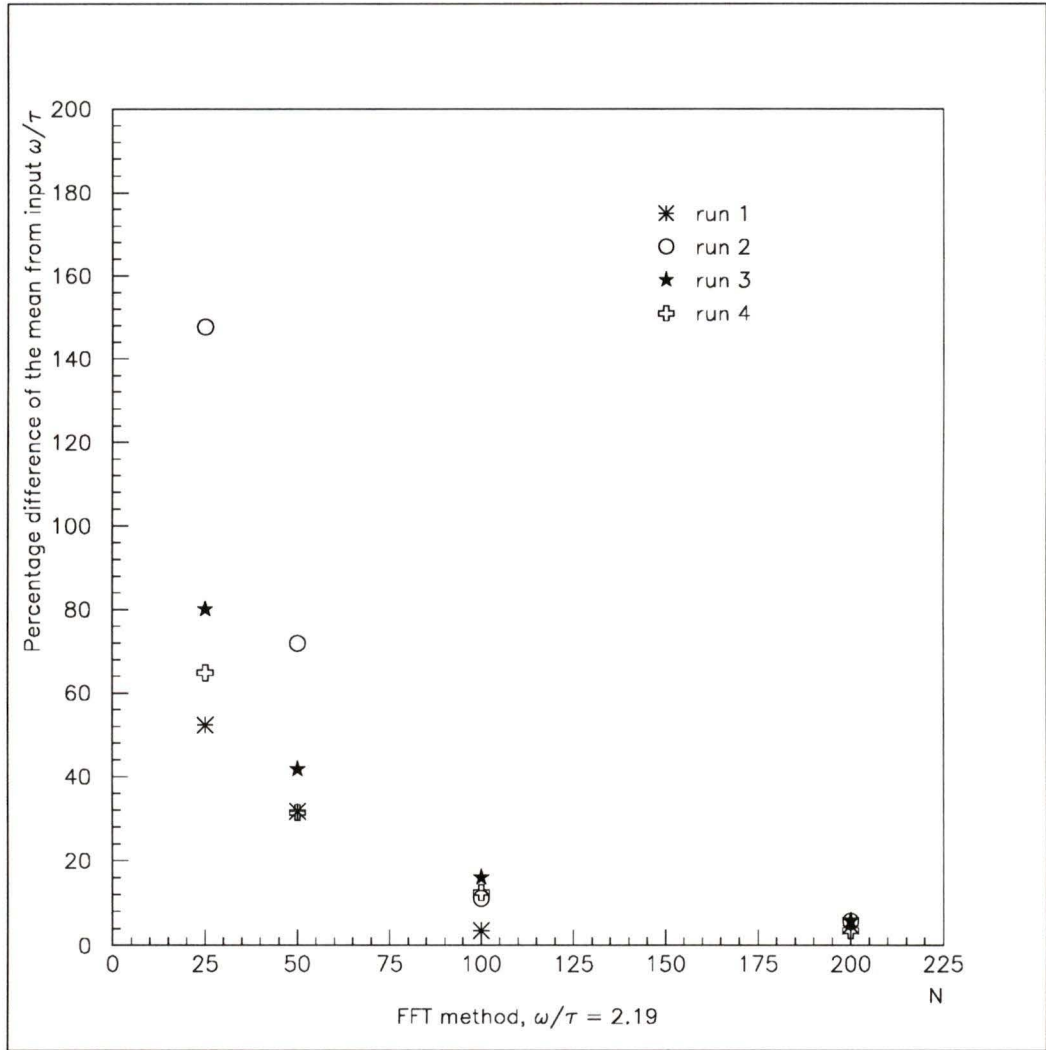


Figure 6.17: FFT method plot of the absolute percentage difference of the mean of the peak frequency distributions from the input ω/τ versus N for an input $\omega/\tau = 2.19 \text{ ps}^{-1}$. Since the peak frequencies were measured at the upper edge of a frequency bin, the mean values used in this plot were shifted by half a frequency bin width (0.3 ps^{-1}) from the values in Appendix B to give the value of the peak frequency at the center of the bin. The plot converges to zero percent at $N = 200$.

the signal at the nominal ω/τ causing a large percentage difference from the mean. All four runs appear to converge at a small percent difference of the mean from the input $\frac{\omega}{\tau}$. It should be noted that this FFT method like the folding method measures directly the frequency of the time spectrum of the B_s^0 oscillation probability distribution. It was noted in chapter 5 that the amplitude distribution has a frequency bin width of about 0.6 ps^{-1} . Any deviation in the mean due to the exponential term in equation (5.4) is hidden by the bin size of the amplitude distribution. One sees from figure 6.17 that increasing the percentage of mistagging (run 3) increases the percentage difference for low values of N. The signed difference between the mean value of the output frequency and the input $\frac{\omega}{\tau}$ was examined for systematic shifts. There was a strong tendency for the recovered value to be too large.

The Fourier Transform amplitude distribution of an exponential convoluted with a Gaussian resolution is subtracted from the amplitude distribution calculated by the FFT analysis (see figure 6.18) following the same procedure as for the high statistics data described in chapter 5. The dominant effects on the measurement are the amplitude distribution bin size and spurious structure due to statistical fluctuations in the time domain spectrum. Subtracting the Fourier Transform of the exponential and normalizing to the first bin does not improve the statistics and therefore does not enhance the signal. Figure 6.19 shows a reanalysis of the data with the amplitude distribution of the Fourier transform of the exponential subtracted off. Results appear to be worse when the Fourier Transform of the exponential is subtracted. This is probably due to the fact that the FFT of the time distribution must be taken from -0.5 ps to account for the smearing of the time distribution to negative time which gives a frequency distribution which has a dip and then a rising slope at frequencies above 2.5 ps^{-1} .

The plot in figure 6.20 shows $\frac{SD}{\sqrt{N}}$ versus N for an input $\frac{\omega}{\tau} = 2.19 \text{ ps}^{-1}$. Once

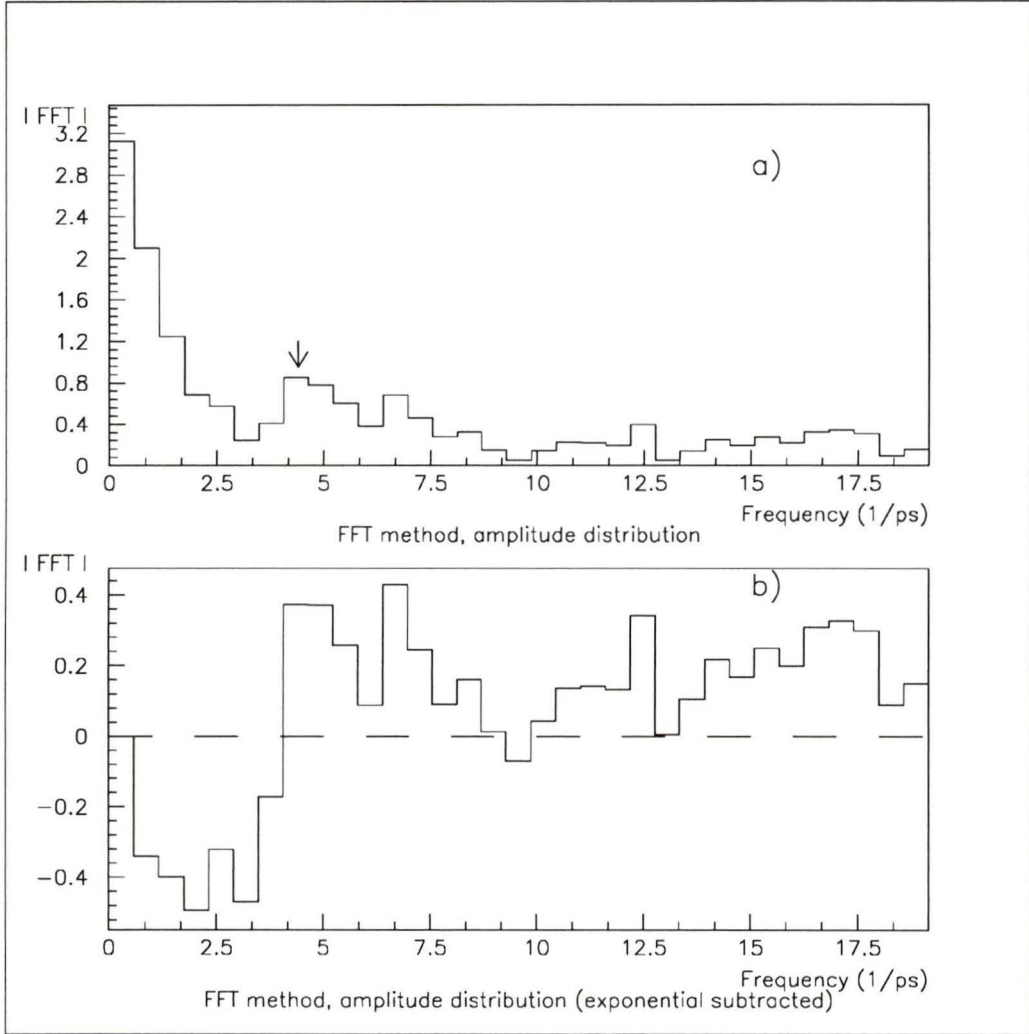


Figure 6.18: a) Amplitude distribution from an FFT applied to 200 events binned into 0.16 ps bins for $\frac{\omega}{\tau} = 2.19 \text{ ps}^{-1}$, $\sigma = 0.13 \text{ ps}$, $\tau = 1.37 \text{ ps}$, 10 percent mistagging, 10 percent background, and frequency bin size of 0.6 ps^{-1} . The arrow shows the peak frequency at 2.25 ps^{-1} . (Divide the peak value by two to get the frequency.) b) Amplitude distribution from an FFT applied to the same 200 events with the exponential term subtracted and binned into 0.16 ps bins for $\frac{\omega}{\tau} = 2.19 \text{ ps}^{-1}$, $\sigma = 0.13 \text{ ps}$, $\tau = 1.37 \text{ ps}$, 10 percent mistagging, 10 percent background, and frequency bin size of 0.6 ps^{-1} . The peak at 2.25 ps^{-1} has disappeared.

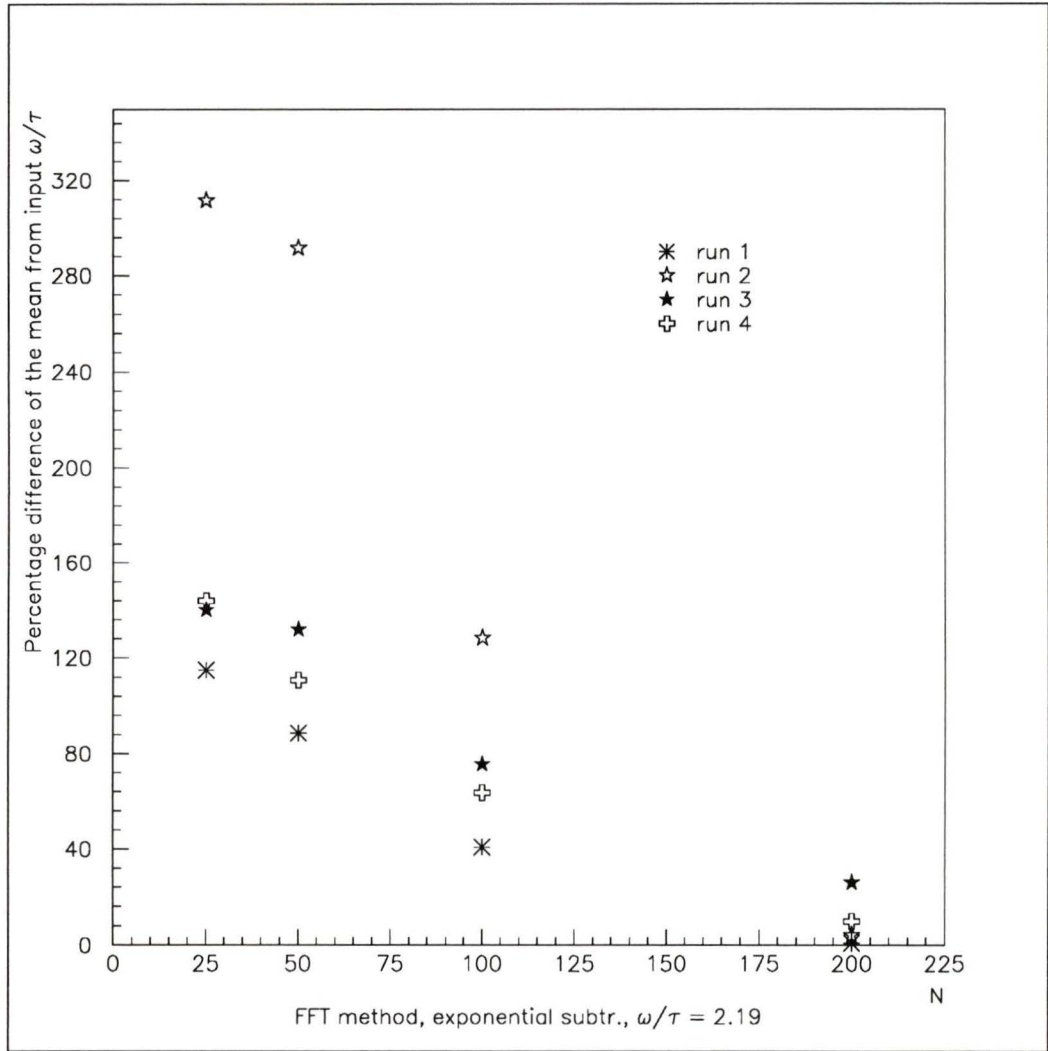


Figure 6.19: FFT method plot of the absolute percentage difference of the mean of the peak frequency distributions with the exponential term subtracted from the input ω/τ versus N for an input $\omega/\tau = 2.19 \text{ ps}^{-1}$. The plot converges to zero percent at $N = 200$. The mean values in these plots were also shifted by half a bin as described in figure 6.17.

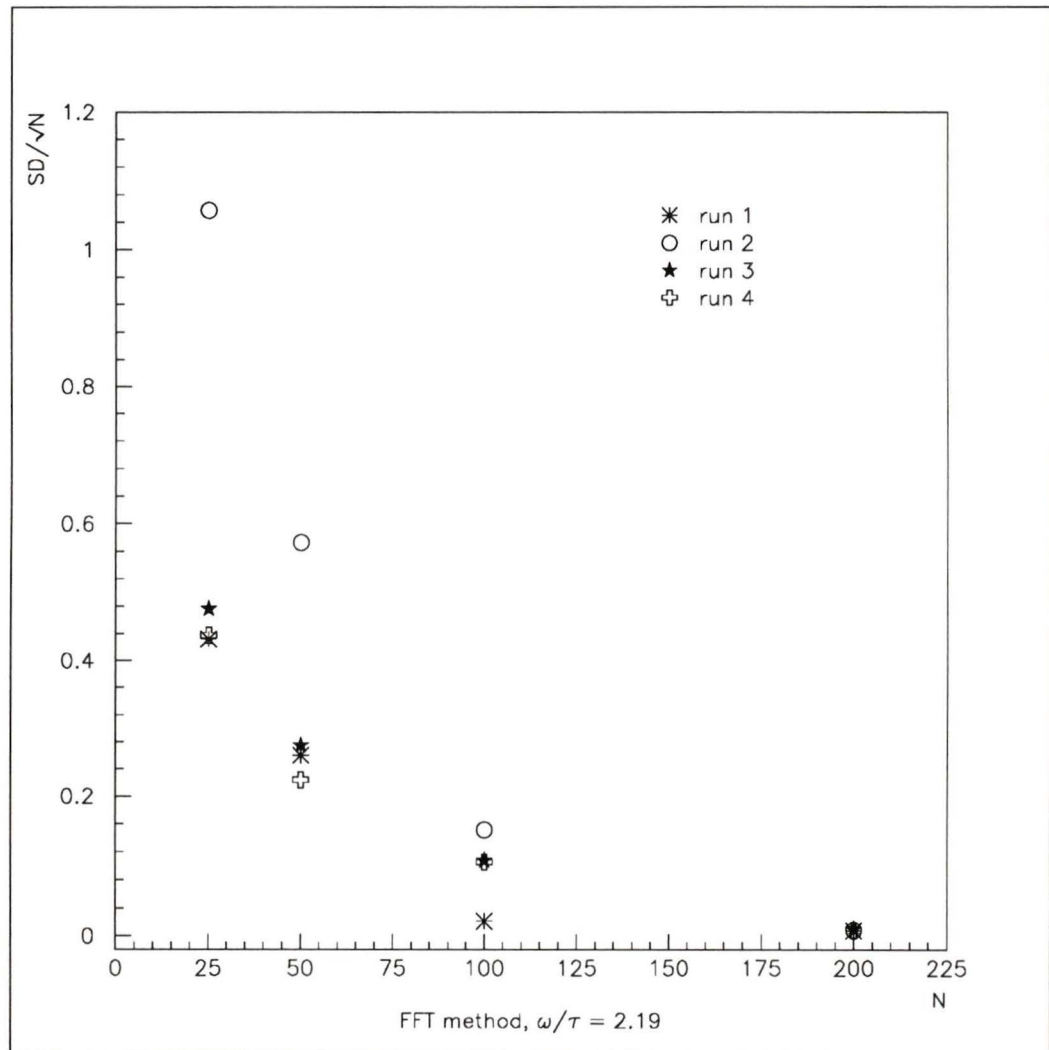


Figure 6.20: FFT method plot of SD/\sqrt{N} of the peak frequency distribution versus N for an input $\omega/\tau = 2.19 \text{ ps}^{-1}$.

again, the SD increases as N decreases. Larger values of SD are apparent for run 2 (small bin size) for the same reasons as given above for the percent difference plots.

Figure 6.21 is a plot of $\frac{SD}{\sqrt{N}}$ versus N of the peak frequency distribution coming from data which had the amplitude distribution of the exponential term in equation (5.4) subtracted out. From this figure, it appears that subtracting the exponential also adversely affects the SD of the peak frequency distribution. Due to this result and the result from figure 6.19, all further runs have been analyzed without subtracting the amplitude distribution of the exponential.

The percentage difference of the mean from the input $\frac{\omega}{\tau}$ and the $\frac{SD}{\sqrt{N}}$ values were averaged over the four runs and plotted versus N for input $\omega/\tau = 0.73, 2.19, 3.65, 5.11,$ and 6.57 ps^{-1} in figures 6.22 and 6.23 respectively. Figure 6.22 shows very large percentage differences with large errors for input $\omega/\tau = 0.73 \text{ ps}^{-1}$. The FFT method like the folding method is a poor method to use for low input ω/τ but improves as the input $\frac{\omega}{\tau}$ increases. The percentage differences for $\omega/\tau = 2.19, 3.65, 5.11,$ and 6.57 ps^{-1} converge to about zero percent as N becomes large.

Figure 6.23, a plot of $\frac{SD}{\sqrt{N}}$ versus N , suggests some systematic dependence of $\frac{SD}{\sqrt{N}}$ on the input ω/τ for a given N .

From these figures, the following conclusions may be drawn:

- At large values of input frequency the peak finding algorithm, taking the first local maximum, biases the result towards finding peaks at low frequency due to statistical fluctuations.
- Results of the FFT method at larger input frequency show increased values for the SD of the output frequency distribution since statistical fluctuations at high frequency can be comparable to the signal at the nominal ω/τ .
- The FFT method like the folding method is inappropriate for low frequency

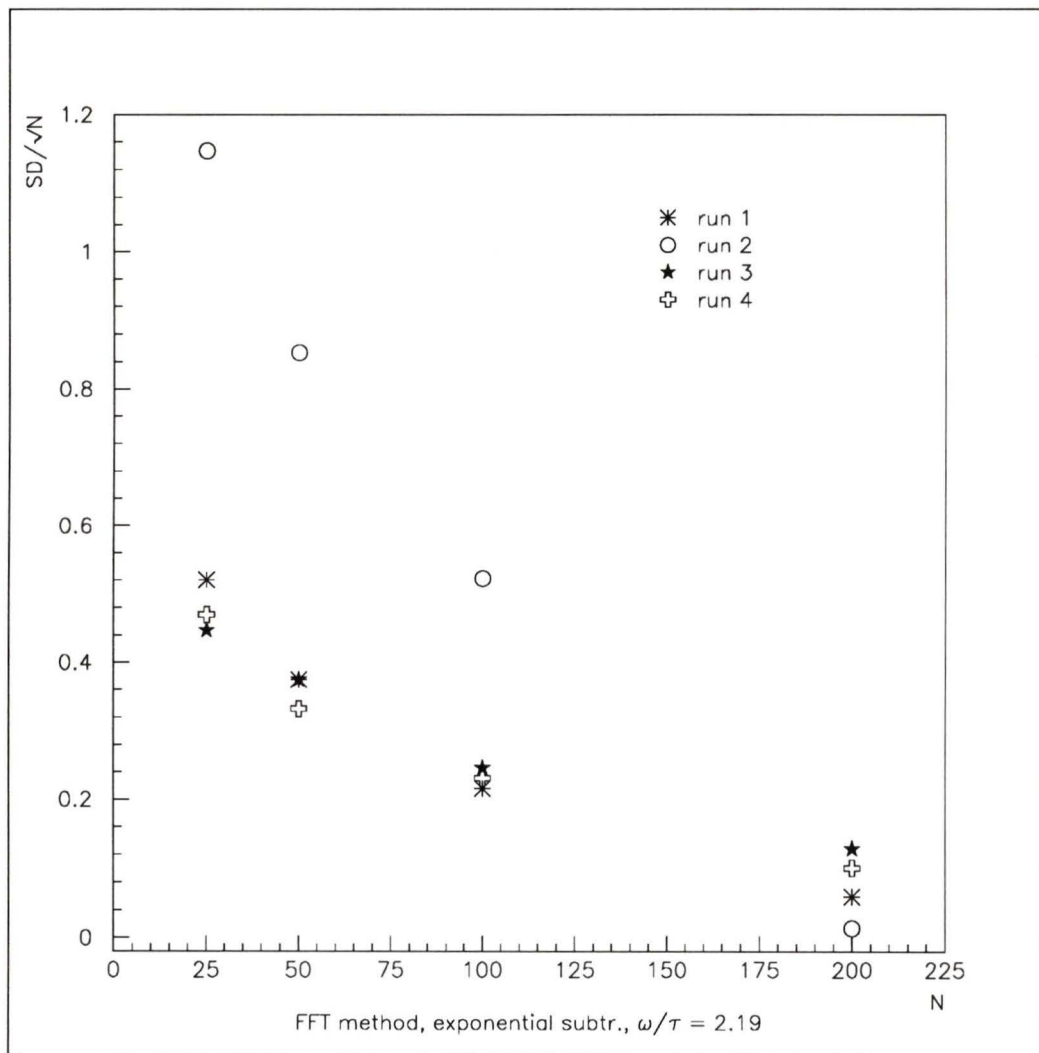


Figure 6.21: FFT method plot of SD/\sqrt{N} of the peak frequency distribution with the exponential term subtracted versus N for an input $\omega/\tau = 2.19 \text{ ps}^{-1}$.

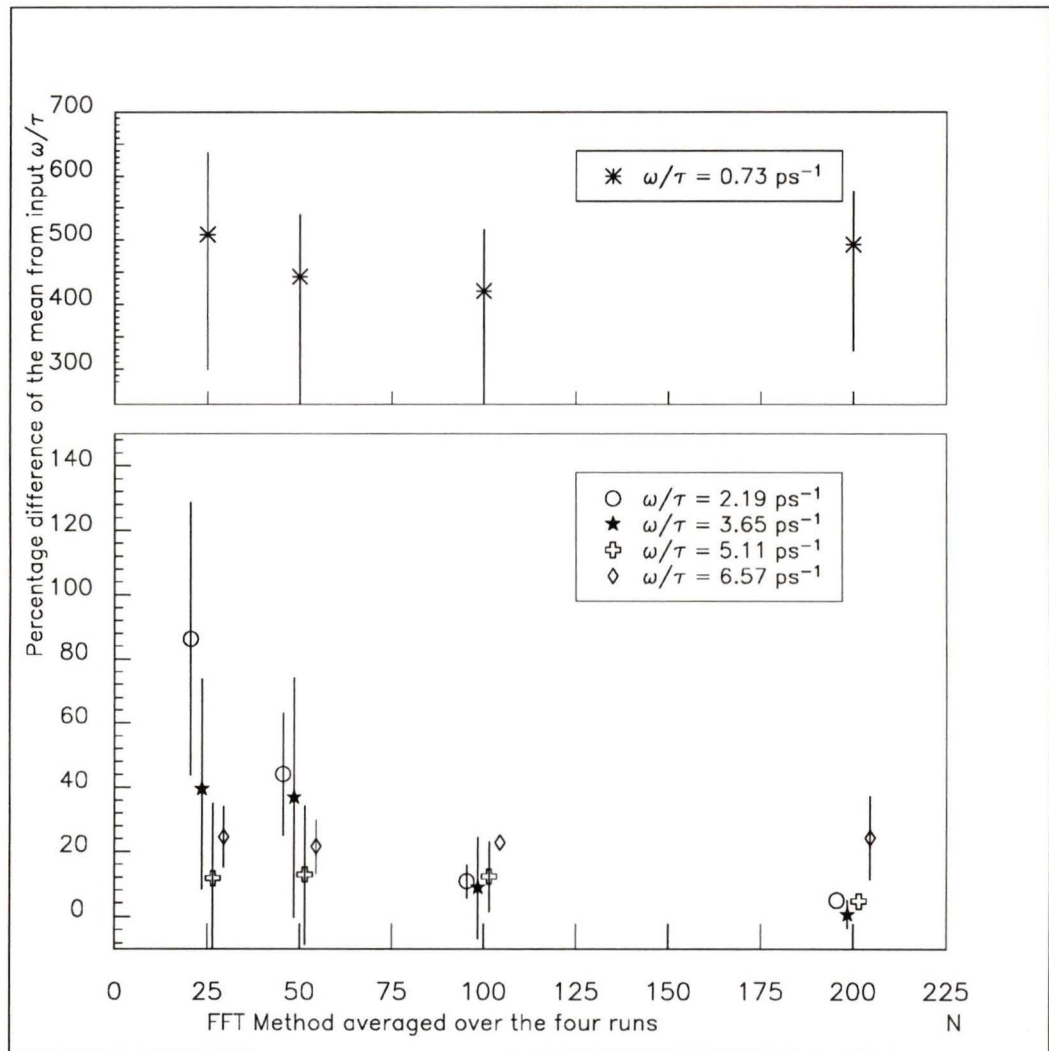


Figure 6.22: FFT method plot of the absolute percentage difference of the mean of the output frequency distribution from the input ω/τ averaged over the four runs versus N . Data at $N = 25, 50, 100,$ and 200 have been slightly offset for clarity. Note that there is a change in scale for the y-axis of the upper plot. Note that the y-axis starts at -10 percent. The mean values in these plots were also shifted by half a bin as described in figure 6.17.

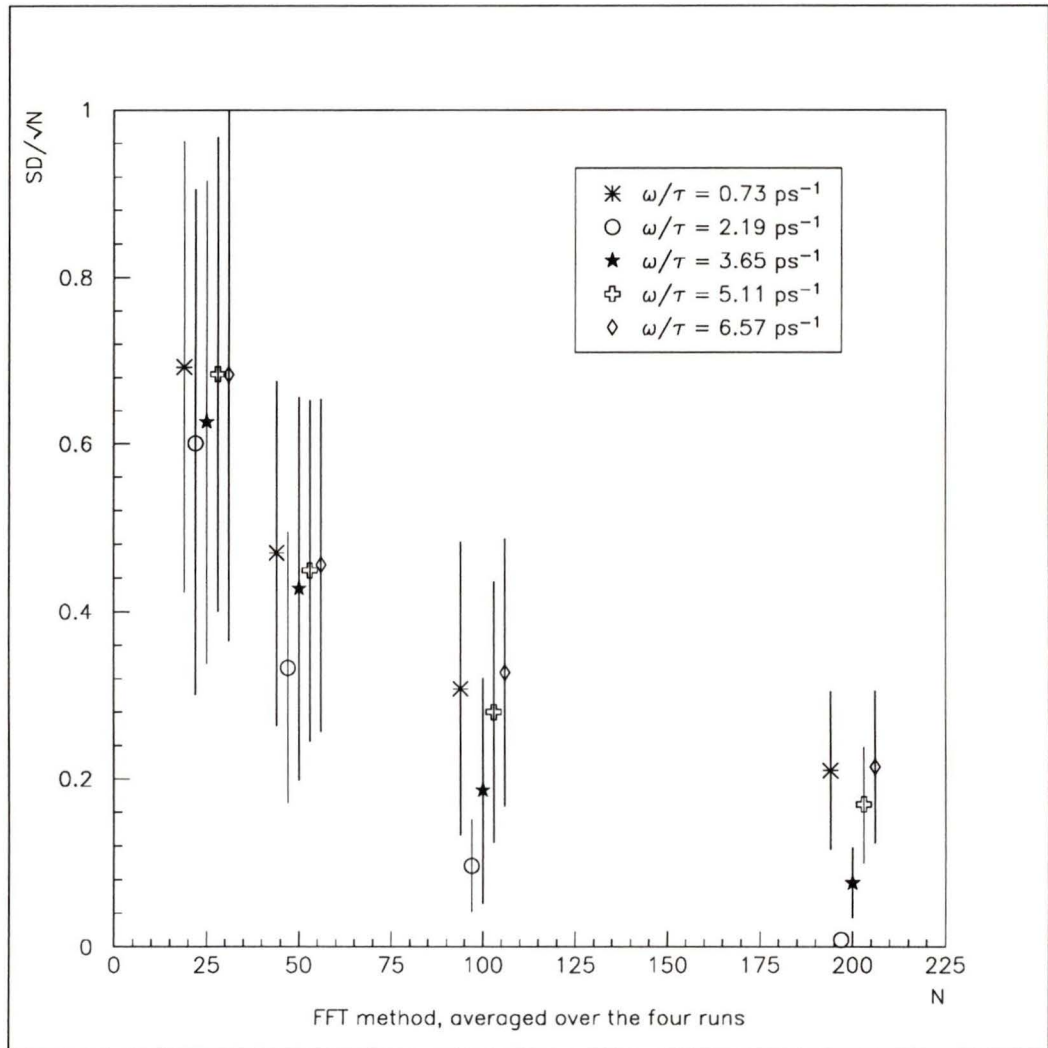


Figure 6.23: FFT method plot of SD/\sqrt{N} averaged over the four runs versus N . Data at $N = 25, 50, 100,$ and 200 have been slightly offset for clarity.

distributions.

- Due to the coarse bin size in the frequency distribution imposed by the lifetime of the B_s^0 , there is a large uncertainty (0.6 ps^{-1}) in measuring the frequency of the data when using the FFT method. Only using higher statistics which would extend the range of measured time of flight can decrease this uncertainty. Hence, the FFT method is inadequate for such low statistics.

In 1990, Moser [41] proposed to measure the frequency of oscillation of B_s^0 mesons by performing an FFT on the data. In his B_s^0 simulations, Moser assumed a time smearing of 0.1 ps and 0.2 ps and explicitly included the effects of B_d^0 mixing and non-oscillating charged B mesons in the equation which generated the data. This thesis assumes a pure B_s^0 sampled obtained by selection criteria on the lepton momentum. He generated 200 sets of 300 sample events from his equation describing B_s^0 mixing and explored the ω range of 1.5 to 7.5. The data were generated between zero and 10 lifetimes, corresponding to a frequency bin width of 0.5 ps^{-1} , ignoring the negative time region. The time bin width of generated data was 0.1 ps. These parameters are compared in table 6.5 with the parameters used in this thesis for the FFT method. Moser measured the distribution of peak frequency for 200 sample runs and had typical values of SD of 0.2 to 0.5 for a time resolution equal to $\sigma = 0.1 \text{ ps}$ to 0.2 ps and $\omega = 1.5$ to 5.0 . These values of SD are similar to those obtained from this thesis where for example at $N = 200$ events and $\omega = 3$ and 5 for run 1, the values of SD are 0.15 and 0.60 respectively (the values of SD are those given in Appendix B multiplied by 1.37 ps in order to compare with Moser who discusses ω distributions and not ω/τ distributions). Moser defined a confidence level as the percentage of peak frequencies within ± 1 unit of the input ω . He concluded from his analysis, that at $\sigma = 0.1 \text{ ps}$, a measurement of up to $\omega = 3.75$ could be made with

	Moser	Thesis
Data	B_s^0 , B_d^0 , B , mistag	B_s^0 , bkgnd, mistag
events	200×300 events	100×200 , 100, 50, 25 events
resolution	0.1 ps, 0.2 ps	0.13 ps
ω range	1.5 to 7.5	1 to 9
time bin	0.1 ps	0.08 ps and 0.16 ps
freq bin	0.5 ps^{-1}	0.6 ps^{-1}

Table 6.5: Table of comparison of the parameters used by Moser and the parameters used in this thesis for the FFT method.

an 88 percent confidence level. At $\sigma = 0.2$ ps, a measurement of up to $\omega = 2.5$ could be made with a 75 percent confidence level. Applying his definition of confidence level to this thesis, one finds for run 1 with a time resolution equal to $\sigma = 0.13$ ps on 100 sets of 200 sample events at $\omega = 3$ (the results which lies in the range of his conclusions given above), a measurement can be made with 100 percent confidence. At $\omega = 5$ with 100 sets of 200 events, a measurement can be made with a 93 percent confidence level. The small differences in the confidence levels of Moser's results and the confidence levels from this thesis' results are probably because Moser included the effects of B mesons other than the B_s^0 while this thesis assumes a sample of pure B_s^0 .

6.5 Conclusions Based on the Results of the Three Methods of Analysis

A few conclusions may be drawn based on the results of the three methods of measuring B_s^0 oscillations given in the three previous sections:

- At low statistics, which might be anticipated (≤ 200 events), the fitting method is really the only viable method of analysis. Here, a hypothesis can be tested

against data with low statistics. The low statistics can confuse both the folding and the FFT methods. At high statistics (≥ 200 events), the folding and FFT methods become viable and are attractive since they do not require fitting procedures.

- Increasing the percentage mistagging has the largest effect of all of the parameters in introducing uncertainty into the measurement of ω/τ .
- Increasing the percentage flat background appears to have little effect on the results.
- Both the folding and the FFT methods are poor methods to use at low frequency. Using an input $\omega/\tau = 0.73 \text{ ps}^{-1}$ results in large values of SD and large percentage difference of the mean from the input $\frac{\omega}{\tau}$ of the output frequency distributions.
- For each of the three analysis methods for a fixed N , the values of SD averaged over all runs show a systematic dependence on ω/τ . SD increases as ω/τ increases.
- The observed mean ω/τ averaged over all runs was closest to the nominal value when analyzed by the fitting method.
- The fitting method produces the most Gaussian looking output frequency distributions of all three methods. $\omega/\tau = 0.73 \text{ ps}^{-1}$ with $N = 50, 100, \text{ and } 200$; $\omega/\tau = 2.19 \text{ ps}^{-1}$ with $N = 100 \text{ and } 200$; and $\omega/\tau = 3.65 \text{ ps}^{-1}$ with $N = 200$ are the runs which satisfy the 90 percent Gaussian criterion for “stable” results.

Chapter 7

Summary of Results

In this thesis, the concept of $B_s^0 - \bar{B}_s^0$ oscillation was developed within the framework of the Standard Model. The Cabibbo-Kobayashi-Maskawa matrix description of the mixing of mass eigenstates was introduced along with the second order weak interaction box diagrams as the mechanism responsible for B_s^0 mixing. The time evolution of CP eigenstates of the neutral B_s^0 mesons was calculated by solving the time-dependent Schrödinger equation, and the system was shown to oscillate between the particle and the antiparticle state with a frequency of oscillation, $\frac{\Delta M}{\hbar}$.

A measurement of B_s^0 oscillations involves a knowledge of the particle-antiparticle nature of the B_s^0 meson at the B meson production and decay points. Two methods of determining this, the dilepton tagging method and the primary kaon method, were explored. From these methods, it was estimated that less than a few hundred B_s^0 could be identified clearly at a detector like OPAL within one year of LEP operation.

The effects of typical experimental resolutions and procedures on the measurement of B_s^0 oscillations were examined. These included the measurement of the time of flight of the B mesons, the mistagging of leptons coming from B^0 mesons on the other side of the interaction which change flavor before decaying, and the detector

resolution which smears the measurements of the B_s^0 decay length. A careful study was made of the energy loss of an ionizing particle in the OPAL silicon microvertex detector. For a test beam measurement of three silicon detector ladders, the cluster pulse height sums were fitted to Landau distributions convoluted with Gaussians. The detector and read out noise was determined for each ladder. The Landau distribution fits to the energy loss data and the measured detector noise were found to be consistent with expected values.

Programs which generate possible sample measurements of the B_s^0 time of flight were written by the author to explore three different methods of measuring the frequency of oscillation of B_s^0 mixing. Simulated events were generated according to the time evolution distribution of a B_s^0 or a \bar{B}_s^0 meson which decays without changing flavor with the following conditions: a 10 to 20 percent lepton mistagging and 10 to 20 percent flat background. The data in the sample distributions were entered into histograms with bin sizes appropriate to the time resolution of the detector, and hence the time smearing of the distributions. Each program then attempted to recover the parameters of the parent distribution. The fitting method used the equation describing the probability distribution of a B_s^0 which decays without changing flavor, to fit the experimental distribution and recover the parameter, $\omega = \frac{\Delta M}{2\Gamma}$, of the original parent distribution. The folding method and the FFT method were also used on the simulated events in order to find the frequency of oscillation. In a sense, the folding method is like the FFT method, since both methods find the main frequency component of the parent distribution. The goal of these methods was to see how few B_s^0 events are necessary to determine the frequency of oscillation to a given precision.

Sample events were repeatedly created from the parent distribution for B_s^0 mesons which decay without changing flavor for various input parent parameters.

The reconstructed parameters were the final output of the three programs. The mean and standard deviation of each distribution were found and the similarity of the distribution to a Gaussian was quantified. It was found that both the folding and the FFT methods were poor methods to use at low frequency since a frequency of $\omega = \frac{1}{2} \frac{\Delta M}{\Gamma} = 1$ resulted in large values of SD and large percentage differences between the mean of the frequency distribution and the input ω . It was also found that the fitting analysis produced the most Gaussian-like output frequency distributions of the three methods. From the analyses performed on the simulated events, it was found that increasing the mistagging parameter had the largest effect on the measured output frequency. It increased the SD and reduced the probabilities of a Gaussian describing the distributions. The fitting method with an input of $\frac{\Delta M}{\Gamma} = 2$ required only 50 B_s^0 events for the output frequency distribution to satisfy the 90 percent Gaussian criterion while for $\frac{\Delta M}{\Gamma} = 6$, 100 events were required and $\frac{\Delta M}{\Gamma} = 10$ required 200 events (see figure 7.1). The folding and FFT methods were found to be inadequate for 200 or less B_s^0 events.

It is the opinion of the author that the folding and FFT methods should only be considered as methods of analysis in situations with good statistics (≥ 300 events). The fitting method produces more Gaussian-like results since it takes into consideration explicitly all of the parameters used to generate the data. However, an exact knowledge of B_s^0 oscillation is necessary in order to derive the fitting equation. No such knowledge is necessary with the folding and FFT methods since these methods only look for periodicities in the data. The folding and FFT methods however offer less understanding as to what these periodicities mean.

With 200 B_s^0 , frequencies up to $\frac{\Delta M}{\Gamma} = 10$ could be measured with good precision. Within the confines of the model used, the input value of ω/τ can be recovered with a 5 to 10 percent accuracy. When the LEP collider reaches its design luminosity, the

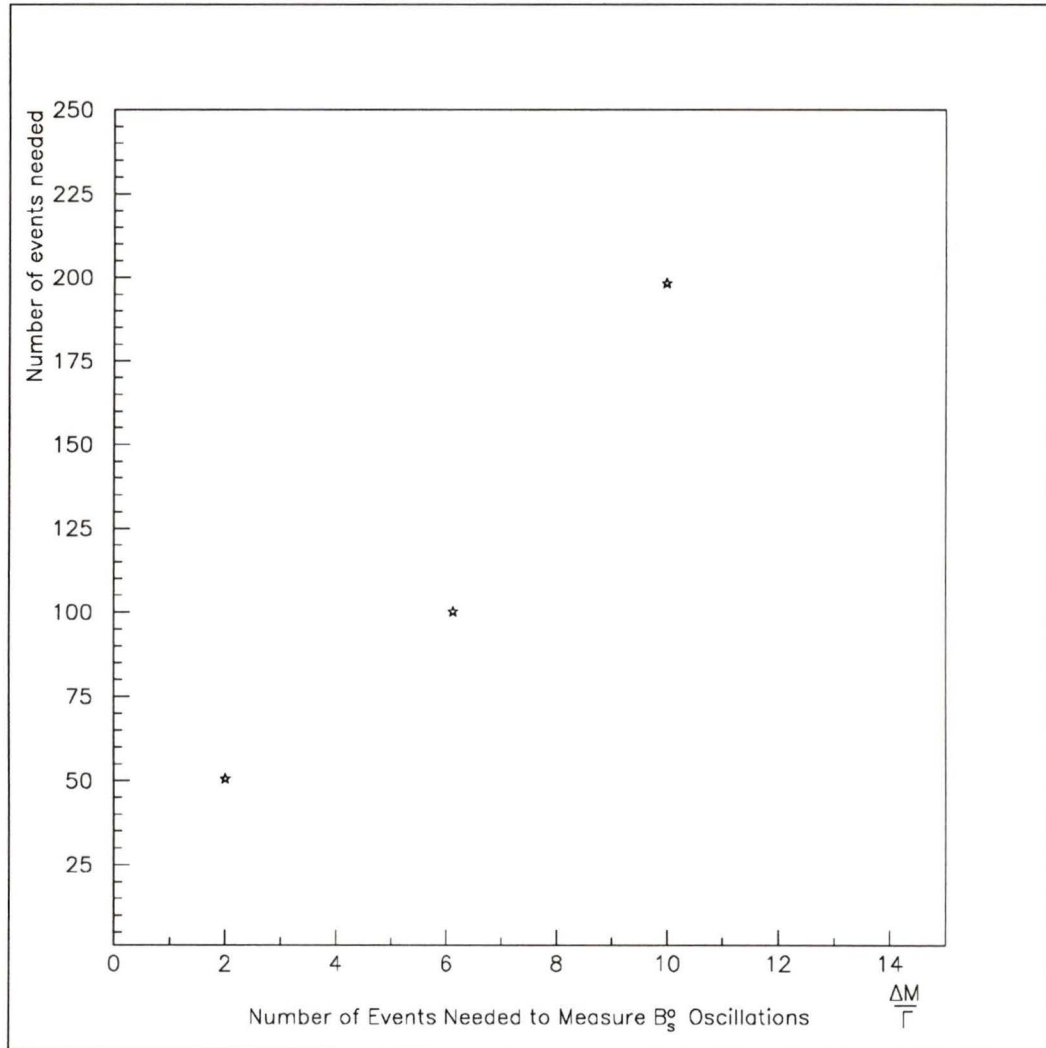


Figure 7.1: The number of events needed to satisfy the 90 percent Gaussian criterion for varying $\frac{\Delta M}{\Gamma}$ based on the results from the fitting method.

OPAL detector may be able to reconstruct 200 B_s^0 within 2 years. During this time, a double-sided silicon microvertex detector which would make both $r - \phi$ and $r - z$ measurements could be installed. It will reduce the error in the decay length of the B_s^0 and hence lower the value for σ_τ which is responsible for the smearing effect on the measurement of the time of flight of the B_s^0 . This year, B_s^0 mesons have been identified at LEP. It is quite likely that the lifetime will be measured in the next year and mixing measurements will be possible in the following year.

Bibliography

- [1] Particle Data Group (1992). Review of Particle Properties. *Physical Review D: Particles and Fields*, **45D**: p. VII.143 and VII.158.
- [2] Hemingway, R. J. (1991). LEP - The Z^0 Factory. *Proceedings of the Sixth Lake Louise Winter Institute: Particle Physics- The Factory Era*. Campbell, B. A. *et al.* eds.. Singapore: World Scientific, p. 386 - 398.
- [3] Glashow, S. (1961). *Nuclear Physics*, **B22**: p. 579.
- [4] Weinberg, S. (1967). *Physics Review Letters*, **19**: p. 1264.
- [5] Salam, A. & J. C. Ward (1964). *Physics Letters*, **13**: p. 168.
- [6] Griffiths, D. (1987). *Introduction to Elementary Particles*. New York: John Wiley & Sons, Inc., p. 46.
- [7] Arnison, G. *et al.* (1983). Experimental Observation of Isolated Large Transverse Energy Electrons with Associated Missing Energy at $\sqrt{s} = 540$ GeV. *Physics Letters*, **122B**: p. 103.
- [8] Banner, M. *et al.* (1983). Observation of Single Isolated Electrons of High Transverse Momentum in Events with Missing Transverse Energy at the CERN $p\bar{p}$ Collider. *Physics Letters*, **122B**: p. 476.
- [9] Bagnaia, P. (1983). Evidence of $Z^0 \rightarrow e^+e^-$ at the CERN $p\bar{p}$ Collider. *Physics Letters*, **129B**: p. 130.
- [10] Particle Data Group (1990). Review of Particle Properties. *Physics Letters*, **239B**: p. II.1.
- [11] Perkins, D. H. (1987). *Introduction to High Energy Physics* (3rd ed.), Menlo Park: Addison-Wesley Publishing Company, Inc..

- [12] Particle Data Group (1990). p. III.61.
- [13] Schroeder, H. (1988). Physics of B Mesons. *DESY 88-101*.
- [14] Lande, E. E. (1956). *Physics Review*, **103**: p. 1901.
- [15] Albrecht, H. *et al.* (ARGUS Collaboration) (1987). Observation of $B^0 - \bar{B}^0$ Mixing. *Physics Letters*, **192B**: p. 245.
- [16] Burchat, Patricia R. (1991). Physics at an Asymmetric- Energy B-Meson Factory. *Proceedings of the Sixth Lake Louise Winter Institute: Particle Physics-The Factory Era*. Campbell, B. A. *et al.* eds.. Singapore: World Scientific, p. 65 - 125.
- [17] Browder, T. *et al.* (1989). Preliminary Report of the $B\bar{B}$ Mixing and CP Violation Group. *SLAC-Report-354*, p. 294 - 357.
- [18] Artuso, M. *et al.* (CLEO Collaboration) (1989). $B^0\bar{B}^0$ Mixing at the $\Upsilon(4s)$. *Physics Review Letters*, **62**: p. 2233.
- [19] Foster, B. (1990). *Electron-Positron Annihilation Physics*. Bristol: IOP Publishing Ltd., p. 161.
- [20] Particle Data Group (1992). p. II.4.
- [21] Press, W. H. *et al.* (1986). *Numerical Recipes: The Art of Scientific Computing*. Cambridge: Cambridge University Press, p. 386 - 387.
- [22] Andersson, B. *et al.* (1983). Parton Fragmentation and String Dynamics. *Nuclear Reports* 97, Nos. 2 & 3, p. 31 - 145.
- [23] Particle Data Group (1992). p. II.17.
- [24] OPAL Collaboration (1991). Evidence for the Existence of the Strange b-flavoured Meson B_s^0 in Z^0 Decays. *CERN-PPE/91-144*.
- [25] Altarelli, G., R. Kleiss, & C. Verzegnassi (1989). Heavy Flavors. *Z Physics at Lep 1 - Vol. 1: Standard Physics*. CERN 89-08, p. 267 - 372.
- [26] Particle Data Group (1990). p. II.5 & II.12.
- [27] Ali, A. & F. Barreiro (1986). The Final States $l^\mp K^\pm K^\pm X$ in Jet Signatures of $B_s^0 - \bar{B}_s^0$ Mixings. *Zeitschrift für Physik C - Particles and Fields* 30, p. 635 - 642.

- [28] Atwood, W. B. (1988). B Meson Physics with Polarized Electron Beams at the SLC. *SLAC-PUB-4668*, p. 1 - 9.
- [29] OPAL Collaboration (1991). The OPAL Detector at LEP. *Nuclear Instruments and Methods in Physics Research*, **A305**: p. 275 - 319.
- [30] Fabjan, C. W. & J. E. Pilcher (1987). Drift and Detection of Charges in Silicon Detectors. *Proceedings of the ICFA School on Instrumentation in Elementary Particle Physics*. Singapore: World Scientific, p. 150 - 173.
- [31] Moisan, C. (1991). Test Beam Results for the FOXFET Silicon Microstrip Detector. *OPAL Technical Note TN-072*.
- [32] Gibson, V. (1991). The Silicon Microvertex Detector. *CERN Internal Report*.
- [33] Rancoita, P. G. & A. Seidman (1982). Silicon Detectors in High Energy Physics: Physics and Applications. *Rivista Del Nuovo Cimento*. Vol. 5, No. 7, p. 1 - 75.
- [34] James, F. & M. Roos (1981). MINUIT Function Minimization and Error Analysis, CERN Program Library Entry D506, Long Write Up.
- [35] CERN Computer Centre Program Library (1989).
- [36] Foster, p. 114.
- [37] OPAL Collaboration (1991). Measurement of the Average B Hadron Lifetime in Z^0 Decays. *CERN-PPE/91-201*.
- [38] Particle Data Group (1990). p. II.13.
- [39] Sobol', I. M. (1974). *The Monte Carlo Method*. Chicago: University of Chicago Press.
- [40] Particle Data Book (1990). p. III.37.
- [41] Moser, H. G. (1990). The Possibility to Measure the Time Dependence of the $B_s^0 - \bar{B}_s^0$ Oscillations Using Fourier Analysis. *Nuclear Instrumentation and Methods*, **A295**: p.435 - 442.
- [42] Abramowitz, M. and Stegun, I. (1964). *Handbook of Mathematical Functions with Formulas, Graphs, and Mathematical Tables*. New York: Dover Publications Inc..
- [43] Particle Data Group (1990). p. III.13.

- [44] Fernow, R. C. (1986). *Introduction to Experimental Particle Physics*. Cambridge: Cambridge University Press, p. 40 - 45.
- [45] Vavilov, P. V. (1957). Ionization Losses in High-Energy Heavy Particles. *JETP*. Vol. 5, No. 4, p. 749 - 751.
- [46] Landau, L. (1944). On the Energy Loss of Fast Particles by Ionization. *Journal of Physics*. Vol. VI, No. 4, p. 201 - 205.

Appendix A

Landau Energy Loss Theory

The average energy loss of a charged particle passing through matter is calculated from the equation

$$\langle E \rangle \approx \frac{dE}{dx} X, \quad (\text{A.1})$$

where X is the thickness of matter through which the particle passed. This equation is true as long as the energy loss is small relative to the energy of the incident particle. $\frac{dE}{dx}$ is given by the Bethe-Bloch equation [43]

$$\frac{dE}{dx} = 4\pi N_A r_e^2 m_e c^2 z^2 \frac{Z\rho}{A\beta^2} \left[\ln\left(\frac{2m_e c^2 \gamma^2 \beta^2}{I}\right) - \beta^2 - \frac{\delta}{2} \right] \quad (\text{A.2})$$

where N_A = Avogadro's number,
 r_e = classical radius of the electron,
 m_e = mass of the electron,
 z = charge of the incident particle,
 Z = atomic number of the medium,
 ρ = density of the medium,
 A = atomic weight of the medium,
 I = mean ionization potential of the medium, and
 δ = a correction known as the density effect.

Three basic theories of energy loss exist [44]. If ξ is the energy above which, on average, a high energy recoil electron, or delta ray, will be produced and E_{max} [43] is the maximum possible energy transfer in a collision then the ratio ξ/E_{max} determines the applicability for a given theory. $\xi = \frac{2\pi n_e z^2 e^4}{mv^2} X$ where for silicon $n_e = 6.99 \times$

10^{23} cm^{-3} and $z^2 = 1$ and

$$E_{max} = \frac{2m_e c^2 \beta^2 \gamma^2}{1 + 2\gamma \frac{m_e}{m_i} + \left(\frac{m_e}{m_i}\right)^2} \quad (\text{A.3})$$

where m_i is the mass of the incident particle. For

$$\frac{\xi}{E_{max}} \geq 1 \quad (\text{A.4})$$

the energy loss distribution is Gaussian. If ξ/E_{max} is in the range

$$0.01 \leq \frac{\xi}{E_{max}} \leq 1 \quad (\text{A.5})$$

then the Vavilov [45] theory must be considered and if

$$\frac{\xi}{E_{max}} \leq 0.01 \quad (\text{A.6})$$

the Landau [46] theory may be used.

ξ is 5.35 keV for a 5 GeV/c pion passing through 300 μm of silicon. E_{max} is approximately 1 GeV and so $\frac{\xi}{E_{max}} \approx 5.35 \times 10^{-6}$. Hence the Landau theory may be used when studying the energy loss of 5 GeV/c pions in silicon.

Three assumptions are used when deriving the Landau distribution:

1. The maximum allowable energy transfer is not limited. (The Vavilov distribution uses the correct expression for maximum allowable energy transfer.)
2. Individual energy transfers are large enough that electrons may be considered as free.
3. The incident particle maintains a constant velocity while crossing the medium.

For the Landau theory of energy loss, it is assumed that the typical energy loss is large relative to the electron binding energy but small relative to the maximum possible energy loss.

The Landau distribution is given by the equation [46] [33]

$$\phi(\lambda) = \frac{1}{2\pi i} \int_{\sigma-i\infty}^{\sigma+i\infty} \exp(\lambda u - u \ln u) du, \quad \text{for } \sigma > 0 \quad (\text{A.7})$$

where

$$\lambda = \frac{1}{\xi} [E_{lost} - \xi (\ln \frac{\xi}{\epsilon} + 1 - \gamma_E - \delta)] \quad (\text{A.8})$$

gives the difference between the energy lost and the mean energy lost and

$$\ln \epsilon' = \ln \frac{(1 - \beta^2)I^2}{2mc^2\beta^2} + \beta^2 \quad (\text{A.9})$$

with $\gamma_E = 0.577$ (Euler's constant). ϵ' is the low energy cutoff chosen by Landau such that the mean energy loss agrees with the Bethe-Bloch equation, and $I = 137$ eV. As stated in equation (A.2), I is the mean ionization potential to ionize a non-valence electron in silicon and is different from the band gap $E_o = 1.12$ eV which is the energy required to ionize the valence electron. δ is the density correction due to the fact that interactions amongst the atomic electrons can cause a screening effect [44] which reduces the ionization loss. This effect occurs because the electric field of the incoming charged particle is altered by the electric polarization of the matter. For $0.1 < \log_{10} \beta\gamma < 3.0$, the expression for the density correction is

$$\delta = 4.606 \log_{10} \beta\gamma - 4.38 + 0.0874(3 - \log_{10} \beta\gamma)^{3.586} \quad (\text{A.10})$$

Since for 5 GeV/c pions $\beta = 0.9996$, and $\log_{10} \beta\gamma = 1.55$ then, $\delta = 3.1$. Therefore, for 5 GeV/c pions incident on 300 μm of silicon, equation A.8 becomes

$$\lambda = \frac{1}{5.35 \text{ keV}}[E - 83.5 \text{ keV}], \quad (\text{A.11})$$

where E is in keV. Figure A.1 is a plot of a Landau distribution with the parameters as given in equation (A.11).

The most probable value of a Landau distribution is given by [44]

$$E_{MPV} = \xi(1.98 + \ln \frac{\xi}{\epsilon'} - \delta) \quad (\text{A.12})$$

and for 5 GeV/c pions $E_{MPV} = 82.2$ keV. It can be seen from figure A.1 that the mean of a Landau is at a higher energy than the most probable value.

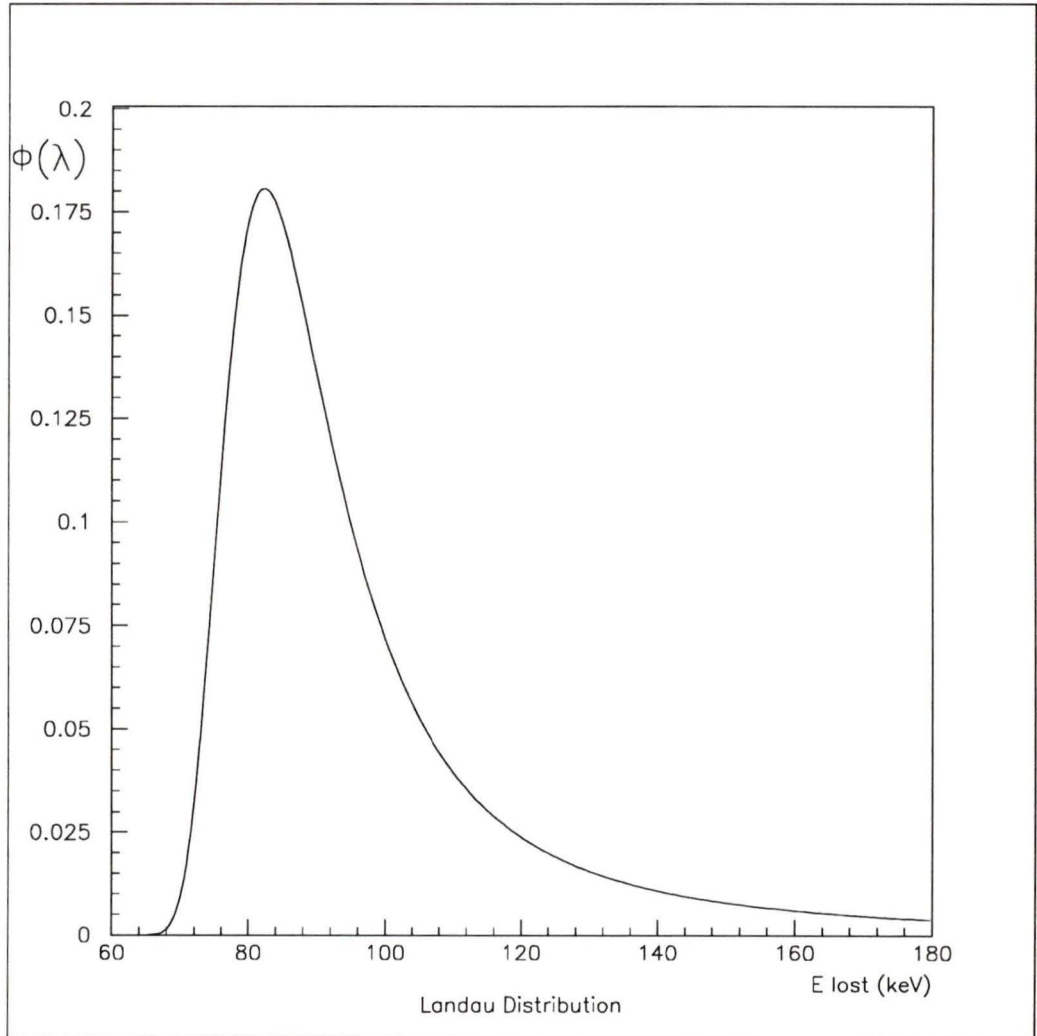


Figure A.1: Plot of a Landau distribution for 5 GeV/c pions in 300 μm of silicon. $\phi(\lambda)$ is the Landau integral shown in equation (A.7).

Appendix B

Simulation Results

Results from the Fitting Method

Table B.1 shows the runs performed with fitting method. Table B.2 gives the results of the runs performed with the fitting method. Table entries for which both the output ω/τ and the σ are zero indicate runs where no Gaussian fit could be made to the reconstructed ω/τ distribution.

<i>The Fitting Method</i>					
Run	# of events/set	input $\frac{\omega}{\tau}$ (ps ⁻¹)	bin size (ps)	mistag	bkg
1	200, 100, 50, 25	0.73, 2.19, 3.65, 5.11, 6.57	0.2	0.1	0.1
2	200, 100, 50, 25	0.73, 2.19, 3.65, 5.11, 6.57	0.1	0.1	0.1
3	200, 100, 50, 25	0.73, 2.19, 3.65, 5.11, 6.57	0.2	0.2	0.1
4	200, 100, 50, 25	0.73, 2.19, 3.65, 5.11, 6.57	0.2	0.1	0.2

Table B.1: *Table of runs performed with the fitting program.*

RUN #	# event	input om/tau	output om/tau	sigma	error om/tau	error sigma	% in +- 3 sigma	mean	SD
1	200	0.73	0.731	0.056	0.006	0.005	100	0.730	0.053
1	100	0.73	0.725	0.056	0.007	0.006	97	0.716	0.087
1	50	0.73	0.721	0.114	0.017	0.026	90	0.717	0.199
1	25	0.73	0.712	0.090	0.013	0.018	78	0.818	0.380
1	200	2.19	2.181	0.058	0.006	0.005	97	2.178	0.075
1	100	2.19	2.185	0.077	0.008	0.006	98	2.245	0.444
1	50	2.19	2.204	0.094	0.011	0.010	79	2.405	0.880
1	25	2.19	2.183	0.109	0.015	0.014	61	2.471	1.202
1	200	3.65	3.647	0.072	0.007	0.006	97	3.671	0.292
1	100	3.65	3.647	0.089	0.011	0.012	86	3.798	0.822
1	50	3.65	3.652	0.155	0.020	0.021	72	3.884	0.920
1	25	3.65	3.656	0.144	0.025	0.031	54	3.494	1.334
1	200	5.11	5.110	0.125	0.015	0.015	80	5.682	2.190
1	100	5.11	5.129	0.192	0.031	0.027	63	5.558	2.242
1	50	5.11	5.046	0.162	0.030	0.031	42	5.766	3.275
1	25	5.11	0.000	0.000	0.000	0.000	0	4.559	3.484
1	200	6.57	6.556	0.171	0.027	0.023	48	9.480	4.416
1	100	6.57	6.665	0.133	0.032	0.046	26	11.209	5.469
1	50	6.57	0.000	0.000	0.000	0.000	0	10.610	6.382
1	25	6.57	0.000	0.000	0.000	0.000	0	10.111	6.815
2	200	0.73	0.731	0.056	0.006	0.005	100	0.730	0.052
2	100	0.73	0.733	0.048	0.007	0.006	81	0.711	0.108
2	50	0.73	0.727	0.122	0.019	0.030	92	0.713	0.196
2	25	0.73	0.705	0.142	0.025	0.050	82	0.864	0.395
2	200	2.19	2.181	0.054	0.004	0.005	98	2.180	0.057
2	100	2.19	2.183	0.079	0.007	0.007	98	2.248	0.439
2	50	2.19	2.199	0.099	0.012	0.011	82	2.376	0.802
2	25	2.19	2.185	0.110	0.014	0.012	66	2.452	1.125
2	200	3.65	3.647	0.066	0.007	0.005	97	3.688	0.453
2	100	3.65	3.633	0.083	0.009	0.009	88	3.824	0.756
2	50	3.65	3.629	0.110	0.017	0.020	75	3.920	0.905
2	25	3.65	3.685	0.144	0.026	0.025	51	3.658	1.482
2	200	5.11	5.125	0.099	0.008	0.009	82	5.378	1.440
2	100	5.11	5.133	0.185	0.026	0.025	73	5.819	2.199
2	50	5.11	5.077	0.134	0.020	0.017	49	5.740	3.371
2	25	5.11	0.000	0.000	0.000	0.000	0	4.579	3.100

Table B.2 continued...

RUN #	# event	input om/tau	output om/tau	sigma	error om/tau	error sigma	% in +- 3 sigma	mean	SD
2	200	6.57	6.577	0.155	0.015	0.022	60	8.778	3.871
2	100	6.57	6.508	0.196	0.030	0.038	41	10.410	5.169
2	50	6.57	6.427	0.592	0.171	0.280	33	9.353	5.901
2	25	6.57	0.000	0.000	0.000	0.000	0	9.334	6.380
3	200	0.73	0.735	0.081	0.010	0.010	89	0.751	0.303
3	100	0.73	0.700	0.113	0.019	0.025	69	0.690	0.361
3	50	0.73	0.792	0.119	0.026	0.033	55	0.728	0.414
3	25	0.73	0.000	0.000	0.000	0.000	0	0.878	0.526
3	200	2.19	2.185	0.075	0.008	0.006	94	2.223	0.362
3	100	2.19	2.176	0.109	0.012	0.013	90	2.238	0.627
3	50	2.19	2.202	0.168	0.022	0.026	71	2.485	0.979
3	25	2.19	2.203	0.113	0.018	0.020	48	2.414	1.302
3	200	3.65	3.643	0.082	0.010	0.009	87	3.683	0.678
3	100	3.65	3.602	0.122	0.017	0.016	70	3.728	1.101
3	50	3.65	3.647	0.096	0.015	0.012	49	3.508	1.401
3	25	3.65	3.653	0.607	0.157	0.240	51	3.081	1.569
3	200	5.11	5.106	0.165	0.023	0.018	68	6.359	3.107
3	100	5.11	5.088	0.174	0.027	0.023	48	5.696	3.029
3	50	5.11	4.971	1.105	0.318	0.587	56	4.615	2.954
3	25	5.11	0.000	0.000	0.000	0.000	0	4.260	3.602
3	200	6.57	6.584	0.182	0.035	0.052	34	9.931	5.088
3	100	6.57	0.000	0.000	0.000	0.000	0	11.495	5.971
3	50	6.57	0.000	0.000	0.000	0.000	0	8.868	6.928
3	25	6.57	0.000	0.000	0.000	0.000	0	7.505	6.693
4	200	0.73	0.738	0.065	0.007	0.009	100	0.730	0.065
4	100	0.73	0.741	0.077	0.009	0.010	97	0.725	0.132
4	50	0.73	0.781	0.185	0.032	0.037	91	0.791	0.328
4	25	0.73	0.705	0.245	0.041	0.057	86	0.779	0.333
4	200	2.19	2.179	0.061	0.006	0.004	100	2.184	0.062
4	100	2.19	2.190	0.094	0.011	0.012	97	2.203	0.164
4	50	2.19	2.228	0.081	0.011	0.009	76	2.370	0.911
4	25	2.19	2.239	0.151	0.022	0.025	64	2.567	1.053
4	200	3.65	3.621	0.096	0.011	0.008	97	3.666	0.265
4	100	3.65	3.624	0.105	0.013	0.012	78	3.962	0.971
4	50	3.65	3.670	0.158	0.026	0.034	59	3.512	1.373
4	25	3.65	3.660	0.145	0.023	0.027	50	3.411	1.535

Table B.2 continued...

RUN #	# event	input om/tau	output om/tau	sigma	error om/tau	error sigma	% in ± 3 sigma	mean	SD
4	200	5.11	5.097	0.132	0.017	0.016	75	5.441	1.574
4	100	5.11	5.117	0.226	0.031	0.033	64	5.941	3.443
4	50	5.11	5.137	0.160	0.029	0.029	40	4.893	2.830
4	25	5.11	0.000	0.000	0.000	0.000	0	4.536	3.181
4	200	6.57	6.450	0.234	0.048	0.041	40	9.774	4.860
4	100	6.57	6.550	0.155	0.035	0.031	26	10.792	5.637
4	50	6.57	0.000	0.000	0.000	0.000	0	9.573	6.297

Table B.2: Results of runs performed with the fitting program. The first three columns show the run number, the number of events per data set, and the ω/τ used when generating the data. The next four columns show the output ω/τ and the sigma from the Gaussian fit of the reconstructed ω/τ distribution along with the associated errors. The next column shows the percent of events which were within $\pm 3\sigma$ of mean of the Gaussian-like distribution in the reconstructed ω/τ distribution. The last two columns show the mean and the standard deviation of the whole reconstructed ω/τ distribution.

<i>The Folding Method</i>				
Run	# of events/set	input $\frac{\omega}{\tau}$ (ps ⁻¹)	mistag	bkg
1	200, 100, 50, 25	0.73, 2.19, 3.65, 5.11, 6.57	0.1	0.1
2	200, 100, 50, 25	0.73, 2.19, 3.65, 5.11, 6.57	0.2	0.1
3	200, 100, 50, 25	0.73, 2.19, 3.65, 5.11, 6.57	0.1	0.2

Table B.3: *Table of runs performed with the folding program.*

Results from the Folding Method

A summary of the runs performed with the folding method is given in table B.3. Table B.4 gives the results of the runs performed with the folding method. Table entries for which both the output ω/τ and the σ are zero indicate runs where no Gaussian fit could be made to the folding frequency distribution.

RUN #	# event	input om/tau	output om/tau	sigma	error om/tau	error sigma	% in +- 3 sigma	mean	SD
1	200	0.73	1.056	0.616	0.168	0.266	89	1.284	0.625
1	100	0.73	1.176	0.784	0.239	0.431	67	1.876	1.120
1	50	0.73	0.000	0.000	0.000	0.000	0	2.414	1.122
1	25	0.73	0.000	0.000	0.000	0.000	0	3.211	0.959
1	200	2.19	2.291	0.085	0.013	0.014	67	2.457	0.301
1	100	2.19	2.425	0.241	0.037	0.056	90	2.567	0.540
1	50	2.19	2.277	0.097	0.014	0.011	53	2.636	0.628
1	25	2.19	2.332	0.119	0.020	0.025	50	2.931	0.671
1	200	3.65	3.764	0.211	0.032	0.035	83	3.592	0.743
1	100	3.65	3.813	0.465	0.103	0.133	78	3.685	0.986
1	50	3.65	0.000	0.000	0.000	0.000	0	3.850	1.190
1	25	3.65	5.753	3.969	7.958	5.126	77	4.016	1.107
1	200	5.11	5.319	0.160	0.030	0.041	55	4.471	1.756
1	100	5.11	5.332	0.169	0.039	0.036	41	4.608	1.934
1	50	5.11	5.333	0.100	0.024	0.032	29	4.814	2.102
1	25	5.11	4.911	4.102	0.965	1.632	98	5.316	2.005
1	200	6.57	0.000	0.000	0.000	0.000	0	3.463	2.347
1	100	6.57	0.000	0.000	0.000	0.000	0	3.650	2.023
1	50	6.57	0.000	0.000	0.000	0.000	0	4.814	2.364
1	25	6.57	0.000	0.000	0.000	0.000	0	5.001	2.182
2	200	0.73	1.177	0.577	0.145	0.240	92	1.580	0.825
2	100	0.73	1.365	0.604	0.152	0.258	78	2.160	1.056
2	50	0.73	0.000	0.000	0.000	0.000	0	2.878	1.170
2	25	0.73	0.000	0.000	0.000	0.000	0	3.243	1.026
2	200	2.19	2.377	0.149	0.033	0.038	79	2.483	0.416
2	100	2.19	2.312	0.109	0.018	0.017	59	2.539	0.607
2	50	2.19	2.308	0.087	0.015	0.020	47	2.749	0.792
2	25	2.19	2.435	0.594	0.182	0.279	59	2.961	0.691
2	200	3.65	3.890	0.708	0.212	0.290	69	3.249	1.213
2	100	3.65	3.390	1.596	0.519	0.662	81	3.627	1.238
2	50	3.65	3.345	2.203	0.835	1.471	100	3.581	1.224
2	25	3.65	0.000	0.000	0.000	0.000	0	3.921	1.141
2	200	5.11	5.305	0.081	0.016	0.017	29	3.822	2.083
2	100	5.11	5.276	0.096	0.019	0.019	28	4.430	2.153
2	50	5.11	5.379	2.886	0.805	1.638	80	5.223	2.001
2	25	5.11	4.860	3.216	0.794	1.623	89	5.032	2.102
2	200	6.57	6.776	0.660	0.295	0.519	22	3.410	2.361

Table B.4 continued...

RUN #	# event	input ω/τ	output ω/τ	sigma	error ω/τ	error sigma	% in ± 3 sigma	mean	SD
2	100	6.57	0.000	0.000	0.000	0.000	0	3.855	2.215
2	50	6.57	0.000	0.000	0.000	0.000	0	5.036	2.196
2	25	6.57	0.000	0.000	0.000	0.000	0	5.252	1.991
3	200	0.73	1.110	0.679	0.176	0.286	89	1.457	0.789
3	100	0.73	0.000	0.000	0.000	0.000	0	2.045	1.107
3	50	0.73	0.000	0.000	0.000	0.000	0	2.835	1.153
3	25	0.73	0.000	0.000	0.000	0.000	0	3.301	0.957
3	200	2.19	2.341	0.072	0.011	0.012	59	2.479	0.438
3	100	2.19	2.298	0.124	0.021	0.019	59	2.614	0.547
3	50	2.19	2.332	0.138	0.024	0.034	54	2.788	0.617
3	25	2.19	2.705	0.832	0.226	0.367	83	2.936	0.689
3	200	3.65	3.823	0.348	0.068	0.077	81	3.504	0.912
3	100	3.65	3.714	1.648	0.832	1.041	91	3.593	1.114
3	50	3.65	3.275	2.027	0.651	1.251	100	3.721	1.144
3	25	3.65	3.816	0.914	0.211	0.429	88	3.979	1.052
3	200	5.11	5.314	0.140	0.024	0.031	56	4.759	1.773
3	100	5.11	5.140	0.334	0.095	0.075	30	4.548	2.228
3	50	5.11	4.219	6.065	5.466	11.985	56	5.375	2.147
3	25	5.11	5.535	0.413	0.090	0.121	47	5.168	1.961
3	200	6.57	0.000	0.000	0.000	0.000	0	4.028	2.558
3	100	6.57	0.000	0.000	0.000	0.000	0	4.318	2.601
3	50	6.57	0.000	0.000	0.000	0.000	0	4.770	2.423
3	25	6.57	0.000	0.000	0.000	0.000	0	5.558	2.268

Table B.4: Results of runs performed with the folding program. The first three columns show the run number, the number of events per data set, and the ω/τ used when generating the data. The next four columns show the output ω/τ and the sigma from the Gaussian fit of the folding frequency distribution along with the associated errors. The next column shows the percent of events which were within $\pm 3\sigma$ of mean of the Gaussian-like distribution in the folding frequency distribution. The last two columns show the mean and the standard deviation of the whole folding frequency distribution.

<i>The FFT Method</i>					
Run	# of events/set	input $\frac{\omega}{\tau}$ (ps^{-1})	bin size (ps)	mistag	bkg
1	200, 100, 50, 25	0.73, 2.19, 3.65, 5.11, 6.57	0.164	0.1	0.1
2	200, 100, 50, 25	0.73, 2.19, 3.65, 5.11, 6.57	0.082	0.1	0.1
3	200, 100, 50, 25	0.73, 2.19, 3.65, 5.11, 6.57	0.164	0.2	0.1
4	200, 100, 50, 25	0.73, 2.19, 3.65, 5.11, 6.57	0.164	0.1	0.2

Table B.5: Table of runs performed with the FFT program.

Results from the FFT Method

A summary of the runs performed with the FFT method is given in table B.5. Table B.6 gives the results of the runs performed with the FFT method.

RUN #	# event	input omg/tau	mean	SD
1	200	0.73	4.085	2.395
1	100	0.73	3.269	2.108
1	50	0.73	3.539	2.723
1	25	0.73	3.945	2.886
1	200	2.19	2.590	0.110
1	100	2.19	2.567	0.210
1	50	2.19	3.182	1.840
1	25	2.19	3.635	2.158
1	200	3.65	3.876	0.439
1	100	3.65	3.774	0.644
1	50	3.65	4.546	1.986
1	25	3.65	4.633	2.263
1	200	5.11	4.540	1.852
1	100	5.11	4.674	2.002
1	50	5.11	4.958	2.367
1	25	5.11	4.569	2.731
1	200	6.57	4.616	2.437
1	100	6.57	4.543	2.393
1	50	6.57	5.120	2.395
1	25	6.57	5.065	2.673
2	200	0.73	5.629	4.975
2	100	0.73	5.196	5.686
2	50	0.73	5.405	5.491
2	25	0.73	6.277	5.481
2	200	2.19	2.613	0.115
2	100	2.19	2.730	1.513
2	50	2.19	4.065	4.050
2	25	2.19	5.724	5.284
2	200	3.65	4.206	1.861
2	100	3.65	5.096	3.781
2	50	3.65	7.364	5.437
2	25	3.65	7.255	5.290
2	200	5.11	5.880	3.864
2	100	5.11	6.825	5.139
2	50	5.11	7.689	5.328
2	25	5.11	7.777	5.539
2	200	6.57	7.179	4.957

Table B.6 continued...

RUN	#	input	mean	SD
#	event	omg/tau		
2	100	6.57	8.201	5.653
2	50	6.57	9.035	5.319
2	25	6.57	9.403	5.802
3	200	0.73	4.073	2.266
3	100	0.73	3.838	2.465
3	50	0.73	3.823	2.676
3	25	0.73	3.957	2.759
3	200	2.19	2.617	0.136
3	100	2.19	2.840	1.078
3	50	2.19	3.403	1.938
3	25	2.19	4.244	2.381
3	200	3.65	3.931	1.023
3	100	3.65	4.085	1.622
3	50	3.65	4.694	2.389
3	25	3.65	4.766	2.492
3	200	5.11	4.778	1.931
3	100	5.11	4.247	2.022
3	50	5.11	4.642	2.515
3	25	5.11	5.074	2.817
3	200	6.57	4.418	2.485
3	100	6.57	4.868	2.658
3	50	6.57	4.801	2.570
3	25	6.57	4.781	2.556
4	200	0.73	3.533	2.237
4	100	0.73	2.921	2.057
4	50	0.73	3.101	2.392
4	25	0.73	3.583	2.716
4	200	2.19	2.567	0.118
4	100	2.19	2.762	1.057
4	50	2.19	3.177	1.582
4	25	2.19	3.908	2.184
4	200	3.65	3.887	0.965
4	100	3.65	4.134	1.395
4	50	3.65	4.697	2.270
4	25	3.65	4.920	2.482
4	200	5.11	4.636	1.929
4	100	5.11	4.410	2.046

Table B.6 continued...

RUN #	# event	input ω/τ	mean	SD
4	50	5.11	4.473	2.481
4	25	5.11	4.755	2.590
4	200	6.57	3.960	2.235
4	100	6.57	4.723	2.378
4	50	6.57	5.379	2.594
4	25	6.57	5.033	2.633

Table B.6: Results of runs performed with the FFT program. The first three columns show the run number, the number of events per data set, and the ω/τ used when generating the data. The last two columns show the mean and the standard deviation of the whole FFT peak frequency distribution.

Vita

Surname: Vincter
Given Names: Manuella Greta
Place of Birth: Lasalle, Quebec
Date of Birth: 3rd of April, 1968

Educational Institutions Attended:

University of Victoria, Canada	1990-1992
McGill University, Canada	1987-1990

Degrees Awarded:

B.Sc. Hons. (Physics) McGill University, Canada	1990
---	------

Honours and Awards:

FCAR Fellowship	1990-1992
University of Victoria MacDonell Scholarship	1990-1991
NSERC Scholarship	1990
Vanier College Program Award in Pure and Applied Sciences	1987
NSERC Scholarship	1987

Publications:

None.

Partial Copyright License

I hereby grant the right to lend my thesis to users of the University of Victoria Library, and to make single copies only for such users, or in response to a request from the Library of any other university or similar institution, on its behalf or for one of its users. I further agree that permission for extensive copying of this thesis for scholarly purposes may be granted by me or a member of the university designated by me. It is understood that copying or publication of this thesis for financial gain shall not be allowed without my written permission.

Title of Thesis:

Measuring the Time Dependence of $B_s^o - \bar{B}_s^o$ Oscillations

Author: Manuella Greta Vinciter



December 7, 1992

(Date)